

UNIVERSITY OF CRETE
DEPARTMENT OF PHYSICS
MICROELECTRONICS RESEARCH GROUP

PH.D. DISSERTATION

**Spontaneous and selective
growth of GaN nanowires on Si
(111) substrates by molecular
beam epitaxy**

Savvas Eftychis

supervised by
Prof. Alexandros Georgakilas

December 13, 2018

PH.D. DISSERTATION

SPONTANEOUS AND SELECTIVE GROWTH OF GAN NANOWIRES
ON SI (111) SUBSTRATES BY MOLECULAR BEAM EPITAXY

ΔΙΔΑΚΤΟΡΙΚΗ ΔΙΑΤΡΙΒΗ

ΑΥΘΟΡΜΗΤΗ ΚΙ ΕΠΙΛΕΚΤΙΚΗ ΑΝΑΠΤΥΞΗ ΝΑΝΟΝΗΜΑΤΩΝ
GAN, ΠΑΝΩ ΣΕ ΥΠΟΣΤΡΩΜΑΤΑ SI (111), ΜΕ ΕΠΙΤΑΞΗ ΜΕ
ΜΟΡΙΑΚΕΣ ΔΕΣΜΕΣ.

Savvas Eftychis

Advisory committee: Prof. Alexandros Georgakilas (Principal Advisor)
Asst. Prof. Eleftherios Iliopoulos
Prof. Emer. Panagiotis Tzanetakis

Thesis committee: Prof. Alexandros Georgakilas
Assos. Prof. Eleftherios Iliopoulos
Assos. Prof. Zaharias Hatzopoulos
Asst. Prof. Konstantinos Makris
Prof. Nikolaos Pelekanos
Prof. Thomas Kehagias
Dr. George Konstantinidis

Abstract

Spontaneously grown gallium nitride (GaN) nanowires (NWs) by the use of plasma assisted molecular beam epitaxy (PAMBE) are a subject of active research due to their high crystalline quality and promising device applications. The properties of GaN NWs depend strongly on the initial surface on which they are grown. In this work we investigate the effect of different initial surfaces on the morphological properties of GaN NWs, when silicon Si (111) is used as a substrate. We employ several experimental techniques in order to determine the morphological, structural and optoelectronic properties of GaN NWs, including reflection high energy electron diffraction (RHEED), field-emission scanning electron microscopy (FE-SEM), X-ray diffraction (XRD), photoluminescence (PL) spectroscopy and high-resolution transmission electron microscopy (HRTEM).

In a first series of experiments, we explore the effect of substrate temperature (T_{sub}) on the nucleation, growth and properties of GaN NWs. The experiments follow (a) a one-step GaN growth procedure, with constant T_{sub} throughout GaN deposition, or (b) a two-step GaN growth procedure, using a lower T_{sub} for the initial stage than the later one. We achieve control of the NW diameter between ~ 20 – 40 nm. A significant suppression of GaN NW nucleation at high temperatures (~ 790 – 800°C) was observed for the one-step growth process. We are able to surpass this constraint using a two-step growth process. The GaN nucleation at the initial low T_{sub} stage allows for main GaN NW growth at much higher T_{sub} during the second growth stage.

Through a second series of experiments, we investigate how the formation of silicon nitride (Si_xN_y) affects GaN NW growth. Si_xN_y forms unintentionally when GaN is grown under N-rich conditions on a bare Si (111) surface. A better control of Si_xN_y formation can be achieved by intentional nitridation of the surface prior to GaN deposition. We perform the first systematic comparison of GaN NW properties grown on unintentionally and intentionally nitridated Si (111) surfaces. The intentional nitridation resulted in a uniform ~ 1.5 nm amorphous Si_xN_y interlayer at the GaN/Si interface, while an irregular and non-uniform interface, with partial presence of amorphous

Si_xN_y , appeared for direct growth of GaN on Si. The homogeneity of the interfacial structure enhanced the degree of crystallographic alignment of the GaN NWs, concerning both tilt and twist. It also decreased the dispersion of NW heights that is otherwise triggered by different nucleation times on structurally different sites of the substrate. The average height of the GaN NWs was similar for both cases but their average diameter was increased from 25 nm to 40 nm on the uniform amorphous Si_xN_y interlayer, possibly an effect of weak epitaxial constraints. Reduced overall intensity and increased defect-related emission at 3.417 eV characterized the 20 K photoluminescence spectra for direct GaN growth on Si.

A third series of experiments explores for the first time the effects of ultrathin AlN prelayers, with nominal thicknesses between 0 and 1.5 nm, on the spontaneous growth of GaN NWs on Si (111) substrates. The increase of AlN thickness gradually limits nitridation of the substrate surface and accelerates the nucleation of 3D GaN islands. The formation of amorphous Si_xN_y by Si nitridation is completely avoided for 1.5 nm of AlN that fully covers the Si surface. The dependence of the height, diameter and density of GaN NWs on the AlN thickness was also determined. Surprisingly, infinitely small changes in the AlN prelayer nominal thickness (~ 0.1 nm) can cause significant differences in the GaN NW nucleation procedure, and the final NW characteristics (i.e. differences in height of ~ 300 nm). The 1.5 nm AlN provided the optimum condition for GaN NW nucleation and growth; the NWs exhibited a large homogeneous height with almost no parasitic GaN formation between them. High resolution transmission electron microscopy showed the full relaxation of misfit strain of AlN on Si (111) and of GaN NWs on AlN. Analysis of in-situ RHEED monitoring of the AlN nucleation revealed the immediate relaxation of the AlN prelayer (before GaN deposition). Formation of $\beta\text{-Si}_3\text{N}_4$ before AlN nucleation was also observed.

In a fourth series of experiments, we study the epitaxial relation of the GaN NWs with the Si (111) crystal for off-axis substrates. We focus on the $(0001)_{\text{GaN}}//(\text{111})_{\text{Si}}$ epitaxial relation for GaN NWs grown on Si (111) substrates with different miscut angles, and for GaN NWs grown on nominally identical Si (111) off-axis substrates but different interfacial structures. Interestingly, the GaN $[0001]//\text{Si}[111]$ epitaxial relation is dominant, even in the case where a thick ~ 11.5 nm, amorphous Si_xN_y is present at the interface.

Finally, a method to selectively grow straight, vertical GaN nanowires by PAMBE at sites specified by a silicon oxide mask, which is thermally grown on silicon (111) substrates and patterned by electron-beam lithography and reactive-ion etching is also analyzed. The investigated method requires only one single molecular PAMBE growth process, i.e., the SiO_2 mask is formed on silicon instead of on a previously grown GaN or AlN buffer layer. The study

of various mask patterns, with the combination of numerical simulations, allowed us to evaluate how the geometrical characteristics (window diameter and spacing) of the mask affect the distribution of the nanowires, their morphology, and alignment for given Ga adatom diffusion length. Capabilities and limitations of this method of selective-area growth of nanowires have been identified. A window diameter less than 50 nm and a window spacing larger than 500 nm could provide selective nucleation of single nanowires in nearly all mask windows.

Acknowledgements

I would like to express my gratitude towards my advisor, Prof. Alexandros Georgakilas for his help and guidance throughout my PhD. Our collaboration has equipped me with indispensable skills, both for life, and for scientific research.

I would like to thank Dr. Adam Adikimenakis, for introducing me to the experimental world of molecular beam epitaxy. His long experience played a key role in the smooth operation of the MBE system. I am also grateful to Dr. Jann Kruse, with whom I worked closely during the experiments described. I also feel the need to thank Katerina Tsagaraki, for all the time she took on the SEM, looking at samples from the MBE, but also for her contribution and mentorship on XRD and AFM measurements. I am also grateful to Maria Androulidaki for all the PL characterization of the samples she performed, and for helping me in understanding the physics behind the PL spectra. Additionally, I want to express my gratitude to Nikos Papadakis and Mihalis Sfendourakis, that as technical gurus, came up with solutions to every technical problem that came up in the lab. Additionally, I would like to acknowledge Prof. Nikos Pelekanos, Dr. Savvas Germanis and Dr. Rahul Jayaprakash, for their fruitful discussions concerning PL measurements.

I would also like to thank Dr. Liverios Lymperakis from Max Planck Institute, for his valuable discussions concerning the growth mechanism, and for contributing with numerical simulations to this work. Additionally, I would like to thank our collaborators from Aristotle University of Thessaloniki, Prof. Philomela Komninou, Prof. Thomas Kehagias and Dr. Triantafyllia Koukoula for their work in TEM microscopy, and also our collaborators from Demokritos, Pascal Normand and Antonis Olziersky, for their contribution in the preparation of patterned samples. The work presented in this thesis, is the result of the excellent collaboration of all these people.

I am grateful to my colleague Dr. Elena Papadomanolaki, for being a valuable friend throughout my educational journey at the University of Crete. Elena and Stelios Kazazis were great office-mates and they both helped me through the easy and difficult times, and made my everyday life much more

interesting. Additionally, I would like to thank my colleagues, Athanasios Margiolakis, Alexandros Tzimis, George Doundoulakis and Dr. Christos Zervos, for all their help and support.

I would additionally like to thank my wife, Gina Panopoulou, for filling part of my life, supporting me through every difficulty that I had during the final stages of the PhD, and for proof reading my dissertation. Most of all I would like to thank my parents, Lenia and Michael, for their patience throughout all the years, for transmitting me their values, and for their moral and financial support, that was necessary for the completion of this work.

This research has been co-financed by the European Union (European Social Fund - ESF) and Greek national funds through the Operational Program "Education and Lifelong Learning" of the National Strategic Reference Framework (NSRF) - Research Funding Program: THALES, project " NanoWire" , MIS 377284. I am also grateful for the financial support provided by IESL/FORTH programs.

Contents

Contents	ix
List of figures	xii
1 Introduction	1
1.1 GaN nanowires	1
1.2 Scope of this work	2
2 Properties of III-Nitride semiconductors	7
2.1 Band structure	7
2.2 Crystal structure	8
2.3 Polarity - Polarization	10
3 Experimental Methods	17
3.1 Molecular Beam Epitaxy	17
3.1.1 Molecular Beam Epitaxy Vacuum Chambers	17
3.1.2 Radiofrequency Plasma source	20
3.1.3 Effusion cells	20
3.1.4 Physical processes of MBE - Surface kinetics	21
3.2 Characterization methods	24
3.2.1 RHEED: An in-situ surface characterization technique	24
3.2.2 Electron Microscopy	25
3.2.3 Photoluminescence Spectroscopy	27
3.2.4 Atomic force microscopy	28
3.2.5 X-ray diffraction	28
4 Stages of spontaneous GaN NW growth	35
4.1 The initial surface	35
4.2 GaN nanowire nucleation	37
4.3 Evolution of the formed GaN NWs	39
4.4 Evolution of NWs in our MBE system	41

4.5	Conclusions	45
5	The role of substrate temperature in spontaneous GaN nanowire growth	51
5.1	One-step growth	52
5.2	Two-step growth	55
5.2.1	The role of the duration of the low substrate temperature step	56
5.2.2	The role of substrate temperature during the elongation stage	60
5.3	Conclusions	64
6	Spontaneous growth of GaN nanowires on Si (111) surfaces: intentional and unintentional Si nitridation	69
6.1	Introduction	69
6.2	Experimental details	70
6.3	Experimental results	70
6.4	Discussion of results	77
6.5	Conclusions	80
7	Effects of ultrathin AlN prelayer on GaN nanowires	85
7.1	Introduction	85
7.2	Experimental Details	86
7.3	Experimental Results	87
7.3.1	RHEED observations for different samples	87
7.3.2	NWs morphology and structure	88
7.3.3	RHEED observations during the first stages of AlN deposition	91
7.4	Discussion	96
7.5	Conclusions	98
8	GaN NW growth on off-axis Si (111) wafers	107
8.1	Effects of the Si (111) miscut angle on GaN NWs growth . . .	107
8.2	Effects of the interfacial structure on GaN NW growth on off-axis Si (111) wafers	110
8.3	Conclusions	114
9	Selective-area growth of GaN NWs on bare Si (111) substrates	119
9.1	Introduction	119
9.2	Experimental details	120

9.3	Results and discussion	122
9.3.1	Role of AlN prelayer	123
9.3.2	Effects of the mask geometrical characteristics	124
9.4	Conclusions	130
10	Summary and future prospects	141
10.1	Conclusions	141
10.2	Relevant Future work	143
Appendix A	Si (111) wafer preparation	147
A.1	Chemical treatment	147
A.2	Thermal treatment	147
Appendix B	Publications - Conferences	151
B.1	Journal publications	151
B.2	Conference proceedings publications	151
B.3	International Conferences	153
B.4	Panhellenic conferences	156

List of Figures

2.1	The areas covered by III-Nitride (blue-shaded), III-Arsenide (orange-shaded) and III-Phosphite (gray-shaded) groups in the Energy band gap – α -Lattice constant plane.	8
2.2	(a) The wurtzite structure, showing the AB AB stacking. (b) The zinblende structure, showing the ABC ABC stacking. . .	9
2.3	(a) The hexagonal structure of wurtzite, depicting the dimensions a and c. (b) The c-plane, m-plane, a-plane and r-plane are depicted in the hexagonal wurtzite cell. Blue spheres (larger) represent Ga atoms, and red spheres (smaller) represent N atoms	10
3.1	Schematic drawing of a plasma-assisted molecular beam epitaxy growth chamber, used for growing III-nitride semiconductors.	19
3.2	Schematics of the basic processes that occur during molecular beam epitaxy: (a) atoms impinging, (b) physisorption, (c) incorporation (chemisorption), (d) desorption, (e) diffusion and (f) decomposition of the crystal	22
3.3	Showing the possible positions of adsorbed atoms to form chemical bonds on the surface. Atoms can be chemisorbed: (a) on the surface of the sample, (b) the edge of a step, (c) in the kink, (d) in a vacancy on the edge of a step and (e) in a vacancy on the surface. In the case of (1) diffusion can lead to further aggregation of atoms on the surface.	23
3.4	Showing the three different growth modes:(a) Frank-van der Merwe mode, layer by layer growth, (b) Volmer-Weber mode, island growth, and (c) Stranski-Krastanov mode, layer plus island growth.	23
3.5	RHEED setup diagram	25

3.6	Schematic representation of the inverse space, and the Ewald's sphere. The section of the Ewald's sphere with the rods of the surface atoms is the RHEED pattern	26
3.7	RHEED patterns that show (a) a streaky, (b) a spotty and (c) a streaky with spotty pattern, that correspond to (a) a smooth surface, (b) 3D structures and (c) a rough surface or small 3D structures that started nucleating.	27
3.8	Schematics of the atomic force microscopy setup. The probe scans the surface of the sample, while its position is monitored by the reflection of a laser beam.	28
3.9	Representation of the Bragg's condition.	29
3.10	A schematic, showing the incident and reflected beams on the sample. The allowable rotations of the sample define the ω , ϕ and χ angles, and the position of the detector defines the 2θ angle.	30
3.11	Schematic representation of Bragg reflection on well aligned (a) and less aligned (b) NWs. The Bragg diffracted X-ray beam has less intensity for a specific $\omega - 2\theta$ scan in the case of misaligned NWs.	31
4.1	(a) RHEED pattern for electron beam incident along the $\langle 0\bar{1}1 \rangle_{Si}$. A $\times 7$ Si (111) surface reconstruction is visible, that corresponds to the 7×7 Si (111) surface reconstruction. (b) Pixel intensity averaged over the height of the image in (a) within the gray dashed border, as a function of the x-distance in (a). The distance between the streaks visible is $1/7$ of the distance between the two main Si (111) streaks.	36
4.2	The diffuse RHEED that is visible after the nitridation of the Si (111) surface, and the formation of an amorphous Si_xN_y	37
4.3	The $\times 1$ RHEED diffraction pattern for an incident electron beam along the $\langle 10\bar{1}0 \rangle$ AlN direction. This is characteristic of the 1×1 AlN surface.	37
4.4	The $\times 1$ RHEED diffraction pattern, for an electron beam incident along the $\langle 10\bar{1}0 \rangle$ AlN direction, of the 1×1 AlN surface, with the faint appearance of 3D GaN island spots.	38
4.5	Plan-view HRTEM image of a GaN NW base. The hexagonal (red dottedshape) morphology of the GaN NW, with 10-10 side facets (m-planes) is evident.	39
4.6	Theta-2theta XRD measurements, showing that the orientation relationship between the GaN NWs and the Si substrate is $(0002)_{GaN} // (111)_{Si}$	40

4.7	The characteristic spotty RHEED diffraction pattern observed for an electron beam incident along the $\langle 10\bar{1}0 \rangle$ GaN direction, when GaN NWs are fully formed and grown as described in the text.	41
4.8	Diffusion of adatoms on the surface and on the side facets of a NW. Diffusion drives the adatoms towards the top facet of the NW, the c-plane facet, that acts as a sink.	42
4.9	Cross-section (top row), tilted (middle row) and top view (third row) SEM micrographs of NW samples grown for 20 min, 40 min, 60 min, 180 min and 330 min, in identical growth conditions ($F_{Ga} = 84.6$ nm/h, $F_N = 430$ nm/h, $T_{Gr} = 760^\circ\text{C}$). The scale bar is 200 nm for all micrographs.	43
4.10	Average height, h , of the GaN nanowires (black circles), grown for different time duration (20, 40, 60, 180 and 330 min), in identical growth conditions ($F_{Ga} = 84.6$ nm/h, $F_N = 430$ nm/h, $T_{Gr} = 760^\circ\text{C}$). The expected NW height if it was Ga-limited and N-limited are also shown by red triangles and blue squares, respectively.	44
4.11	Average diameter of GaN nanowires, grown for different durations ($t_{Gr} = 20, 40, 60, 180$ and 330 min) in identical growth conditions ($F_{Ga} = 84.6$ nm/h, $F_N = 430$ nm/h, $T_{Gr} = 760^\circ\text{C}$). The line is a linear fit to the data, giving an average diametric growth rate of 7.46 nm/h.	45
4.12	Density of GaN nanowires, grown for different time duration (20, 40, 60, 180 and 330 min), for identical growth conditions as described in the text. During the first minutes there is a steep increase, that is followed by an exponential-like decrease.	46
5.1	One-step growth NW samples. Cross-section (top row), tilted (middle row) and top view (third row) SEM micrographs of samples grown at 760°C (a, b and c), 780°C (d, e and f), 790°C (g, h and i) and 800°C (j, k and l). The Ga- and N- fluxes used were 84.6 nm/h and 430 nm/h respectively, and the total GaN deposition time was 3 h.	53
5.2	Graphs showing the relation of (a) height and (b) density as a function of temperature. The measurements were made for samples with GaN NWs grown at different T_{sub} (760°C , 780°C , 790°C and 800°C), from SEM micrographs. For the case of $T_{sub} = 760^\circ\text{C}$, two samples were grown and illustrated in the graphs.	54

5.3	Graphs showing (a) the average (red circles) and minimum (black squares) diameter as a function of temperature and (b) the time needed for the appearance of the first GaN 3D spots in the RHEED pattern, τ , as a function of temperature. Samples with GaN NWs grown at 760°C, 780°C, 790°C and °C for a duration of 3h, under identical growth conditions (see text) were used. Additionally for (b), RHEED observations for samples grown using the same Ga and N fluxes, at temperatures of 730°C and 745°C for the first 20 min were used. The inset in (b) shows the linear fit performed for the calculation of the E_{inc} of GaN on the crystalline AlN prelayer used.	55
5.4	SEM micrographs of cross-section (top row), top (middle row) and tilted view (bottom row) for samples with $t_{IGS} = 0$ (a, e, i), $t_{IGS} = 3$ min (b, f and j), $t_{IGS} = 6$ min (c, g, k) and $t_{IGS} = 20$ min (d, h, l).	57
5.5	SEM micrographs of the sample growth at $T_{sub} = 730$ °C, for a total growth duration of 20 min, with N and Ga fluxes equal to 430 nm / h and 84.6 nm / h; (a) top and (b) tilted view.	58
5.6	(a) Average and maximum heights of the GaN NWs grown with different time durations of the IGS stage ($t_{IGS} = 0, 3$ min, 6 min and 20 min) and with $T_{IGS} = 730$ °C and $T_{FGS} = 780$ °C. (b) the height distributions for samples grown with different duration of the initial growth stage.	59
5.7	The density of GaN nanowires in samples with different duration of the initial growth stage, at $T_{IGS} = 730$ °C, and the same total growth time (3h) and growth conditions ($F_{Ga} = 84.6$ nm / h, $F_N = 430$ nm / h, $T_{FGS} = 780$ °C). The values of the sample grown directly at 780°C for 3h ($t_{IGS} = 0$ min) are also depicted, for comparison with the one step growth. The line is guide for the eyes.	60
5.8	Diameter of the GaN NWs, for samples with different initial-growth durations studied (t_{IGS}), at $T_{IGS} = 730$ °, and the same total growth time (3h) and growth conditions ($F_{Ga} = 84.6$ nm / h, $F_N = 430$ nm / h, $T_{FGS} = 780$ °C).	61
5.9	SEM images of the cross-section (top row), tilted (middle row) and top (bottom row) view for samples grown with identical growth conditions ($T_{IGS} = 730$ °, $t_{IGS} = 20$ min, $F_{Ga} = 84.6$ nm / h, $F_N = 430$ nm / h), but with different T_{FGS} , equal to 750°C, 760°C, 770°C, 780°C, 790°C and 800°C.	62

5.10	The height of GaN NWs grown on 1.5 nm AlN/Si (111) by one-step and two-step growth processes, at different substrate temperatures. In the case of the two-step process the value of T_{FGS} used for 160 min GaN NW growth is used in the plot. The first step of 20 min growth, was accomplished at 730°C. The Ga and N fluxes used were identical for all the samples (84.6 nm / h and 430 nm / h.	63
5.11	The density of GaN NWs grown by a one-step or two-step growth process at different substrate temperatures. In the case of two-step process, initial GaN growth was carried out at 730°C for 20 min. The total growth time for all GaN NW samples was 3h.. . . .	64
5.12	The GaN NW average diameter, measured from SEM micrographs of samples grown with a two-step growth process, at different substrate temperatures during the final growth stage. The initial substrate temperature, T_{IGS} was 730°C, and the initial growth duration was 20 min. The Ga and N fluxes used were identical for all the samples (84.6 nm / h and 430 nm / h).	65
6.1	FE-SEM micrographs for observation at (a, b) 30 tilt view, (c, d) top view and (e, f) cross-section view showing the GaN nanowires of sample A (a,c,e) and sample B (b,d,f). Sample A of direct GaN growth on Si (111) exhibits increased misalignment of nanowires compared to sample B of GaN growth on intentionally nitridated Si (111) substrate.	71
6.2	Height distribution of the two samples, as measured by FE-SEM images. Sample A (B) height distribution is denoted with black color (grey color). The curves serve as a guide for the eye.	72
6.3	XRD rocking curves around the (0002) GaN reflection for samples A and B.	72
6.4	ϕ -scan of the (11.4) GaN planes, revealing the twist coherency, with the six-fold symmetry.	73
6.5	Cross-sectional HRTEM image of sample A, along the $[\bar{1}10]_{Si}$ zone axis, illustrating an inclined GaN NW nucleated directly on the Si surface. In the inset, the corresponding FFT diffractogram from the interfacial area shows the orientation relationship between the GaN NW and the Si substrate. Red circles denote the $[1\bar{1}00]$ -type reflections of wurtzite GaN. . . .	73

6.6	HRTEM image of sample B, viewed along the $[11\bar{2}0]_{GaN} // [\bar{1}10]_{Si}$ zone axes, showing a slightly inclined GaN NW grown on the thin amorphous Si_xN_y layer of the Si surface. Wurtzite GaN crystalline remnants (arrows) are depicted on either side of the NW.	74
6.7	FE-SEM image of sample B, after the KOH etching, showing the characteristic etched top part of N-polar GaN NWs.	74
6.8	Photoluminescence spectra taken (a) at room temperature and (b) at 20K. The inset is the PL spectrum at 20K in the band edge region, showing the different contribution of the defect-emission peak at 3.417 eV in the two samples.	76
6.9	Cross-sectional HRTEM image of sample A illustrating three adjacent NWs along the $[11\bar{2}0]_{GaN} // [\bar{1}10]_{Si}$ zone axes. Roughening of the Si (111) surface and formation of a thin amorphous Si_xN_y layer are due to unintentional nitridation. The central NW grown on a 1.3 nm thick amorphous Si_xN_y has a larger diameter, due to the absence of crystalline constraints with Si, compared to the other two thin NWs that are partially or fully in contact with the Si substrate, as shown in the insets depicting the corresponding GaN/Si interfaces.	77
7.1	RHEED patterns for electron beam incidence along the $\langle 11\bar{2}0 \rangle_{GaN}$ azimuth after 5 minutes of GaN deposition, for samples with AlN prelayer thickness of (a) 0.2, (b) 0.4, (c) 0.5 and (d) 1.5nm.	89
7.2	Cross-sectional FE-SEM micrographs of GaN NWs grown on: (a) nitridated Si (111) surface or after depositing on Si (111) an AlN prelayer with nominal thickness (b) 0.22nm, (c) 0.38nm, (d) 0.54nm and (e) 1.5nm.	90
7.3	(a) Height, (b) diameter, (c) density and (d) (0002) GaN ω -scan FWHM of GaN NWs grown spontaneously on Si (111) with different AlN prelayer thickness.	91
7.4	(a) HRTEM image of a GaN NW with 0.38 nm AlN prelayer showing the GaN/Si interface, projected along $[11\bar{2}0]_{GaN} // [110]_{Si}$ zone axes (z.a.). The amorphous interfacial layer is clearly visible.	92
7.5	HRTEM image of the sample with 0.38 nm AlN prelayer, projected along $[11\bar{2}0]_{GaN} // [110]_{Si}$ z.a., illustrating a non polar m-plane GaN crystal sharing an amorphous interface with the Si substrate. Basal plane SFs are also visible in GaN.	92

- 7.6 a) HRTEM image showing another crystal of m-plane GaN in the sample with 0.38 nm AlN prelayer, where the thin bright contrasted interfacial layer is in focus. It is clear that this area is crystalline, corresponding to the c-planes of GaN. b) Bragg image taken by Fourier filtering of (a), indicating the flat Si surface. c) Fourier filtered image from (a) showing the amplitude of the 111-Si frequency. d) Fourier filtered image from (a) showing the amplitude of the c-GaN frequency. . . . 93
- 7.7 HRTEM image of the GaN NWs sample with 1.5nm AlN prelayer thickness showing GaN NWs/AlN/Si interface, projected along $[11\bar{2}0]_{GaN} // [110]_{Si}$ z.a.. No amorphous interfacial layer at the GaN/AlN/Si interface can be detected. The AlN layer presents a dot-like albeit continuous form, where a GaN NW nucleates directly on top of it. 94
- 7.8 (a) HRTEM image of a part of the previous GaN/AlN/Si interface. (b) Corresponding GPA map of the lattice strain component along the growth direction. (c) Corresponding line profile of the lattice strain of the (0002) GaN and AlN planes. The average calculated strain is $-21.2(\pm 0.6)\%$ for AlN and $-18.6(\pm 0.3)\%$ for GaN, implying an almost strain-free configuration. 95
- 7.9 RHEED patterns for electron beam incidence along the $\langle 10\bar{1}0 \rangle_{AlN} / \langle \bar{2}11 \rangle_{Si}$ azimuth showing (a) the 7×7 Si (111) reconstruction, taken 0.4 sec before opening the main shutter, (b) the 8×8 β -Si₃N₄ (0001) reconstruction, taken 1.2 sec after the opening of the main shutter, and (c) the AlN pattern, taken 11.3 sec after the main shutter opening, as they were recorded for the case of AlN deposition. The averaged pixel intensity along the horizontal X-axis, for the rectangular regions depicted in gray dashed line in (a), (b) and (c), are shown in (d), (e) and (f), respectively. The position of the (01)-order RHEED bulk line of Si (111) (d, e) and AlN (0001) (f) are indicated by black arrows, with the X-axis representing the X-pixel distance along the chosen rectangle. The dotted rectangles in (a) and (b) define the background regions, for the 7×7 and 8×8 streak intensity, as defined by the enclosed solid line. 100

- 7.10 Analysis of RHEED observations during the growth of AlN on Si (111) substrate that initially exhibits the 7×7 surface reconstruction: (a) Time evolution of the reconstructions 7×7 Si (111) (gray curve) and 8×8 β -Si₃N₄ (black curve) , and (b) Variation of the intensity of the RHEED (01) bulk lines of Si (111) (black curve) and AlN (0002) (gray curve) versus the deposited AlN thickness. 101
- 8.1 Illustration showing the relative direction of the normal on the substrate surface (Z-axis) and the Si [111] (blue line) and GaN [0001] (red line) crystal directions. The drawing also shows the Si [111] tilt angle, α_{Si} , the GaN [0001] tilt angle, α_{GaN} , the angle between the GaN [0001] tilt direction and the Si [111] tilt direction, $\Delta\beta$, and the projected GaN [0001] tilt angle towards the Si [111] tilt direction, γ . The apparent angles are larger compared to the real values, for illustrative reasons . . . 108
- 8.2 Results of the XRD measurements for GaN NWs grown on Si (111) substrates with increasing miscut angles (0.24° , 0.82° , 2.97° and 4.42°). Graph (a) shows (a) the relative angle of the Si (111) and GaN (0001) directions ($\Delta\beta$) and graph (b) shows the tilt angle of GaN (0001) planes (α_{GaN}) and its projection on the Si [111] / substrate surface normal plane (γ) 110
- 8.3 Cross-section (top row), tilted (middle row) and top view (third row) SEM micrographs of GaN NWs grown on Si (111) substrates with increasing miscut angles: 0.24° (a, e, i), 0.82° (b, f, j), 2.97° (c, g, k) and 4.42° (d, h, l). 111
- 8.4 Results of SEM image measurements for GaN NWs grown on Si (111) substrates with different miscut angles, showing (a) the diameter, (b) the NW height and (c) the density of the GaN NWs 112
- 8.5 The miscut angle (α_{Si}) and the GaN (0002) tilt angle (α_{GaN}) can be seen for GaN NWs grown on miscut Si (111) wafers, with different interfacial layers. The difference between the two angles for each sample is marked. 114
- 8.6 The FWHM of the $(0002)_{GaN}$ RC and the difference in the tilt directions between Si (111) and GaN (0002) ($\Delta\beta$) can be seen for NWs grown on nominally 3.7° off-axis Si (111) substrates, with different interfacial structures. 115

- 8.7 Schematic of the Nagai model, explaining the tilt between the substrate (Si (111), with black lines) and the epitaxial layer (AlN (0002), with orange line). The substrate surface is shown with a gray, dotted line. 115
- 9.1 SEM images showing the processed patterns in 20 nm-thick thermally grown SiO₂ masks on Si (111) substrates with (a) hexagonal and (b) square lattices of circular windows (window diameter: $D_w = 20$ nm, window period/spacing: $S = 125$ nm). Inset of (b): Tilted cross-sectional view of the square lattice. The scale bar is 200 nm for all micrographs. 121
- 9.2 Top-view SEM images of some of the windows in the SiO₂ masks with window diameter D and spacing S , which have stayed partially empty during the growth of the nanowires. (a) $D_w = 20$ nm, $S = 125$ nm; (b) $D_w = 40$ nm, $S = 125$ nm; and (c) $D_w = 80$ nm, $S = 250$ nm. 122
- 9.3 SEM tilted view images showing the same region of patterned mask ($S = 250$ nm and $D_w = 60$ nm) for 3 different GaN NW samples, grown on identically grown conditions but with different amounts of AlN deposition. (a) No AlN was deposited, (b) 0.4 nm of AlN was deposited, (c) 1.5 nm of AlN was deposited. The scale in all three images is shown in (c). 123
- 9.4 SEM images of tilted view of GaN NWs, on mask regions with $D_w = 40$ nm and different window spacings. (a) $S = 125$ nm, (b) $S = 250$ nm, (c) $S = 500$ nm and (d) $S = 1000$ nm. 124
- 9.5 Plots illustrating (a) the FF and (b) the average NW number per window, for window spacings of 250 nm (blue triangle pointing towards the right), 500 nm (green triangle pointing down) and 1000 nm (red triangle pointing up), as a function of the window diameter (x-axis). 125
- 9.6 SEM images for a sample with a square pattern, with $S = 10$ μm spacing and $D_w = 25$ nm. (a) Top view of the sample, with a small magnification (scale bar is 10 μm), and (b) SEM micrograph of a tilted-view GaN NW at a larger magnification (scale bar is 100 nm), focusing in the central grown window and in the NWs grown around the window. 126
- 9.7 SEM images of the tilted view GaN NWs, on regions with $S = 1000$ nm, and different window diameters. (a) $D_w = 40$ nm (b) $D_w = 60$ nm (c) $D_w = 80$ nm (d) $D_w = 100$ nm and (e) $D_w = 200$ nm 126

- 9.8 Average height (black circles) and diameter (gray squares) of NWs for different window spacing S , taking into account only nanowires that grew straight and separated inside windows of $D_w = 40$ nm diameter. The dotted lines are linear fits to the data. 127
- 9.9 (a) TEM image depicting two nanowires in a single window ($D_w=80$ nm, $S=500$ nm), where the right one comprises two coalesced individual nanowires. The corresponding selected area electron diffraction (SAED) pattern (inset) reveals the epitaxial relationship between the Si and GaN lattices. Three-index reflections refer to Si, while four-index reflections belong to the wurtzite structure of GaN. (b) HRTEM image of the interfacial area indicated by the white rectangle in (a), along the $[11-20]$ GaN/ $[110]$ Si projection direction, showing the nucleation site and the perfect lattice alignment of the coalesced nanowires. The rough Si surface of the window is covered by a thin amorphous layer of about 2 nm. Nevertheless, the epitaxial relation of GaN with Si remains unaffected. 132
- 9.10 Photoluminescence in semi-logarithmic scale taken at 20K of nanowires grown self-arranged (upper, solid line) as well as inside windows with diameter D_w and spacing S of $D_w=80$ nm, $S=500$ nm (middle, dotted line) or $D_w=40$ nm, $S=1000$ nm (lower, dashed line). The inset shows the same measurements at room temperature. Emission happens only in the ultraviolet, no peaks appear throughout the entire measured visible spectrum. (The graphs have been separated by one decade for visibility: solid line $\times 100$, dotted line $\times 10$, and dashed line $\times 1$.) 133
- 9.11 Cross-sectional tilted view of KOH etched GaN NWs grown on regions with (a) $S=1000$ nm and $D_w=200$ nm and (b) $S=500$ nm and $D_w=80$ nm 133
- 9.12 Contour plot indicating the chemical potential calculation of Ga adatoms. The open and filled hexagons indicate the position of the empty and filled with NW windows in the mask, respectively. The distances are in units of diffusion length. Periodic boundary conditions are applied in both directions. . 134
- 9.13 Change of the chemical potential $\Delta\mu$ and adatom density c in the window at the center of the supercell as function of distance from the center, for different window diameters. c_0 is the maximum adatom density calculated at the center of the widest window. The distance from the center of the window is in units of window diameter. 135

- 9.14 Change of the chemical potential $\Delta\mu$ and adatom density c in the window at the center of the supercell as function of the window spacing for various diffusion lengths of 400 nm (black circles), 500 nm (red circles) and 800 nm (blue circles), as well as window diameters of 60 nm (empty circles) and 80 nm (filled circles). c_0 is the maximum adatom density calculated for the maximum window spacing. The window spacing is in units of diffusion lengths. 136
- A.1 The characteristic $\times 7$ pattern for electron beam incidence along the (a) $\langle 0\bar{1}1 \rangle$ and (b) $\langle \bar{2}11 \rangle$ Si azimuth, denoting the characteristic 7×7 Si (111) surface reconstruction. 148

Introduction

1.1 GaN nanowires

Ever since GaN nanowires (NW) were spontaneously grown on sapphire and silicon substrates by the pioneering work of the groups of Kishino [13] and Calleja [9] respectively, they have been at the center of scientific research on III-Nitride semiconductors. This is due to their improved crystalline structure compared to epitaxially grown GaN films, that allows for advances in the already well-established technological achievements and applications of the III-N semiconductors.

GaN NWs grown by the bottom-up, diffusion induced (DI) growth mechanism (further explained in Chapter 1) are immune to any lattice mismatch with the substrate. Any misfit dislocations that could result from the relaxation of misfit strain, are limited at the interface between the NW GaN crystal and the underlying substrate, at the base of the nanowire [11]. The large surface-to-volume ratio facilitates the escape of any threading dislocations out of the GaN crystal. All the above result in the growth of a fully relaxed crystal, free of extended defects such as threading dislocations or basal plane stacking faults.

The superior crystal quality of the NWs makes them appealing for optoelectronic devices like light emitting diodes (LEDs) [4] and lasers [1], and also nanoscale transistors [3]. The NW large surface-to-volume ratio is favorable for applications in photovoltaics [8] and sensors [5]. Additionally to the above, the fact that they can be realized on a variety of different surfaces, like silicon [9], sapphire [13], diamond [10], graphene [7] and TiN [12] allows them to be integrated in a variety of different platforms. A single GaN NW was also recently integrated in an AFM tip, in order to improve imaging resolution of the technique [2].

Apart from the significant achievements in device applications, the ongoing NW research also focuses in understanding the mechanisms occurring during the spontaneous growth of GaN NWs. The significant progress made

in understanding GaN NW formation, has led to the distinction of different pathways of the process, depending on the initial surface used for GaN deposition. When GaN NWs are grown spontaneously on a Si (111) substrate, the formation of the NWs is most commonly studied on three different initial surfaces: (i) on an amorphous Si_xN_y layer, (ii) on a not-well defined, unintentionally nitridated Si (111) surface and (iii) on a crystalline AlN layer. For devices demanding a better control in the GaN NW location and arrangement, a selective area growth method (SAG) has been successfully applied [6] (and refernces therein). In this method, NW nucleation sites are specified on a mask that is developed on GaN templates, GaN buffer layers or AlN buffer layers.

1.2 Scope of this work

In this work we aim to address issues concerning both spontaneous growth of GaN NWs as well as selective area growth. Initially, we study the effect of substrate temperature on different steps of GaN NW growth. Then, we investigate in detail the three pathways of spontaneous GaN NW formation on Si (111) substrates by focusing on a few well-defined but under-explored open questions. First, we wish to understand and quantitatively characterize the differences in NWs forming on an intentionally nitridated surface compared to one that becomes unintentionally nitridated. For this purpose, we conduct a comparative examination between the two cases. Second, we explore the formation of NWs in the boundary between the regime of growth on crystalline AlN and that of amorphous Si_xN_y . In order to achieve this, samples with ultrathin AlN layers were compared. We also studied the GaN [0001] // Si [111] epitaxial relation of GaN NWs when grown on off-axis Si (111) substrates. A fourth goal of this research was to identify possible improvements on the SAG method on Si (111) substrates, and identify significant factors that affect the final GaN NW array morphology.

The outline of this dissertation is as follows. Chapter 2 presents the properties of III-N semiconductors. Chapter 3 focuses on the experimental methods used throughout this work. There, the basics of plasma-assisted molecular beam epitaxy (PA-MBE) and the principles governing the epitaxial growth are presented. Additionally, the techniques that were used in order to evaluate the grown samples, such as reflective high energy electron diffraction (RHEED), scanning electron microscopy (SEM), photoluminescence spectroscopy (PL), X-ray diffraction and transmission electron microscopy (TEM) are briefly described.

In Chapter 1, we present the current understanding of the spontaneous

growth of GaN NW formation, on Si (111) substrates. We begin by presenting in more detail the three different pathways of initial surfaces when Si (111) substrates are used. The chapter then describes the mechanisms that occur during the GaN NW formation process. Through a series of experiments with GaN NWs that were grown at identical conditions but different growth durations, we also focus on the evolution of the GaN NWs.

The following chapter, Chapter 5, focuses on the role of the substrate temperature in GaN NW growth and the effects on the final GaN NW characteristics. This is done by a comparative examination of GaN NW samples grown at different substrate temperatures. For a more thorough study of the effects of temperature, a series of two-step grown samples was deemed necessary in order to investigate the substrate temperature effects in the last stage of GaN NW formation.

In the next chapter, Chapter 6, we investigate the role of a thin amorphous Si_xN_y at the interface between the GaN NW and the Si (111) substrate. The unintentional Si nitridation, during the first stages of direct GaN NW growth, on the bare Si surface, is compared to intentional Si nitridation prior to GaN growth. The morphology, structure and optoelectronic properties of GaN NWs is linked to characteristics of the interfacial layer, and to processes that occur during the initial growth stages.

An investigation of ultrathin AlN prelayers, in the GaN NW formation is presented in Chapter 7. This chapter investigates the boundary between the regime of growth on amorphous Si_xN_y and crystalline AlN. Significant changes in the GaN NW formation process, and in the final NW characteristics are identified between samples with minimal differences in the AlN prelayer nominal thickness.

In chapter 8, we study the effects of GaN NWs growth on off-axis Si (111) substrates. More specifically we focus on the $[0001]_{\text{GaN}}//[111]_{\text{Si}}$ epitaxial relation for GaN NWs grown on Si (111) substrates with different miscut angles, and for GaN NWs grown on nominally identical Si (111) off-axis substrates but different interfacial structures. The $\text{GaN}[0001]//\text{Si}[111]$ epitaxial relation for GaN NWs grown on amorphous Si_xN_y with different thicknesses and on crystalline AlN is under investigation.

The following chapter (Chapter 9), deals with the selective area growth (SAG) of GaN NWs on Si (111) substrates. A successful method for SAG growth on a nano-patterned SiO_2 mask on Si (111) substrate has been found, that minimizes the steps required in order to achieve good growth selectivity. The mask geometrical characteristics were also proven to play an important role in the final GaN NW formation. Numerical simulations focused on the kinetics occurring on the surface, during the initial growth stages, identified the significance of the mask's geometrical characteristics, and revealed

an interaction between the windows that affects the formation of GaN NW arrays.

Finally, the conclusions of this work, together with some future prospects are presented in the final chapter, Chapter 10.

Bibliography

- [1] ARAFIN, S., LIU, X., AND MI, Z. "Review of recent progress of III-nitride nanowire lasers". *Journal of Nanophotonics* 7 (2013), 074599.
- [2] BEHZADIRAD, M., NAMI, M., RISHINARAMAGALAM, A. K., FEEZELL, D. F., AND BUSANI, T. "GaN nanowire tips for nanoscale atomic force microscopy". *Nanotechnology* 28 (2017), 20LT01.
- [3] GACEVICA, Z., LOPEZ-ROMERO, D., MANGAS, T. J., AND CALLEJA, E. "A top-gate GaN nanowire metalsemiconductor field effect transistor with improved channel electrostatic control ". *Appl. Phys. Lett.* 108 (2016), 033101.
- [4] GUO, W., ZHANG, M., BANERJEE, A., AND BHATTACHARYA, P. "Catalyst-Free InGaN/GaN Nanowire Light Emitting Diodes Grown on (001) Silicon by Molecular Beam Epitaxy". *Nano Lett.* 10 (2010), 3355.
- [5] KIM, S., PARK, J. Y., CHLOI, S., KIM, H. S., NA, H. G., YANG, J. C., LEE, C., AND KIM, H. W. "Room temperature sensing properties of networked GaN nanowire sensors to hydrogen enhanced by the Ga₂Pd₅ nanodot functionalization". *Int. J. Hydr. Energy* 36 (2011), 2313.
- [6] KRUSE, J. E., LYMPERAKIS, L., EFTYCHIS, S., ADIKIMENAKIS, A., DOUNDOULAKIS, G., TSAGARAKI, K., ANDROULIDAKI, M., OLZIER-SKY, A., DIMITRAKIS, P., IOANNOU-SOUGLERIDIS, V., NORMAND, P., KOUKOULA, T., KEHAGIAS, T., KOMNINO, P., KONSTANTINIDIS, G., AND GEORGAKILAS, A. "Selective-area growth of GaN nanowires on SiO₂-masked Si (111) substrates by molecular beam epitaxy". *J. Appl. Phys.* 119 (2016), 224305.
- [7] KUMARESAN, V., LARGEAU, L., MADOURI, A., GLAS, F., ZHANG, H., OEHLER, F., CAVANNA, A., BABICHEV, A., TRAVERS, L., GOGNEAU, N., TCHERNYCHEVA, M., AND HARMAND, J.-C. "Epitaxy of GaN Nanowires on Graphene". *Nano Lett.* 16 (2016), 4895.

- [8] NGUYEN, H. P. T., CHANG, Y.-L., SHIH, I., AND MI, Z. "InN p-i-n Nanowire Solar Cells on Si". *IEEE JOURNAL OF SELECTED TOPICS IN QUANTUM ELECTRONICS* 17 (2011), 1062.
- [9] SANCHEZ-GARCIA, M., CALLEJA, E., MONROY, E., SANCHEZ, F., AND E. MUNOZ, F. C., AND BERESFORD, R. "The effect of the III/V ratio and substrate temperature on the morphology and properties of GaN- and AlN-layers grown by molecular beam epitaxy on Si(111)". *J. Cryst. Growth* 183 (1998), 23.
- [10] SCHUSTER, F., FURTMAYR, F., ZAMANI, R., MAGEN, C., MORANTE, J. R., ARBIOL, J., GARRIDO, J. A., AND STUTZMANN, M. "Self-Assembled GaN Nanowires on Diamond". *Nano Lett.* 12 (2012), 2199.
- [11] TRAMPERT, A., RISTIC, J., JAHN, U., CALLEJA, E., AND PLOOG, K. H. "TEM study of (Ga,Al)N nanocolumns and embedded GaN nanodiscs". *Inst. Phys. Conf. Ser.* 180 (2003), 167.
- [12] VAN TREECK, D., CALABRESE, G., GOERTZ, J. J. W., KAGANER, V. M., BRANDT, O., FERNANDEZ-GARRIDO, S., AND GEELHAAR, L. "Self-assembled formation of long, thin, and uncoalesced GaN nanowires on crystalline TiN films". *Nano Res.* 11 (2018), 565.
- [13] YOSHIZAWA, M., KIKUCHI, A., FUJITA, N., KUSHI, K., SASAMOTO, H., AND KISHINO, K. "Self-organization of GaN/Al_{0.18}Ga_{0.82}N multi-layer nano-columns on (0001) Al₂O₃ by RF molecular beam epitaxy for fabricating GaN quantum disks". *J. Cryst. Growth* 189/190 (1998), 138.

Properties of III-Nitride semiconductors

2.1 Band structure

III-Nitride semiconductor materials consist of elements from group III (Al, Ga and In) and N from the V group of the Periodic Table of Elements. They can form binary (AlN, GaN, InN), ternary ($In_xGa_{1-x}N$, $Al_xGa_{1-x}N$, $In_xAl_{1-x}N$) and quaternary ($In_xAl_yGa_{1-x-y}N$) compounds. Their high thermal conductivity, high breakdown fields (GaN, AlN), wide direct band gap, chemical stability and resistance to chemical corrosion are only some of the properties that have placed the III-Nitride family in the center of technological research in the last 30 years [12, 13, 15].

Their direct band gap covers an energy region from deep ultraviolet (6.2 eV) to infrared (0.65 eV) which is a much wider range compared to III-Arsenide and III-Phosphide semiconductors (Fig. 2.1). The value of the band gaps for AlN, GaN and InN are 6.2 eV [2], 3.4 eV [2] and 0.65 eV [14] respectively. Nitride alloys that combine different amounts of Al, In and Ga, have band gaps among the above values. For alloys of the form $In_xAl_yGa_{1-x-y}N$, this band gap value can be approximated by

$$E_g(x, y) = xE_g^{InN} + yE_g^{AlN} + (1 - x - y)E_g^{GaN} - xb^{InN}(1 - x) - yb^{AlN}(1 - y) \quad (2.1)$$

where $E_g(x, y)$ is the band gap value of the alloy, and b^{InN} and b^{AlN} are the bowing parameters for In and Al compounds respectively [11, 20].

The tunability of the band gap in nitrides makes them ideal for optoelectronic applications such as light emitting devices (LED), laser diodes (LD), solar cells, ultraviolet and infrared detectors. Recently (2014) the physics Nobel prize was awarded to Isamu Akasaki, Hiroshi Amano and Shuji Nakamura, acknowledging their work on III-Nitrides for efficient blue LEDs [1].

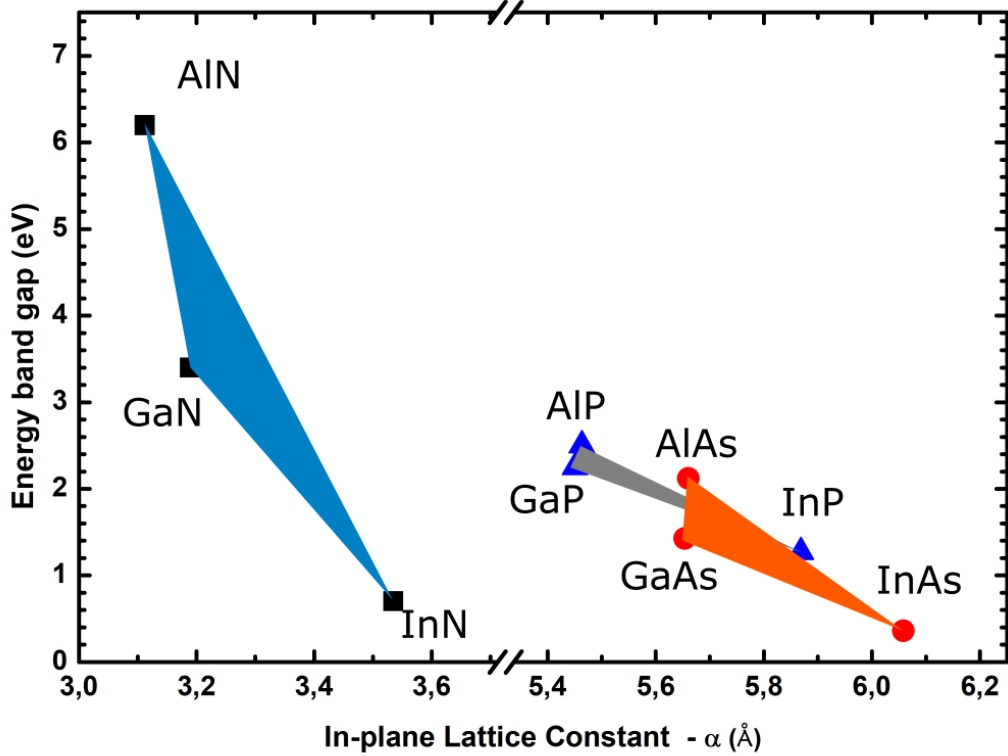


Figure 2.1: The areas covered by III-Nitride (blue-shaded), III-Arsenide (orange-shaded) and III-Phosphite (gray-shaded) groups in the Energy band gap – α -Lattice constant plane.

2.2 Crystal structure

The crystal structure of the III-Nitride materials can be either wurtzite (hexagonal) or zincblende (cubic). The wurtzite crystal structure is the most thermodynamically stable [13]. The zincblende structure can result from growing nitrides on cubic structures.

In both the wurtzite and zincblende structures, each group III atom is linked with four N atoms with covalent bonds, and each N atom with four group III atoms [9]. The wurtzite structure has a hexagonal closed pack (hcp) arrangement, and the layer stacking in the [0001] direction follows an AB AB AB sequence (Fig. 2.2.a). For the zincblende structure, the layer stacking follows an ABC ABC ABC sequence, as shown in Fig. 2.2.b.

The hexagonal structure is described by the lattice parameters a , which is the side length of the hexagon, and c , which is the height of the hexagonal

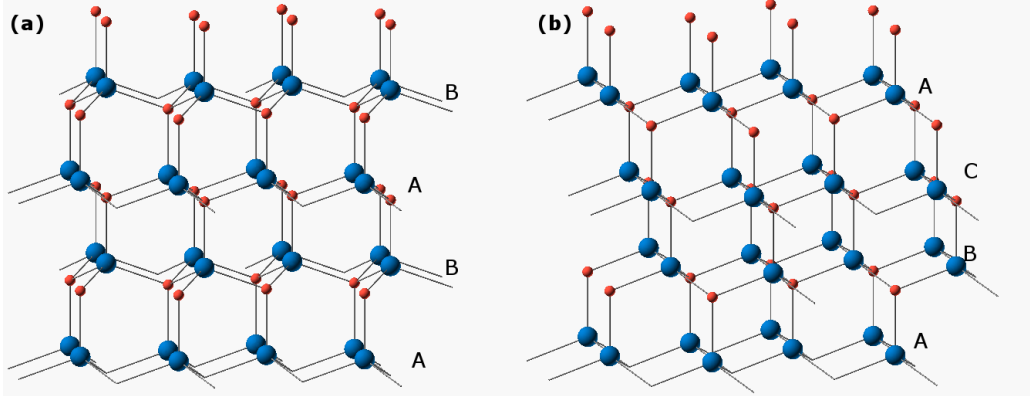


Figure 2.2: (a) The wurtzite structure, showing the AB AB stacking. (b) The zincblende structure, showing the ABC ABC stacking.

	GaN	AlN	InN
c (Å)	5.185 [17]	4.982 [17]	5.699 [5]
a (Å)	3.189 [17]	3.112 [17]	3.535 [5]
b (Å)	0.376 [2]	0.380 [2]	0.377 [2]

Table 2.1: Showing the values of the wurtzite crystal lattice, c , a and b , for GaN, AlN and InN

prism (Fig. 2.3.a.). The wurtzite structure can be described as two hexagonally close packed arrangements, one of the III-element and one of N atoms, that are displaced by a vertical distance equal the length of the covalent bond, b , between the group III and the N atoms in the $[0001]$ direction. The lattice constant values a , c and the III-N covalent bond length b for GaN, AlN and InN can be found in Table 2.1 [2, 5, 17]. For ternary and quaternary compounds, Vegards law is used for the calculation of the lattice constant [4]. According to this, the lattice constant a of a compound of $In_xAl_yGa_{1-x-y}N$ is given by:

$$a_{\text{alloy}}(x, y) = xa_{\text{InN}} + ya_{\text{AlN}} + (1 - x - y)a_{\text{GaN}} \quad (2.2)$$

In Fig. 2.3.b some of the main planes of the wurtzite crystal structure are noted. These planes are the c -plane, the m -plane, the a -plane and the r -plane, indexed as $\{0001\}$, $\{1\bar{1}00\}$, $\{11\bar{2}0\}$ and $\{1\bar{1}02\}$ respectively [9].

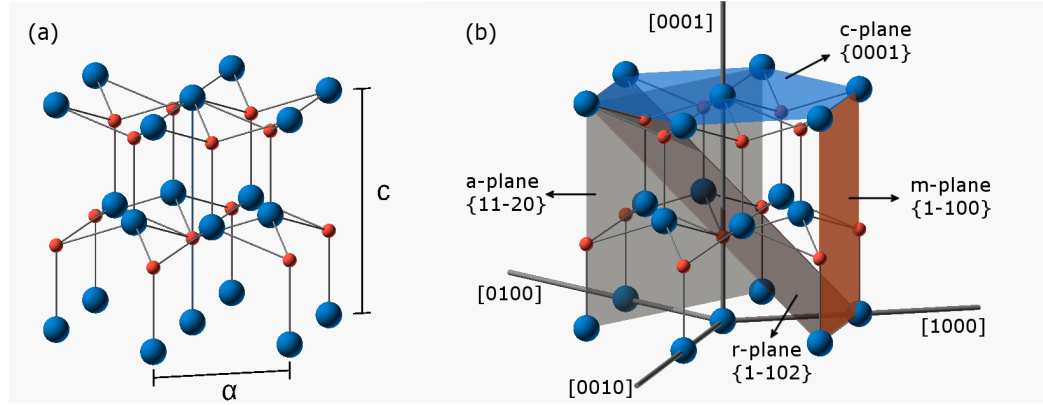


Figure 2.3: (a) The hexagonal structure of wurtzite, depicting the dimensions a and c . (b) The c -plane, m -plane, a -plane and r -plane are depicted in the hexagonal wurtzite cell. Blue spheres (larger) represent Ga atoms, and red spheres (smaller) represent N atoms

2.3 Polarity - Polarization

The wurtzite structure has a non-inversion symmetry, that is present in the c -axis. Due to this, there are different polar directions. The $[0001]$ direction conventionally is defined as the vector pointing from the III-atom (anion) towards the N-atom (cation), the positive direction of the c -axis. The $[000\bar{1}]$ direction is pointing from the N-atom towards the III-atom. III-polar structures are defined as the structures that are grown towards the $[0001]$ direction, while N-polar structures are defined as those that grow towards the $[000\bar{1}]$ direction. Different polarities have different results in the growth of films and in the properties of the crystal [8, 21]. For example, different polarity films present different surface morphologies and favor or hinder the formation of threading dislocations (Ga-polar films present a smoother surface compared to the N-polar films [18, 19]. Additionally, polarity has consequences on the incorporation rate of impurities [6], in the defect formation [3, 10, 16] and in adatom mobility [22].

Due to the strong ionicity of the covalent bond, strong polarization fields are manifested inside the crystal that affect its electrical and optical properties [2, 7]. The total polarization, P is a sum of spontaneous and piezoelectric polarizations. The spontaneous polarization is a property of the III-nitrides, and becomes possible due to the non-inversion symmetry in combination with the strong ionicity of the covalent bond. Uneven distributions of the valence electrons along the c -axis result in a spontaneous polarization field with direction parallel to the $[000\bar{1}]$ direction. The piezoelectric polarization

is a result of strain in the crystal, that causes the atoms of the III-Nitrides to shift from their position in a relaxed wurtzite cell.

Bibliography

- [1] http://www.nobelprize.org/nobel_prizes/physics/laureates/2014, 2014.
- [2] AMBACHER, O. "Growth and applications of Group III-nitrides". *J. Phys. D: Appl. Phys.* 31 (1998), 2653.
- [3] COULON, P. M., MEXIS, M., TEISSEIRE, M., JUBLOT, M., EGUE'S, P. V., LEROUX, M., AND ZUNIGA-PEREZ, J. "Dual-polarity GaN micropillars grown by metalorganic vapour phase epitaxy: Cross-correlation between structural and optical properties". *J. Appl. Phys.* 115 (2014), 153504.
- [4] DENTON, A. R., AND ASHCROFT, N. W. "Vegards law". *Phys. Rev. A* 43 (1991), 3161.
- [5] DIMAKIS, E. "*Physical Mechanisms in Molecular Beam Epitaxy and Properties of InN (0001) Films*". PhD thesis, University of Crete, Physics Department, 2007.
- [6] DUFF, A. I., LYMPERAKIS, L., AND NEUGEBAUER, J. "Understanding and controlling indium incorporation and surface segregation on In_xGa_{1-x}N surfaces: An ab initio approach". *Phys. Rev. B* 89 (2014), 085307.
- [7] FIORENTINI, V., BERNARDINI, F., SALA, F. D., CARLO, A. D., AND LYGLI, P. "Effects of macroscopic polarization in III-V nitride multiple quantum wells". *Phys. Rev. B* 60, 12 (1999), 8849.
- [8] HELLMAN, D. "The Polarity of GaN: a Critical Review". *MRS Internet Journal of Nitride Semiconductor Research* 3 (2014).
- [9] HENINI, M., Ed. "*Molecular Beam Epitaxy - From research to mass production*", 1 ed. Elsevier, Nov 2012.

- [10] KIRSTE, R., COLLAZO, R., CALLSEN, G., WAGNER, M. R., KURE, T., REPARAZ, J. S., MITA, S., XIE, J., RICE, A., TWEEDIE, J., SITAR, Z., AND HOFFMANN, A. "Temperature dependent photoluminescence of lateral polarity junctions of metal organic chemical vapor deposition grown GaN". *J. Appl. Phys.* 110 (2011), 093503.
- [11] MCCLUSKEY, M., DE WALLE, C. G. V., MASTER, C. P., ROMANO, L. T., AND JOHNSON, N. M. "Large band gap bowing of $In_xGa_{1-x}N$ alloys". *Appl. Phys. Lett.* 72 (1998), 2725.
- [12] MORKOC, H. "*Handbook of Nitride Semiconductors and Devices*", vol. 1. Wiley-VCH Verlag GmbH & Co. KGaA, Weinheim, May 2008.
- [13] MOUSTAKAS, T. D. "*Gallium Nitride (GaN)*", 2 ed., vol. 57 of *Semiconductors and Semimetals*. Academic Press, Oct 1999.
- [14] ORTI, E., BREDAS, J., CLARISSE, C., WU, D., WALUKIEWICZ, W., SHAN, W., YU, K. M., AND III, J. W. A. "Temperature dependence of the fundamental band gap of InN". *J. Appl. Phys.* 94 (2003), 4457.
- [15] RUTERANA, P., ALBRECHT, M., AND NEUGEBAUER, J., Eds. "*Nitride Semiconductors: Handbook on Materials and Devices*". Wiley-VCH Verlag GmbH & Co. KGaA, 2016.
- [16] SCHUCK, P. J., MASON, M. D., GROBER, R. D., AMBACHER, O., LIMA, A. P., MISKYS, C., DIMITROV, R., AND STUTZMANN, M. "Spatially resolved photoluminescence of inversion domain boundaries in GaN-based lateral polarity heterostructures". *Appl. Phys. Lett.* 79 (2001), 952.
- [17] STRITE, S., AND MORKOC, H. "GaN, AlN and InN: A review". *Journal of Vacuum Science & Technology B: Microelectronics and Nanometer Structures Processing, Measurement, and Phenomena* 10 (1992), 1237.
- [18] STUTZMANN, M., AMBACHER, O., EICKHOFF, M., KARRER, U., PIMENTA, A. L., NEUBERGER, R., SCHALWIG, J., DIMITROV, R., SCHUCK, P., AND GROBER, R. D. "Playing with Polarity". *Phys. Status Solidi B* 228, 2 (2001), 505.
- [19] SUMIYA, M., YOSHIMURA, K., ITO, T., OHTSUKA, K., FUKU, S., MIZUNO, K., YOSHIMOTO, M., KOINUMA, H., OHTOMO, A., AND KAWASAKI, M. "Growth mode and surface morphology of a GaN film deposited along the N-face polar direction on c-plane sapphire substrate". *J. Appl. Phys.* 88 (2000), 1158.

- [20] WU, J., WALUKIEWICZ, W., YU, K. M., III, J. W. A., LI, S. X., HALLER, E. E., LU, H., AND SCHAFFD, W. J. "Universal bandgap bowing in group-III nitride alloys". *Solid State Communications* 127 (2003), 411.
- [21] ZUNIGA-PEREZ, J., CONSONNI, V., LYMPERAKIS, L., KONG, X., TRAMPERT, A., FERNANDEZ-GARRIDO, S., BRANDT, O., RENEVIER, H., KELLER, S., HESTROFFER, K., WAGNER, M. R., REPARAZ, J. S., AKYOL, F., RAJAN, S., RENNESSON, S., PALACIOS, T., AND FEUILLET, G. "Polarity in GaN and ZnO: Theory, measurement, growth, and devices". *Appl. Phys. Rev.* 3, 4 (2016), 041303.
- [22] ZYWIETZ, T., NEUGEBAUER, J., AND SCHEFFLER, M. "Adatom diffusion at GaN (0001) and (000 $\bar{1}$) surfaces". *J. Appl. Phys.* 73 (1998), 487.

Experimental Methods

This chapter presents the basics of the experimental methods, instruments and experimental setups that were used in this work. Initially we describe the molecular beam epitaxy (MBE) method for semiconductors' growth, followed by the experimental methods that were used for sample characterization, i.e. electron microscopy techniques, atomic force microscopy (AFM), photoluminescence (PL) and X-ray diffraction (XRD).

3.1 Molecular Beam Epitaxy

MBE uses accurate control of molecular or atomic beam flow, to deposit crystalline material onto a crystalline substrate, whose temperature is precisely controlled. This can result in the growth of ultra-thin epitaxial layers, or the growth of 3 dimensional (3D) structures. Deposition is performed in a high vacuum (HV) environment (10^{-5} Torr or higher) with background pressure in the ultra HV (UHV) range of 10^{-11} Torr, resulting in excellent crystal quality. All the above capabilities, in combination with in-situ tools used for sample characterization, have defined the MBEs' leading role in the production of high-quality semiconductor materials and devices.

3.1.1 Molecular Beam Epitaxy Vacuum Chambers

The system that was used is the MBE 32P RIBER. It is comprised of 4 vacuum chambers that are used for smooth operation. These chambers are: the load chamber, the degas chamber, the transfer chamber and the growth chamber. They are separated with gate valves, isolating one from the other, and each vacuum chamber has its own vacuum pump system. This way, simultaneous operations that use different vacuum chambers are possible, i.e. while a sample is growing in the growth chamber, a substrate can be degassed in the degas chamber, while other substrates, ready to be grown,

or to be degassed, are in the transfer chamber.

Initially, an 8-position cassette with substrates is loaded in the load chamber, which is the only chamber that comes in direct contact with the laboratory atmosphere. At this point it should be pointed out that the laboratory atmosphere is a controlled clean room environment (class 1000). The loaded substrates have been previously cleaned using a standard chemical process to remove any organic and inorganic contaminants. Then the chamber, which is equipped with a turbomolecular pump, is pumped down to 10^{-6} Torr. The degas chamber is attached to the load chamber.

The degas chamber is equipped with a degas heater, for degassing substrates in high vacuum conditions. This is a necessary procedure prior to any deposition on the surface of the substrate. Degassing sublimes residual atoms from the substrate surface, that may have originated from chemical cleaning, or from the clean room environment. Additionally to the cleanliness of the surface, this procedure also protects the ultra high vacuum in the growth chamber from the sublimated atoms. The degas vacuum chamber is continuously pumped by a turbomolecular pump. The pressure is measured by an ion gauge, and can reach ultra high vacuum (UHV) values of 10^{-11} Torr.

The transfer chamber separates the degas chamber from the growth chamber. The cassette with substrates is positioned in this chamber while procedures that use other vacuum chambers are ongoing, i.e. degassing a substrate or growing a sample. The chamber is pumped with an ion pump and a Ti-sublimation pump, that preserves UHV. The pressure is measured by an ion gauge. The presence of this chamber additionally helps in preserving the UHV in the growth chamber, which is the next chamber attached. The sublimated residuals that may pass from the degas chamber to the transfer chamber, during transfer of substrates, will be pumped in the transfer chamber before opening the gate valve between transfer and growth chamber, preserving in this way the purity of the growth chamber.

The deposition on the surface occurs in the growth chamber. A schematic of this chamber is shown in Fig. 3.1. It is equipped with: effusion cells, a radio frequency plasma source for the production of the reactive nitrogen beam, and an electron gun and a fluorescent screen for reflection high energy electron diffraction (RHEED) observations. Additionally there is a quadrupole mass spectrometer (QMS), for monitoring the different molecules that are present in the chamber, and a manipulator that allows for heating up to 850°C , and continuous rotation of the sample during the deposition process.

This chamber, uses a combination of pump methods for achieving UHV. A turbomolecular pump, supported by a smaller turbomolecular pump and a diaphragm pump is used, capable of pumping up to 1800 L/s. Additionally,

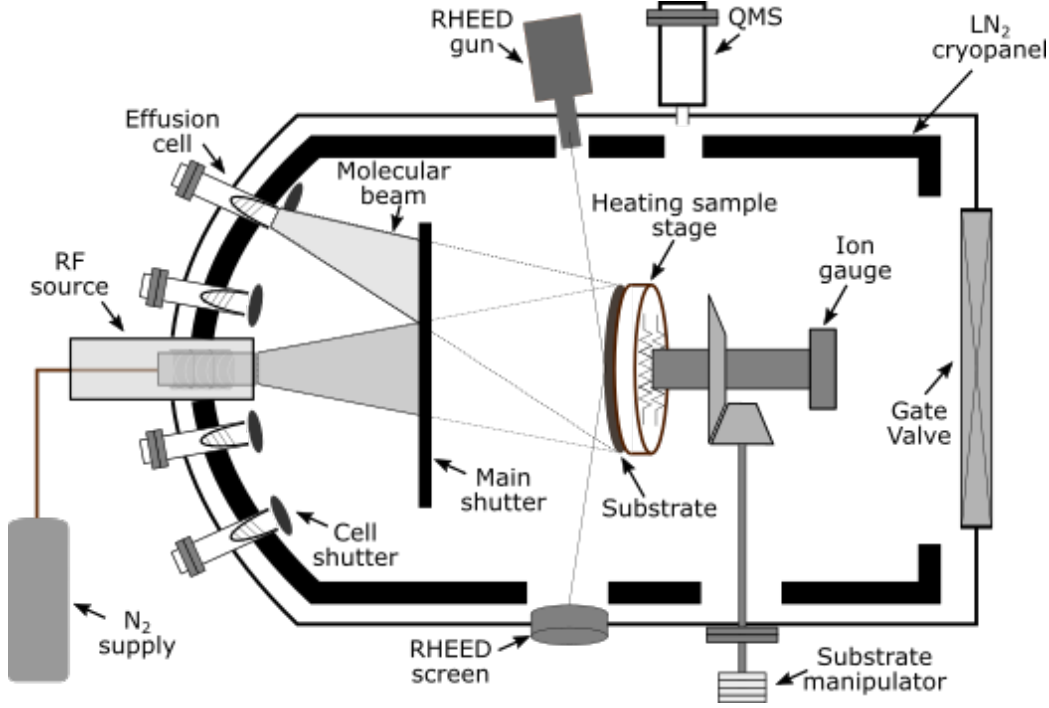


Figure 3.1: Schematic drawing of a plasma-assisted molecular beam epitaxy growth chamber, used for growing III-nitride semiconductors.

the chamber is equipped with a Titanium sublimation pump, effective for the more reactive components of the residual gas (O_2 and CO), as well as an ion pump capable of preserving vacuum up to 10^{-11} Torr. Furthermore, the system uses liquid nitrogen (LN_2) cryopanel, that are effective in the pumping procedure through gas adsorption on the surface of the panels. The LN_2 cryopanel also provide heat extraction and thermal insulation between the different heating elements of the chamber.

The UHV achieved in the growth chamber is well within the molecular beam regime. This means that the mean free path of the molecules is larger than the critical length of the system. This critical length is the distance between the effusion cell and the substrate, and in most of the MBE growth chambers is equal to 0.15-3 cm. The average mean free path, λ , is given by [6, 7]:

$$\lambda = \frac{k_B T}{\sqrt{2\pi} p D^2} \quad (3.1)$$

where k_B , T , p and D denote Boltzmann's constant, the growth chamber temperature, the pressure and the diameter of molecules, respectively. The mean

free path for Ga atoms, in typical growth conditions¹ is 0.96 m, well within the molecular beam regime. Additionally to the molecular beam regime of operation, the UHV also minimizes the presence of impurities and allows for samples of better crystal quality and high purity.

3.1.2 Radiofrequency Plasma source

The growth of III-Nitrides requires a source of nitrogen, that is used in combination with the atoms from the III group. Due to the inert nature of N₂, different methods are used that result in energetic nitrogen species. These methods include the microwave electron cyclotron plasma source and the radio-frequency plasma source. The combination of a nitrogen plasma source with the MBE is called Plasma-Assisted MBE (PAMBE), and is the method that was used. For the production of plasma, an RF-plasma source was used. N₂ inert gas is introduced in a pyrolytic boron nitride (PBN) cavity. Then it is inductively coupled through a water-cooled copper coil with RF energy at 13.56 MHz. This creates a plasma, and transforms the nitrogen molecules to excited molecules (N₂^{*}), ionized molecules (N₂⁺), excited atoms (N^{*}) and ionized atoms (N⁺). The plasma is contained in a PBN discharge tube that is capped with a PBN exit plate that contains many tiny holes [8]. The final composition of the active nitrogen beam depends on the input power and gas flow, both of which have significant effects on the growth procedure [4].

3.1.3 Effusion cells

Effusion cells are used in MBE, for the precise control of molecular or atomic beams. They are based on the works of Martin Knudsen [12, 13] and Langmuir [15] (for a concise description of their work the reader is referred to [9]). Although the term "Knudsen cell" originally referred to a cell used to measure the mass that evaporates [14], the term is widely used as a synonym to an effusion cell.

Effusion cells are small crucibles that contain high purity material such as Ga, Al, Si, and allow for accurate flow control through thermal evaporation or sublimation. The crucibles are uniformly heated, and they are usually made from high purity PBN or graphite. The cells can reach very high temperatures (up to ~1500 °C), providing a high flux. The temperature is regulated by close-loop controllers, establishing a stable flux. These two flux characteristics ensure high and stable growth rates [6].

¹for p=10⁻⁴ Torr, T = 300 K, D = 2.7 Å

The flux Φ_e coming out of a crucible, as calculated by the Knudsen [12, 13, 14] and Langmuir [15] theories, is given by:

$$\Phi = A_e p(T) \left(\frac{N_a}{2\pi M k_B T} \right)^{\frac{1}{2}} \quad (3.2)$$

where A_e is the opening surface of the crucible, $p(T)$ is the equilibrium pressure of the evaporant at a temperature T , N_a is the Avogadro number, M is the molecular weight of the evaporating species, k_B is the Boltzmann constant, and T is the absolute temperature. For this equation to hold, the liquid/solid and vapor phase must be in equilibrium. However, due to the large opening of the effusion cell (in order to achieve higher fluxes [6]) this condition does not hold.

The real flux is highly dependent on the geometrical factors of the crucible, such as the shape of the crucible, the size of the opening and the height to diameter ratio. Furthermore, the useful flux coming from an effusion cell is the one that reaches the surface of the substrate. So, additional factors such as the distance and the angle between the crucible and the substrate play a crucial role. For the above reasons, the beam flux is determined from its equivalent pressure measured by an ion gauge. The gauge is located behind the heating sample stage (Fig. 3.1), and can rotate towards the cells, having the same position as the substrate when growing. This results in measurements of the beam's equivalent pressure that correspond to the flux reaching the surface of the samples.

3.1.4 Physical processes of MBE - Surface kinetics

Molecular beam epitaxy is governed by the kinetics of the atoms impinging on the surface of the sample. The main processes that occur are illustrated in Fig. 3.2 [7, 16]. Initially, impinging atoms can adsorb to the surface, interacting with the surface atoms. Adsorption can occur either through weak Van der Waals forces, a process also called physisorption, or by forming stronger chemical bonds (i.e. covalent or ionic), also called chemisorption. The adsorbed atoms can diffuse on the surface, until (i) they are incorporated to the crystal, or (ii) they are desorbed back in the growth chamber vacuum. Additionally to the above, decomposition of the atoms of the crystal also occurs, where atoms from the crystal can also either desorb, or diffuse on the surface, following the procedure described above [7, 16].

Incorporation of the atoms occurs through chemisorption at nucleation sites, reducing the dangling bonds of the surface, and thus reducing the total surface energy. These nucleation sites can be considered as imperfections of the surface [3, 10]. The number of bonds that are formed between the

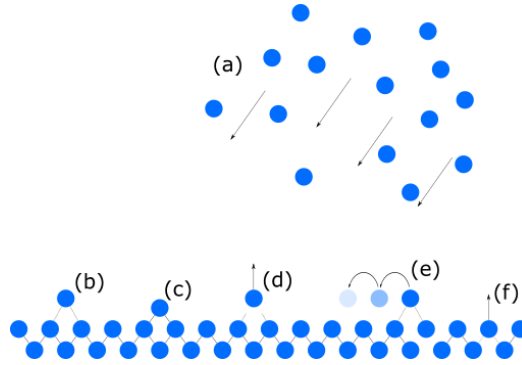


Figure 3.2: Schematics of the basic processes that occur during molecular beam epitaxy: (a) atoms impinging, (b) physisorption, (c) incorporation (chemisorption), (d) desorption, (e) diffusion and (f) decomposition of the crystal

chemisorbed atom and the nucleation site define the preference of atoms nucleating at the specific sites [3, 10]. The main possible sites, as can be seen in Fig. 3.3, beginning from the less favourable are:

1. on the surface of a sample,
2. on the edge of a step,
3. in a kink that is formed in a step,
4. in a vacancy on the edge of a step and
5. in a vacancy on the surface

Atoms being adsorbed on the surface of a crystal, can become nucleation sites, resulting in nucleous that are formed on the surface (Fig. 3.3.1). If the size of the nucleous is larger than a critical size, it can grow further and create 2D islands, or 3D clusters [1, 3, 19]. Otherwise, if the size is smaller than the critical size, it will dissolve.

All the above kinetics of the adatoms depend in every case on the growth conditions. These conditions are the impinging flux, the temperature of the substrate, the surface of the substrate and the lattice constant and the impinging flux ratio in the case of two or more depositing elements.

Epitaxial growth of thin films can be classified into three different growth modes (Fig. 3.4) [7, 18]

1. layer by layer or Frank van de Merwe growth mode (Fig. 3.4.a). The atoms that diffuse on the surface are attracted to the substrate more than among themselves, resulting in a 2D growth of the film.
2. island or Volmer Weber growth mode (Fig. 3.4.b). The atoms are attracted strongly between them, and create 3D clusters. These 3D

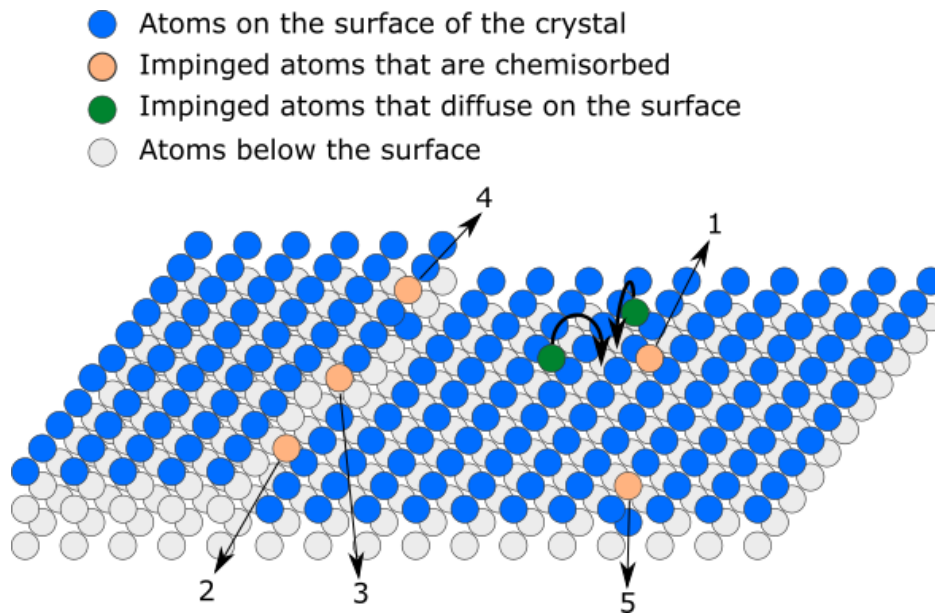


Figure 3.3: Showing the possible positions of adsorbed atoms to form chemical bonds on the surface. Atoms can be chemisorbed: (a) on the surface of the sample, (b) the edge of a step, (c) in the kink, (d) in a vacancy on the edge of a step and (e) in a vacancy on the surface. In the case of (1) diffusion can lead to further aggregation of atoms on the surface.

clusters later coalesce and form a film.

3. layer plus island or Stranski Krastanov growth mode (Fig. 3.4.c). In this growth mode, the atoms initially grow in a 2D growth of a thin layer, and later on top of the film they form 3D clusters. This can occur when the first layers are strained.

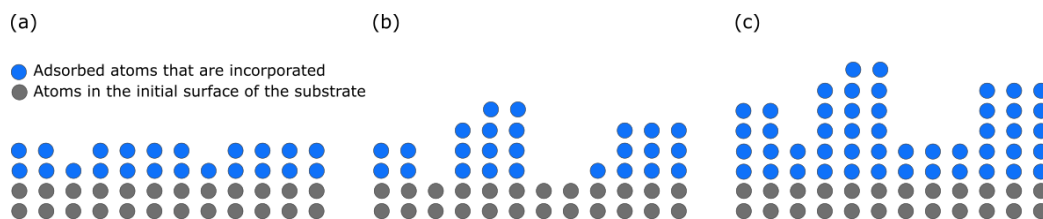


Figure 3.4: Showing the three different growth modes: (a) Frank-van der Merwe mode, layer by layer growth, (b) Volmer-Weber mode, island growth, and (c) Stranski-Krastanov mode, layer plus island growth.

The distinction of the three growth modes is better understood over a

discussion of the local surface and interface energies per unit area, in combination with accumulated strain in the growing layers [16]. The surface energy per unit area, γ , is defined as the reversible work, dW , needed to increase the surface of a material by dA :

$$\gamma = \frac{dW}{dA} \quad (3.3)$$

In the case of epitaxy, one can define γ_{sub} and γ_{dep} as the surface energy per unit area of the substrate, and of the deposited material respectively. In a similar way, γ_{int} is defined as the interface energy per unit area between the substrate and the material that is deposited. These quantities are related to the binding energy, and to the number of bonds included in a surface dA .

The growth mode of the initial layers is defined from the relation among these quantities. One can define the quantity $\Delta\gamma = \gamma_{dep} + \gamma_{int} - \gamma_{sub}$. For the case where $\Delta\gamma < 0$, then $\gamma_{sub} < \gamma_{dep} + \gamma_{int}$, and the growth will proceed in a layer by layer mode, at least for the first layers. In the case of a different lattice constant among the substrate and the epitaxial material, then accumulation of strain can lead to 3D growth mode (Stranski-Krastanov growth mode). Otherwise, the growth will continue layer by layer (Frank van der Merwe growth mode). For the case where $\Delta\gamma > 0$, then $\gamma_{sub} > \gamma_{dep} + \gamma_{int}$, and the growth will proceed with the formation of 3D clusters (Volmer-Weber growth mode) [3, 16].

3.2 Characterization methods

3.2.1 RHEED: An in-situ surface characterization technique

In MBE systems, in-situ characterization of the surface during growth is possible through a number of techniques [6, 7]. These methods include Auger electron spectroscopy, secondary ion mass spectroscopy, X-ray photoemission spectroscopy, ultra violet photoemission spectroscopy and reflection high electron diffraction (RHEED) [11]. The latter was used in this work, and will be described in the following section.

The RHEED setup is described in Fig. 3.5 [7, 11]. An electron gun produces a high energy electron beam through a heated wolfram filament, that is used as a cathode. Electrons are then accelerated towards the anode, that has 15 kV higher potential. This results in electrons with a De-Broglie wavelength of $\sim 1\text{\AA}$, thus allowing for a high distinctive ability. The electrons form a beam, that is further collimated through a set of electromagnets.

Eventually the electron beam with a spot size between $0.5-1 \cdot 10^{-3}\text{m}$ is directed towards the surface of the sample. The incident angle of the directed beam is about $1-2^\circ$, and covers a surface of $0.45-0.9 \text{ cm}^2$ on the sample. The diffracted beam is directed towards a phosphorus screen, where diffraction patterns become visible (Fig. 3.5). The very small penetration length of the electron beam, makes this technique sensitive to the first layers of the surface [11].

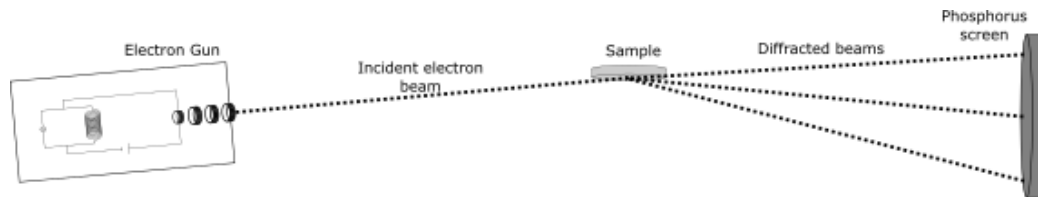


Figure 3.5: RHEED setup diagram

For a better understanding of the information that RHEED patterns provide, some basic concepts are necessary. The reciprocal space of a smooth surface, is made of parallel rods normal to the surface of the substrate. The Ewald sphere has a radius equal to the wavelength of electrons of the incident beam. The section of the reciprocal space of the crystal and the Ewald sphere defines the necessary condition for constructive diffraction, and constitutes the RHEED pattern that is visible in the phosphorus screen (Fig. 3.6). Both the rods and the Ewald sphere have a finite thickness. The rods due to thermal vibrations of the atoms, and crystal defects, and the Ewald sphere due to energy dispersion of the electrons [11]. The radius of the Ewald sphere is larger than the distance between the rods, so it intersects many parallel rods, and due to the finite thickness, the intersection is a region along the rods, and not a single spot. This results in a streaky pattern (Fig. 3.7.a).

In the case of 3D structures, the electron beam diffracts while it is transmitted through them, and results in spotty patterns (Fig. 3.7.b). In the case of a rough surface, or when 3D structures start to form, then the pattern is both streaky and spotty (Fig. 3.7.c).

3.2.2 Electron Microscopy

Scanning Electron Microscopy (SEM)

Scanning electron microscopy (SEM) is a technique widely used for observing morphological characteristics of samples in the nano-scale by using a focused electron beam. Production of electrons is usually done through thermionic emission [2, 5]. The electrons are accelerated with energies up to 40 kV

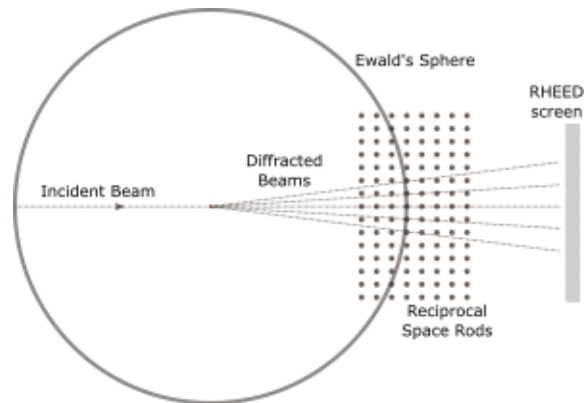


Figure 3.6: Schematic representation of the inverse space, and the Ewald's sphere. The section of the Ewald's sphere with the rods of the surface atoms is the RHEED pattern

and are focused through a combination of electromagnets. This results in an electron wavelength of 5×10^{-2} Å, that in combination with the electron optical system, allows for resolutions up to ~ 10 Å or better.

As the name implies, the electron beam scans the sample that is loaded in a vacuum chamber. The electrons collide with the sample, and produce various particles such as backscattering electrons, secondary electrons, Auger electrons, transmitted electrons and X-rays. The sample must be conductive, in order to avoid electron charge effects. The final SEM micrograph results from information of emitted particles (mainly the secondary electrons), in combination with the position that these particles are produced, that is defined by the location of the beam. Due to the very small spot size, a very wide depth of field is achieved, that allows for a better understanding of the 3D structure of the sample. The magnification of the sample can vary between 10-500000 times, making this tool valuable in microelectronics laboratories.

High resolution SEM systems employ electron beams produced through field- effect (FE) emission. The SEM used in this work was the JEOL 7000F FE-SEM microscope, and all the SEM observations on the grown samples were carried out by Katerina Tsagaraki.

Transmission electron microscopy

Another microscopy technique that uses an electron beam is the Transmission electron microscopy (TEM) [2]. This method uses electrons that are accelerated through a cathode with energies between 200-1000 keV, giving them speeds near the speed of light, allowing for a significantly larger resolution than SEM. In this technique, the electron beam is transmitted through

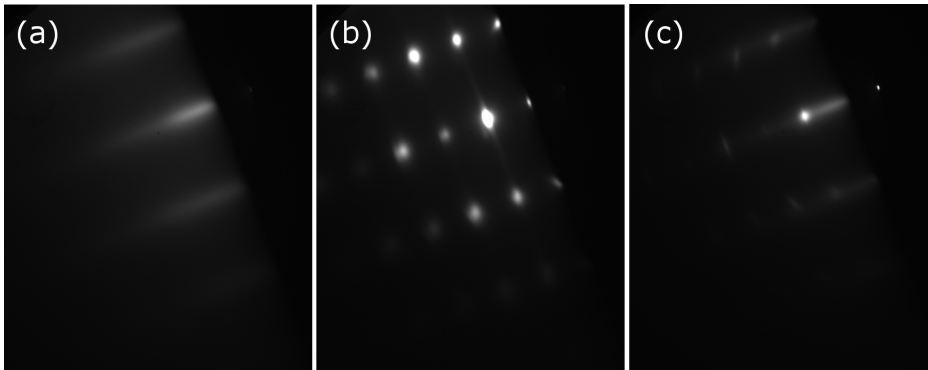


Figure 3.7: RHEED patterns that show (a) a streaky, (b) a spotty and (c) a streaky with spotty pattern, that correspond to (a) a smooth surface, (b) 3D structures and (c) a rough surface or small 3D structures that started nucleating.

an ultra-thin sample (of the order of 100 nm), and then focused in a back focal plane, producing the diffracted pattern. This pattern represents the reciprocal space of the crystal. Then, using appropriate lenses, the user can switch from reciprocal space imaging to real space imaging. The characterization with TEM that will be presented in this thesis, was performed in the Aristotle university of Thessaloniki, in collaboration with Prof. Philomela Komninou and Prof. Thomas Kehagias, and Dr. Triantafyllia Koukoula.

3.2.3 Photoluminescence Spectroscopy

Photoluminescence spectroscopy (PL) is a technique that uses optically-induced electron excitation in order to get information for the electronic structure of the sample. A laser beam is incident on the surface of the sample, and excites electrons from their equilibrium states [2]. Electrons return to their equilibrium state, either through a radiative, or through a non-radiative process. In the radiative process, they emit light according to the energy difference of their excited and their equilibrium state. This emission spectrum is collected by a CCD sensor, and through the PL peaks important information for the electronic structure of the semiconductor can be deduced. PL measurements were performed at room temperature and at 20K, using a He-Cd laser (centered at 325 nm) for optical excitation. The emission spectra were collected by an Actron Research Spectrum PRP 500i spectrometer. The experimental accomplishment of the PL measurements was realized by Maria Androulidaki.

3.2.4 Atomic force microscopy

The atomic force microscopy (AFM) is a technique used for surface characterization of samples, through a thin probe attached to an atomic scale cantilever that scans the surface [2]. The position of the probe is managed through a feedback loop controller that takes as input the reflection of a laser beam that is directed on a mirror on top of the probe (Fig. 3.8). The sample drive allows for x-y-z movement through piezoelectric crystals (scanner). While the probe is scanning the surface, the deflection of the cantilever is measured through the laser beam reflection and is maintained constant by moving the scanner. The distance the scanner moves vertically at each (x,y) data point is recorded, and through proper software, the surface morphology is reconstructed.

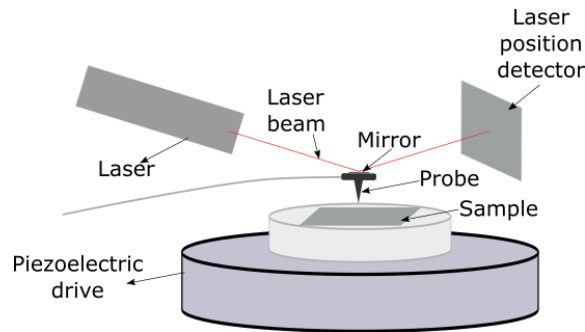


Figure 3.8: Schematics of the atomic force microscopy setup. The probe scans the surface of the sample, while its position is monitored by the reflection of a laser beam.

An AFM can operate in three different modes: (1) the non-contact mode, that means the probe does not come in contact with the surface of the sample, but is slightly higher, (2) the tapping mode, that means the probe oscillates and touches the surface at the lowest point of the oscillation, and (3) the contact mode, that means that the probe is in continuous contact with the surface. The AFM experiments on the samples grown were carried out by Katerina Tsagaraki and Dr. Jann Kruse.

3.2.5 X-ray diffraction

X-ray diffraction is a non-destructive method that is used for structural characterization and assessment for the crystal quality of samples [2, 17]. X-rays are produced through high energy electron collision with a metal, and then directed towards the sample. In the Bede D1 triple axis diffractometer that

was used, the source emitted a wavelength of $\lambda = 1.54056 \text{ \AA}$ (Cu K α 1), that is comparable with the dimensions of crystal lattices (i.e. $c_{GaN} = 5.185 \text{ \AA}$). The X-ray beam is passing through channel-cut crystal monochromators and definition slits and radiates to the sample, that is placed in a sample holder. Then, constructive interference occurs in specific incident angles according to Bragg's condition:

$$n\lambda = 2d\sin(\theta) \quad (3.4)$$

where n is a positive integer, λ is the wavelength of the X-ray, d is the plane spacing, and θ is the incident angle between the X-ray and the plane (Fig. 3.9).

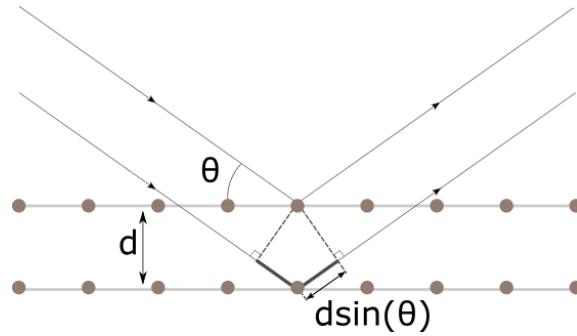


Figure 3.9: Representation of the Bragg's condition.

The sample holder can rotate in the x , y and z dimensions, controlling the angles of χ , ω and ϕ respectively. The detector can rotate around the sample in the dispersion plane, measuring the intensity of the diffracted beam at different 2θ angles (Fig. 3.10). Controlling the rotation of the sample around all 3 axes, in combination with the rotation of the detector, allows for a variety of different scan modes, the basic of which are [17] :

$\omega - 2\theta$: the sample and the detector are rotated by ω and 2θ , in a ratio of 1:2.

2θ : only the detector is rotated, tracing the diffracted beam in different 2θ angles.

ω -scan: rotation around the ω (y)-axis which is normal to the dispersion plane of the sample, changing the ω angle, without changing the position of the detector.

χ : rotation of the sample around the χ (x) axis, which is in the plane of the surface.

ϕ : rotation of the sample around the z -axis which is the normal to the surface, changing the ϕ angle.

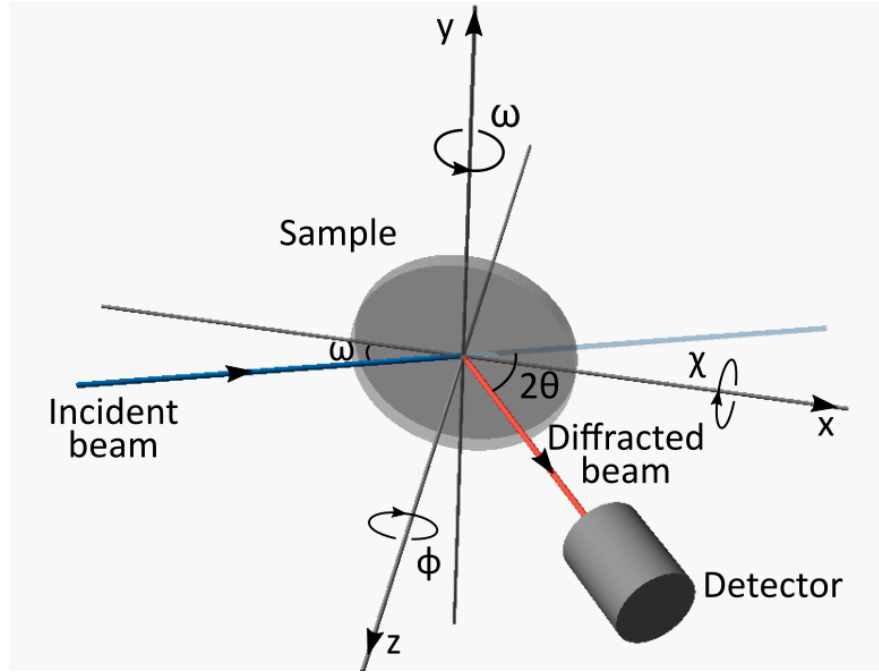


Figure 3.10: A schematic, showing the incident and reflected beams on the sample. The allowable rotations of the sample define the ω , ϕ and χ angles, and the position of the detector defines the 2θ angle.

XRD is widely used for the determination of lattice parameters (that provide information on composition and strain). It is also used to assess the misorientation of films (that gives information for defect types and densities) [17] and the thickness of different layers. In the case of nanowires (NWs), XRD measurements can provide valuable information on the alignment, the twist coherency, the growth direction and the epitaxial relation of the NWs with the substrate.

The $\omega - 2\theta$ scan is used to compare the alignment of the NWs. Comparison of the full width half maximum (FWHM) around planes that give constructive diffraction allows for an estimation of the alignment of each sample. In the case of well aligned NWs (Fig. 3.11.a), the FWHM is expected to be smaller than in the case of less aligned NWs (Fig. 3.11.b).

For the twist coherency of NWs with a wurtzite crystal, we take advantage of the six-fold symmetry around the [0001] direction that planes not parallel to the sample surface have, and search for 6 peaks in a $360^\circ \phi$ scan of specific planes (for the GaN crystal, the (11.4) planes were used). For NWs that have a high twist coherency, we expect sharp peaks, with smaller FWHM than those having a lower one.

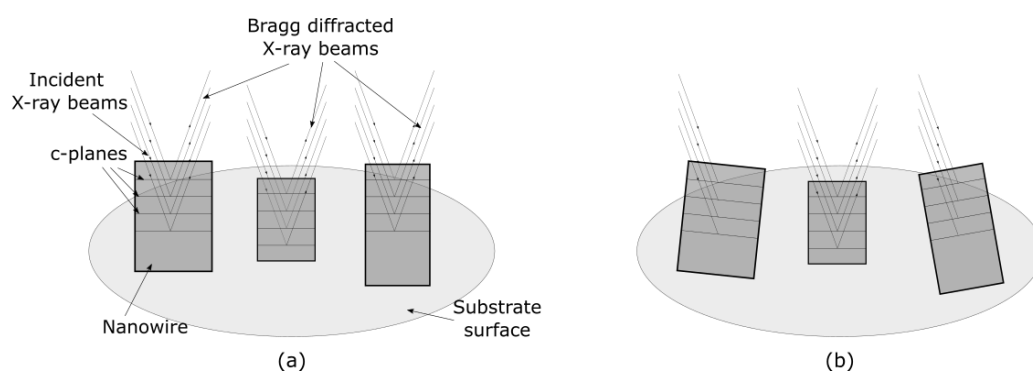


Figure 3.11: Schematic representation of Bragg reflection on well aligned (a) and less aligned (b) NWs. The Bragg diffracted X-ray beam has less intensity for a specific $\omega - 2\theta$ scan in the case of misaligned NWs.

Bibliography

- [1] BECHSTEDT, F. *"Principles of surface physics"*. Springer, 2003.
- [2] BRUNDLE, C. R., EVANS, C. A., AND WIHON, J. S., Eds. *"Encyclopedia of materials characterization - Surfaces, Interfaces, thin Films"*. Materials Characterization. Elsevier Inc., 1992.
- [3] DHANARAJ, G., BYRAPPA, K., PRASAD, V., AND DUDLEY", M., Eds. *"Springer handbook of crystal growth"*. Springer, 2010.
- [4] GEORGAKILAS, A., NG, H. M., AND KOMNINO, P. *"Nitride Semiconductors: Handbook on Materials and Devices"*. Wiley-VCH Verlag GmbH & Co. KGaA, 2016.
- [5] GOLDSTEIN, J. I., NEWBURY, D. E., MICHAEL, J. R., RITCHIE, N. W., SCOTT, J. H. J., AND JOY, D. C. *"Scanning Electron Microscopy and X-Ray Microanalysis"*, fourth edition ed. Springer, New York, NY, 2018.
- [6] HENINI, M., Ed. *"Molecular Beam Epitaxy - From research to mass production"*, 1 ed. Elsevier, Nov 2012.
- [7] HERMAN, M., AND SITTE, H. *"Molecular beam epitaxy, fundamentals and current status"*, 1 ed., vol. 7 of *Springer Series In Materials Science*. Springer-Verlag Berlin Heidelberg, 1989.
- [8] HOKE, W. E., LEMONIAS, P. J., AND WEIR, D. G. "Evaluation of a new plasma source for molecular beam epitaxial growth of InN and GaN films". *J. Cryst. Growth* (1991), 1024.
- [9] HUTTEL, Y., Ed. *"Gas-Phase Synthesis of Nanoparticle"*. Wiley-VCH Verlag GmbH & Co. KGaA, Weinheim, Germany, 2017.
- [10] IBACH, H., Ed. *"Physics of Surfaces and Interfaces"*. Springer Berlin Heidelberg New York, 2006.

- [11] ICHIMIYIA, A., AND COHEN, P. I. "*Reflection High Energy Electron Diffraction*". Cambridge University Press, 2004.
- [12] KNUDSEN, M. 'Molecular flow of gases through orifices (and effusion). English translation: AEC-tr-3715 (in German)'. *Ann. Phys.* 28 (1909), 999.
- [13] KNUDSEN, M. "The laws of molecular and viscous flow through tubes. English translation: AEC-tr-3303 (in German)". *Ann. Phys.* 28 (1909), 75.
- [14] KNUDSEN, M. "Die maximale Verdampfungsgeschwindigkeit des Quecksilbers". *Ann. Phys. (Leipzig)* 47 (1915), 697.
- [15] LANGMUIR, I. "The vapour pressure of metallic tungsten". *Phys. Rev.* 2 (1913), 239.
- [16] MATTHEWS, J. W., Ed. "*Epitaxial Growth*". Academic Press, Inc., 1975. Part B.
- [17] MORAM, M. A., AND VICKERS, M. E. "X-ray diffraction of Nitrides". *Rep. Prog. Phys.* (2009), 036502.
- [18] MOUSTAKAS, T. D. "*Gallium Nitride (GaN)*", 2 ed., vol. 57 of *Semiconductors and Semimetals*. Academic Press, Oct 1999.
- [19] TU, K.-N., MAYERS, J., AND FELDMAN, L. "*Electronic thin film science for electrical engineers and material scientists*". Macmillan publishing company, 2017.

Stages of spontaneous GaN NW growth

In this chapter we present existing knowledge on the nucleation and growth of GaN NWs on Si substrates. We begin by exploring three different cases of initial surfaces, when Si (111) substrates are used for GaN NW growth. We then describe the process of NW growth, that includes the nucleation and elongation stages.

4.1 The initial surface

When active N and Ga adatoms reach the Si (111) substrates, an amorphous Si_xN_y layer unavoidably forms, simultaneously with the GaN crystal. This process results in a not-well defined interface between GaN and the nitridated Si surface, that also affects the grown NWs [4, 5, 14, 17]. Two common procedures are used in order to have a better defined interface between the GaN NWs and the Si (111) substrate. These are exposure of the initial surface to active N, and deposition of a thin AlN layer. More details concerning the interface, and the effects on the GaN NWs in each of the above cases, will be presented in chapters 6 and 7 respectively.

In this section, we focus on the three different initial surfaces for GaN NW growth mentioned above (bare Si (111), amorphous Si_xN_y and AlN layer) and comment on the RHEED patterns observed throughout our experiments.

First the pattern in the case of a bare Si (111) surface for an electron beam incident along the $\langle 0\bar{1}1 \rangle$ Si azimuth is shown in Fig. 1.1.a. The streaks that are visible are representative of the 7×7 Si reconstruction, that occurs on a clean Si (111) surface. This pattern is usually observed at high temperatures, between $600\text{-}860^\circ\text{C}$ [20, 25, 27]. When the Si (111) wafer cleaning procedure described in appendix A was followed, the 7×7 pattern appeared systematically between $740\text{-}760^\circ\text{C}$ (manipulator's thermocouple temperature) during

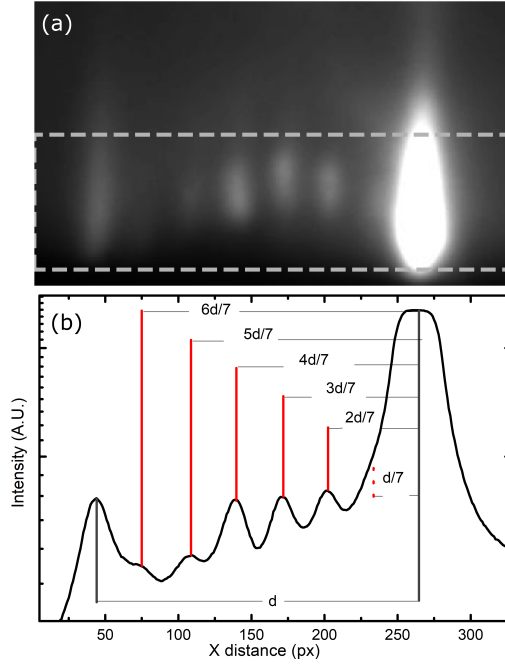


Figure 4.1: (a) RHEED pattern for electron beam incident along the $\langle 0\bar{1}1 \rangle_{Si}$. A $x7$ Si (111) surface reconstruction is visible, that corresponds to the 7×7 Si (111) surface reconstruction. (b) Pixel intensity averaged over the height of the image in (a) within the gray dashed border, as a function of the x-distance in (a). The distance between the streaks visible is $1/7$ of the distance between the two main Si (111) streaks.

the Si substrate heating. The axes of the characteristic surface cell of the 7×7 reconstruction are 7 times larger than the bulk Si (111) surface basic cell [26] in both the $\langle 0\bar{1}1 \rangle$ and $\langle \bar{2}11 \rangle$ directions.

This is verified by the distances between the visible streaks: compared to the distance between the 0th and 1st order reflection of the bulk the $x1$ Si (111) streaks, d , the distance between two successive streaks in the $x7$ pattern is $d/7$. This is better illustrated in Fig. 1.1.b. The distance between two neighbouring Si surface atoms, towards the $\langle 0\bar{1}1 \rangle$ and $\langle \bar{2}11 \rangle$ directions is 3.84 \AA and 6.65 \AA length (Si-Si bond length is 2.35 \AA), while for the case of the 7×7 reconstruction, the dimensions of the characteristic surface basic cell are 26.88 \AA and 46.55 \AA , respectively.

Second, we show the observed RHEED for the amorphous Si_xN_y layer in Fig. 1.2. As expected from an amorphous surface, the observed RHEED is diffuse and featureless. The RHEED pattern of the third type of surface, that of an AlN crystalline film, is shown in Fig. 1.3. The electron beam was

incident along the $\langle 10\bar{1}0 \rangle$ AlN direction. A detailed study observing the modification of the Si (111) 7×7 reconstruction to the bulk 1×1 periodicity of the AlN (0001) surface will be presented in chapter 7.

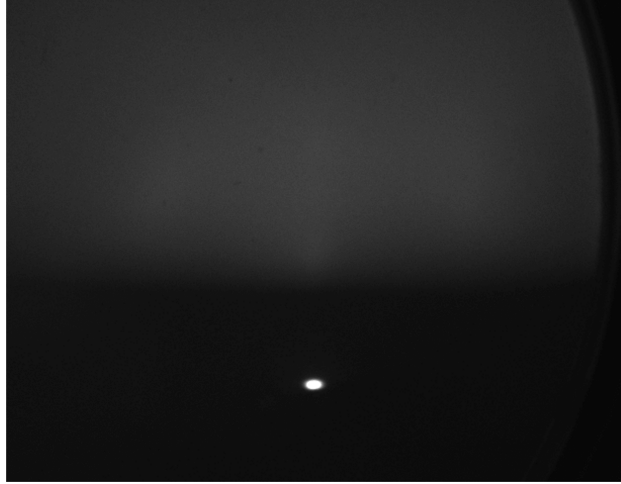


Figure 4.2: The diffuse RHEED that is visible after the nitridation of the Si (111) surface, and the formation of an amorphous Si_xN_y .

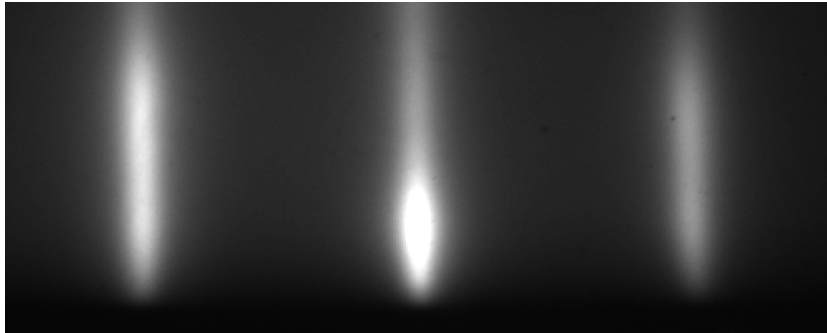


Figure 4.3: The $x1$ RHEED diffraction pattern for an incident electron beam along the $\langle 10\bar{1}0 \rangle$ AlN direction. This is characteristic of the 1×1 AlN surface.

4.2 GaN nanowire nucleation

The nucleation stage of the NWs begins when active N and Ga atoms reach the initial surface. Initially, there is a period where most of the deposited Ga atoms are desorbed back into the vacuum [5, 15]. During this period,

almost no GaN nucleation events occur. When a 7×7 Si (111) reconstructed surface is used as an initial surface (Fig. 1.1), the RHEED pattern initially changes from the 7×7 RHEED pattern to diffuse light, corresponding to the amorphous Si_xN_y formation. On the other hand, when active N and Ga atoms are deposited on an amorphous Si_xN_y surface (Fig. 1.2) and on a thin AlN layer (Fig. 1.3), no change is observed on the initial RHEED pattern during the first minutes.

The appearance of GaN transmission spots in the RHEED pattern signals the beginning of 3D GaN island nucleation [6, 19, 22]. Fig. 1.4 shows the RHEED pattern in the case of GaN nucleating on top of a 1.5 nm of crystalline AlN. We can clearly distinguish the AlN streaks, on top of which the transmission spots appear.

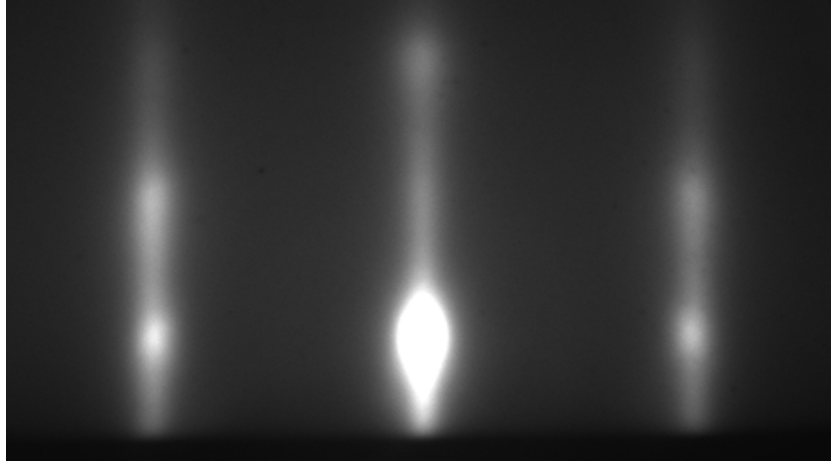


Figure 4.4: The $x1$ RHEED diffraction pattern, for an electron beam incident along the $\langle 10\bar{1}0 \rangle$ AlN direction, of the 1×1 AlN surface, with the faint appearance of 3D GaN island spots.

The time needed for the majority¹ of the GaN NWs to nucleate is referred to as the incubation time [11]. The incubation time, τ_{inc} , depends on temperature according to the Arrhenius law $\tau_{inc} \propto \exp(-\Delta E_{inc}/k_B T)$ [13], where ΔE_{inc} is the activation energy.

As the deposition of N and Ga atoms continues, some GaN nuclei that survive grow larger in size, until they grow to a stable size, forming a GaN island. Then the islands follow a series of shape transformations, that depend on the epitaxial constraints that are enforced from the substrate [8, 9]. The final shape is a 3D hexagonal-prism column, which is the shape of the NW.

¹GaN NWs can be nucleated throughout the growth procedure, in different regions of free surface of the substrate.

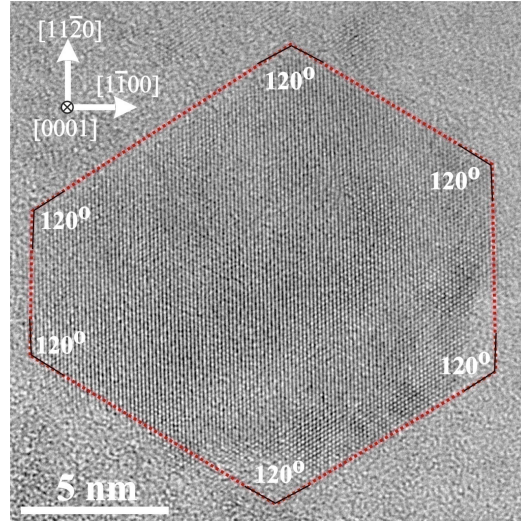


Figure 4.5: Plan-view HRTEM image of a GaN NW base. The hexagonal (red dotted shape) morphology of the GaN NW, with 10-10 side facets (*m*-planes) is evident.

The main axis of the formed NWs is parallel to the $[0001]$ direction (*c*-axis), as confirmed by XRD measurements we performed (Fig. 1.6). The six side facets are $\{1\bar{1}00\}$ surfaces (*m*-planes), as verified by HRTEM measurements (Fig. 1.5), and as AFM, SEM and HRTEM studies have shown [1, 7].

It should be noted at this point, that due to the statistical nature of the processes occurring during MBE growth, nucleation events can occur throughout the growth process. The above description concerns the majority of the NW nucleation events, that occur in the initial stages of the growth.

4.3 Evolution of the formed GaN NWs

Once the NWs have formed, they grow larger as time progresses, with a larger axial growth rate compared to the radial one. As the GaN NWs grow higher, the electron beam of the RHEED is blocked from reaching the bottom surface. As a result, in the case where an AlN prelayer on Si is used, the AlN streaks gradually disappear, and the GaN diffraction spots become brighter and smaller (Fig. 1.7).

The NW growth rate along the $[0001]$ axis is larger than that of a GaN (0001) film grown in the Ga-limited (N-rich) growth regime with the same Ga-flux, but smaller than the thickness of a GaN film that would be grown, respectively, in the N-limited (Ga-rich) growth regime. These characteris-

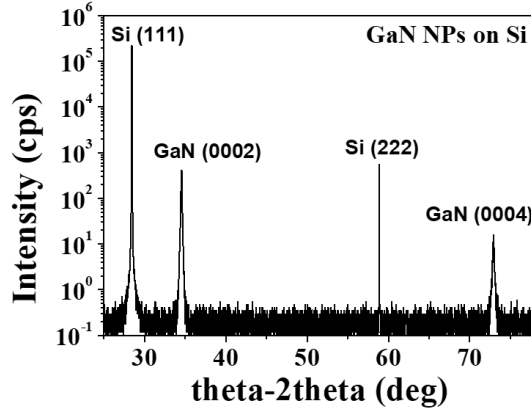


Figure 4.6: Theta-2theta XRD measurements, showing that the orientation relationship between the GaN NWs and the Si substrate is $(0002)_{\text{GaN}} // (111)_{\text{Si}}$

tics reveal that the NW elongation process is governed by diffusion-induced process [12, 21, 24], during which Ga adatoms diffuse from the substrate surface and the side facets of the NW towards the top (0001) surface of the NW. Due to a faster nucleation at the top c-plane compared to the side m-planes, the top surface acts as a sink for the Ga adatoms [24], as illustrated in Fig. 1.8.

The preferred nucleation on the top c-plane could be a result of the smaller nucleation barrier for GaN nucleation on the c-plane compared to that of m-plane facets [7]. An additional process that could aid in the preferential axial growth, was proposed by Lymperakis et al [23]. Using density functional theory calculations, they found that the non-polar m-plane is unstable when interacting with atomic nitrogen. Atomic nitrogen could be present in the nitrogen RF plasma beam and would result in a lower GaN nucleation rate on the m-plane than on the polar c-plane.

Additionally to the above, the geometrical factors of the PA-MBE also contribute to the higher axial growth rate compared to the radial one, as shown in the work of Foxon et al [16]. When considering the inclination of the Ga beam and of the nitrogen plasma source compared to the NW axial direction, they calculated a much higher arrival rate at the top surface of the NW compared to the side facets (factor of 5 difference). In our MBE system, the Ga source has a $\sim 20^\circ$ angle compared to the direction normal to the surface, and could result to a growth rate ratio (axial growth / radial growth) of ~ 8 , if all the incident atoms were incorporated in the solid without any surface diffusion.

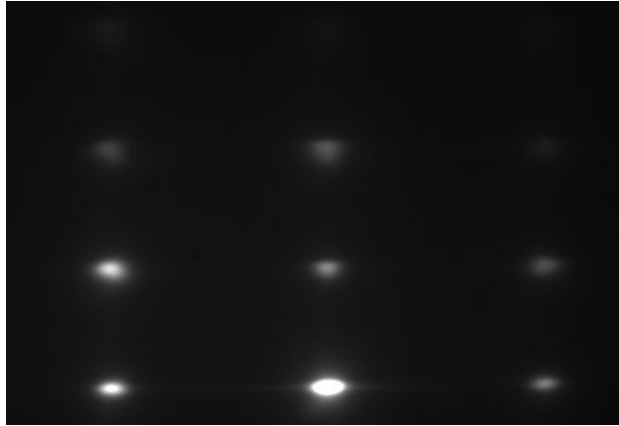


Figure 4.7: The characteristic spotty RHEED diffraction pattern observed for an electron beam incident along the $\langle 10\bar{1}0 \rangle$ GaN direction, when GaN NWs are fully formed and grown as described in the text.

The growth of the NWs is governed by the diffusion process of Ga adatoms. Thus, the number of Ga adatoms reaching the top surface is limited by the diffusion length. In the case of NWs with heights much larger than the Ga diffusion length on the side-facets, the contribution of Ga adatoms from the substrate surface should be almost zero [7]. The diffusion length on the side-facet has been estimated to be less than 100 nm [6, 12, 18, 23].

4.4 Evolution of NWs in our MBE system

In order to identify the characteristics of the evolution of GaN NWs in our MBE system, we performed a time-series analysis. We prepared samples with different durations of GaN growth on Si (111) substrates. Preparation of the Si (111) wafers is described in Appendix A. A 1.5 nm thick AlN film was then deposited on the initial Si surface, followed by 20 min of exposure to active nitrogen. Then, GaN NWs were grown for 20 min, 40 min, 60 min, 180 min and 330 min, with identical growth conditions (Fluxes of Ga and N equivalent to $F_{Ga} = 84.6$ nm/h, $F_N = 430$ nm/h, $T_{Gr} = 760^\circ\text{C}$).

Fig. 1.9 shows cross-section, tilted and top-view SEM images of these samples, in the top, middle and bottom rows of Fig. 1.9 respectively. As the growth duration increases (from left to right) the height, h , of the NWs also increases, as observed from the cross-section images. Similarly, an increase in the diameter, d , is also observed from the tilted view SEM images. From the side-by-side comparison of the top view SEM images, in Fig. 1.9, we can see a steep increase of the NW density for a duration up to 40 min, followed

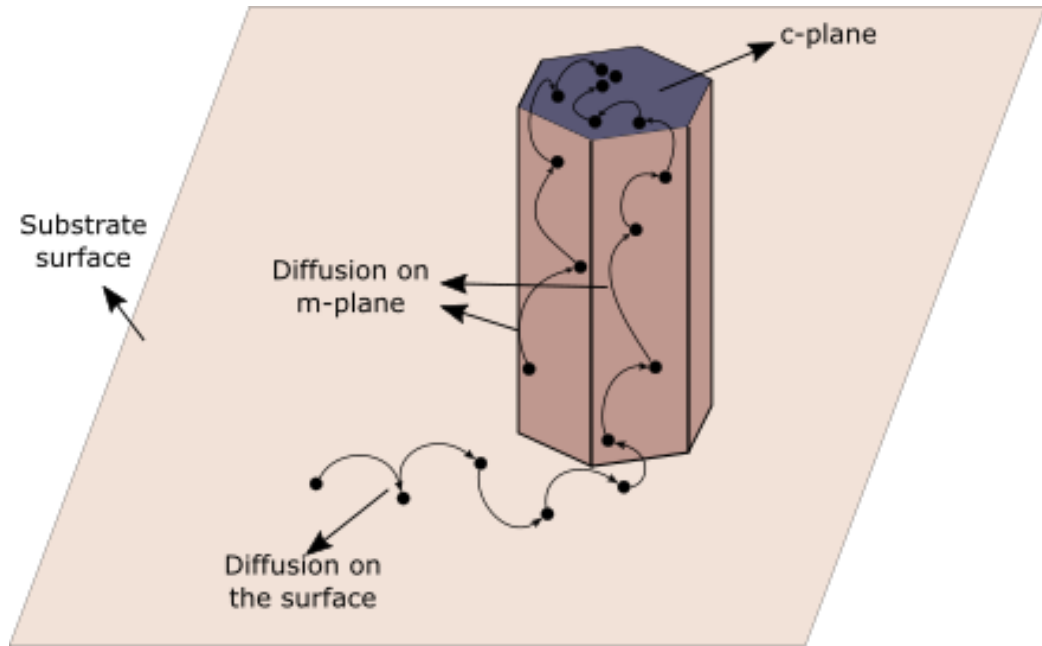


Figure 4.8: Diffusion of adatoms on the surface and on the side facets of a NW. Diffusion drives the adatoms towards the top facet of the NW, the c-plane facet, that acts as a sink.

by a decrease for longer growths. We quantify these trends in the following analysis.

Fig. 1.10 shows the experimentally determined average NW height as a function of time. Additionally, we compare this height to its expected values if it was limited by the incident flux of Ga (red triangles) or by the incident N-flux (blue squares). The actual height of the NWs in all the growth times studied, is larger than the Ga-limited NW height, and smaller than the N-limited NW height.

The increase of the average height with time appears to be linear, suggesting that GaN NWs grow almost with a constant growth rate. This was calculated to be 255 nm/min. For the calculation of the average growth rate, the sample with NWs shorter than 150 nm was not included in order to avoid significant contribution of Ga adatoms diffusing from the substrate-surface in the growth rate (adatom diffusion length along m-planes is calculated to be less than 100 nm). The growth rate of 255 nm/h is larger than Ga-limited growth rate (84.6 nm/h) and smaller than N-limited one (430 nm/h). It suggests a significant diffusion of Ga adatoms (4 times the directly incident flux on the (0001) plane) from the lateral m-sided to the top c-plane surface

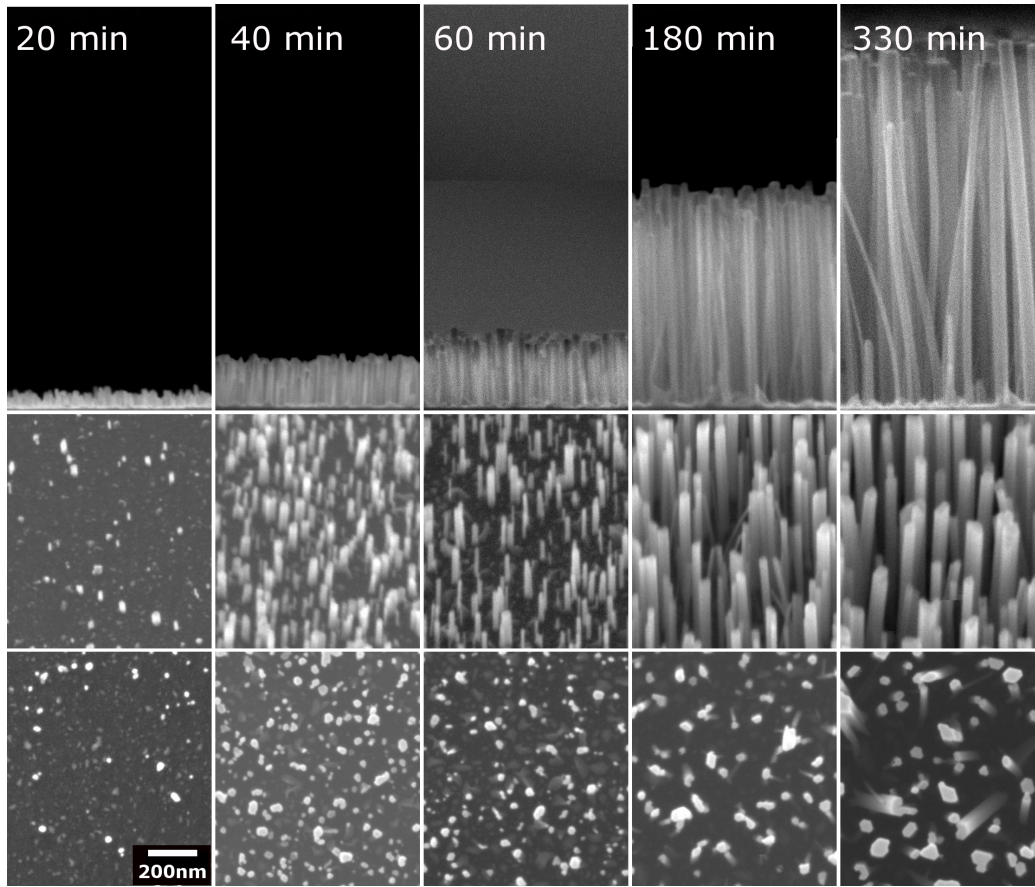


Figure 4.9: Cross-section (top row), tilted (middle row) and top view (third row) SEM micrographs of NW samples grown for 20 min, 40 min, 60 min, 180 min and 330 min, in identical growth conditions ($F_{Ga} = 84.6 \text{ nm/h}$, $F_N = 430 \text{ nm/h}$, $T_{Gr} = 760^\circ \text{C}$). The scale bar is 200 nm for all micrographs.

Fig. 1.11, shows the average diameter (d) of the NWs as a function of the growth time. A linear trend provides a good fit to the data, within the range of explored values. The calculated diametric growth rate was found to be 7.46 nm/h , less than 3% of the axial growth rate. This is in agreement with the expectations discussed in section 1.3, and comparable with the 10.2 nm/h found in the work of Furtmayr et al [17]. It should be noted that throughout the literature, the diametric growth rate is also referred to as radial growth rate. However, for comparison between nucleation rates of the m-plane and c-plane, one should compare the radial growth rate ($\Delta r/t_{gr} = \Delta d/(2t_{gr})$) with the axial one ($\Delta h/t_{gr}$), and not the diametric growth rate. As we can see from our results, GaN nucleation at the m-plane of the NWs occurs with a rate less than 1.5 % of that at the c-plane.

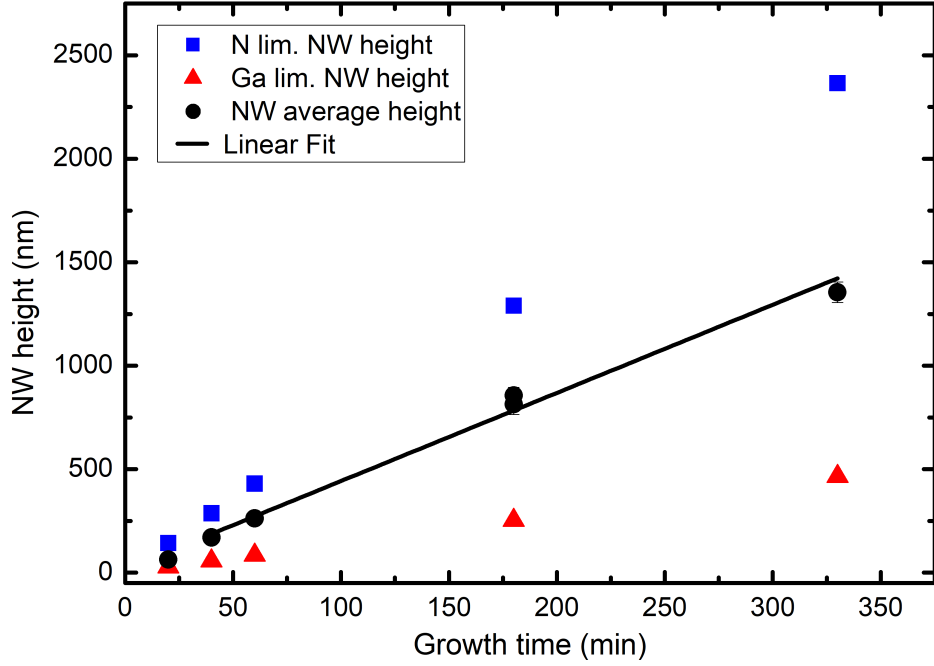


Figure 4.10: Average height, h , of the GaN nanowires (black circles), grown for different time duration (20, 40, 60, 180 and 330 min), in identical growth conditions ($F_{Ga} = 84.6 \text{ nm/h}$, $F_N = 430 \text{ nm/h}$, $T_{Gr} = 760^\circ \text{C}$). The expected NW height if it was Ga-limited and N-limited are also shown by red triangles and blue squares, respectively.

The NW density as a function of time is shown in fig. 1.12. The number density reaches up to $22.5 \times 10^9 \text{ cm}^{-2}$, for $t_{Gr} = 40 \text{ min}$. Then it follows an exponential-like reduction down to $6.5 \times 10^9 \text{ cm}^{-2}$, for $t_{Gr} = 330 \text{ min}$. A similar behaviour of a maximum in the number density in the first growth minutes has been also observed by Calarco et al [3]. This has been attributed to the coalescence of the NWs that form closely to each other, as the NWs grow larger in size with time [3, 12]. Additionally, at longer growth durations, coalescence of NWs also occurs due to another factor. NWs that have acquired substantial height may coalesce due either to electric forces from electric build-up charges, that can be caused either by an electron beam (during RHEED observations, or when evaluating the sample in the SEM microscope) [2] or due to the nitrogen plasma [28], or due to a negligible tilt of the NW due to defects and morphological irregularities at the interface [10].

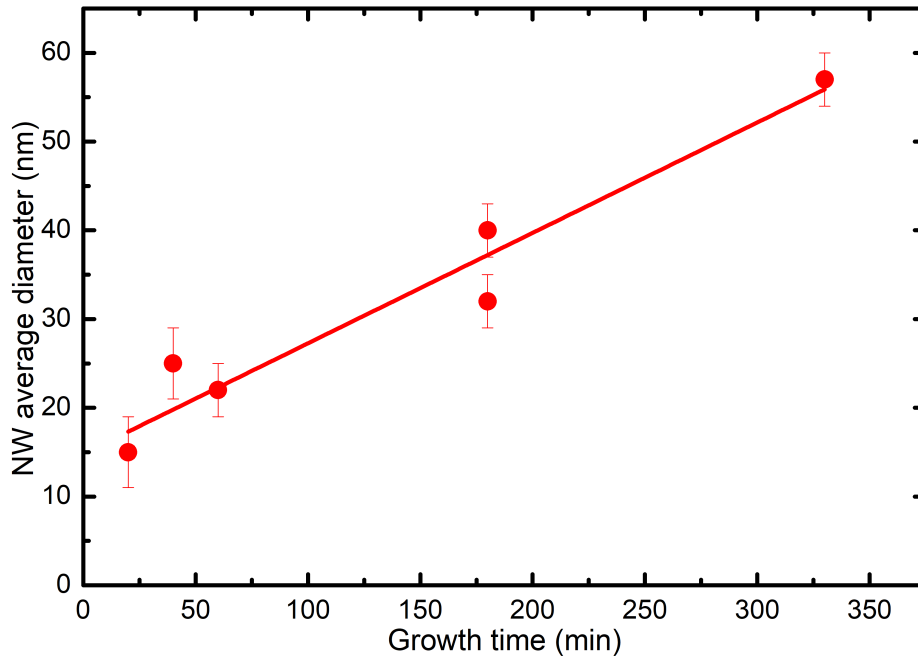


Figure 4.11: Average diameter of GaN nanowires, grown for different durations ($t_{Gr} = 20, 40, 60, 180$ and 330 min) in identical growth conditions ($F_{Ga} = 84.6$ nm/h, $F_N = 430$ nm/h, $T_{Gr} = 760^\circ$ C). The line is a linear fit to the data, giving an average diametric growth rate of 7.46 nm/h.

4.5 Conclusions

Throughout this chapter, we present the basics of the GaN NW growth on Si (111) substrates. The NWs form through a two step stage, the nucleation and elongation stage. During the two step process, an incubation stage precedes any formation of a stable GaN nuclei. The nuclei will evolve into a NW through a series of shape transformations, that depends on the initial surface, and then through a diffusion induced process the GaN NW height and diameter will increase. We showed the linearity of the height and radius with time, for GaN NWs grown in our MBE system.

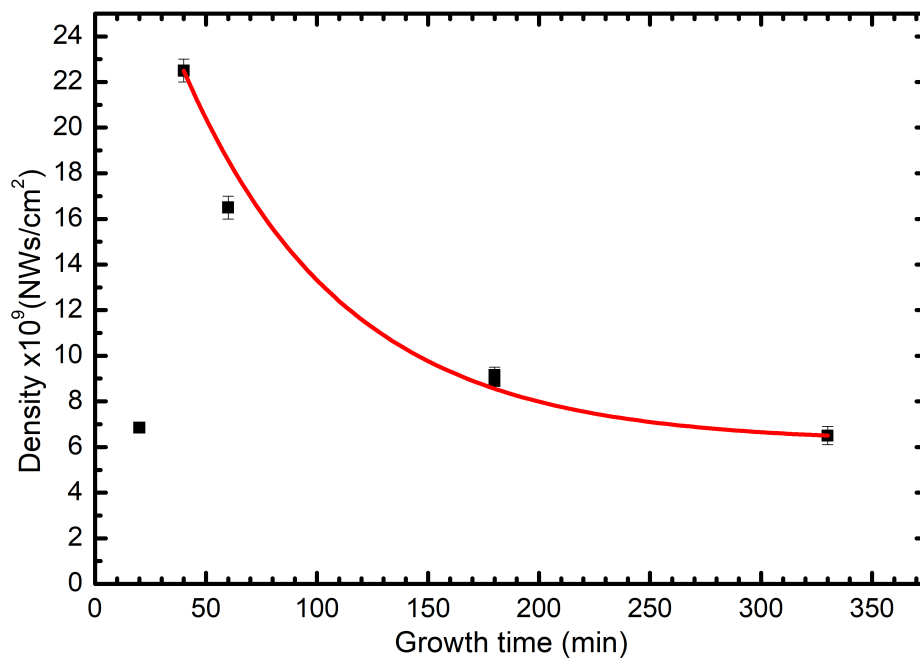


Figure 4.12: Density of GaN nanowires, grown for different time duration (20, 40, 60, 180 and 330 min), for identical growth conditions as described in the text. During the first minutes there is a steep increase, that is followed by an exponential-like decrease.

Bibliography

- [1] BERTNESS, K. A., ROSHKO, A., MANSFIELD, L., HARVEY, T., AND SANFORD, N. "Nucleation conditions for catalyst-free GaN nanowires". *J. Cryst. Gr.* 300 (2007), 94.
- [2] BERTNESS, K. A., ROSHKO, A., SANFORD, N. A., BARKER, J. M., AND DARYDOV, A. V. "Spontaneously grown GaN and AlGaN nanowires". *J. Cryst. Gr.* 7287 (2006), 522.
- [3] CALARCO, R., MEIJERS, R. J., DEBNATH, R. K., STOICA, T., SUTTER, E., AND LUTH, H. "Nucleation and Growth of GaN Nanowires on Si(111) Performed by Molecular Beam Epitaxy". *Nano Lett.* 7, 8 (2007), 2248.
- [4] CALLEJA, E., RISTIC, J., FERNANDEZ-GARRIDO, S., AND M. A. SANCHEZ-GARCIA, L. C., GRANDAL, J., TRAMPERT, A., JAHN, U., SANCHEZ, G., GRIOL, A., AND B.SANCHEZ. "Growth, morphology, and structural properties of group-III-nitride nanocolumns and nanodisks". *Phys. Stat. Solidi (b)* 244 (2007), 2816.
- [5] CHEZE, C., GEELHAAR, L., TRAMPERT, A., AND RIECHERT, H. "In situ investigation of self-induced GaN nanowire nucleation on Si". *Appl. Phys. Lett.* 97 (2010), 043101.
- [6] CONSONNI, V. "Self-induced growth of GaN nanowires by molecular beam epitaxy: A critical review of the formation mechanisms". *Phys. Status Solidi RRL* 7, 10 (2013), 699.
- [7] CONSONNI, V., DUBROVSKII, V. G., TRAMPERT, A., GEELHAAR, L., AND RIECHERT, H. "Quantitative description for the growth rate of self-induced GaN nanowires". *Phys. Rev. B* 85 (2012), 155313.
- [8] CONSONNI, V., HANKE, M., KNELANGEN, M., GEELHAAR, L., TRAMPERT, A., AND RIECHERT, H. "Nucleation mechanisms of self-

- induced GaN nanowires grown on an amorphous interlayer". *Phys. Rev. B* *83* (2011), 035310.
- [9] CONSONNI, V., KNELANGEN, M., GEELHAAR, L., TRAMPERT, A., AND RIECHERT, H. "Nucleation mechanisms of epitaxial GaN nanowires: Origin of their self-induced formation and initial radii". *Phys. Rev. B* *81* (2010), 085310.
- [10] CONSONNI, V., KNELANGEN, M., JAHN, U., TRAMPERT, A., GEELHAAR, L., AND RIECHERT, H. "Effects of nanowire coalescence on their structural and optical properties on a local scale". *Appl. Phys. Lett.* *95* (2009), 241910.
- [11] CONSONNI, V., TRAMPERT, A., GEELHAAR, L., AND RIECHERT, H. "Physical origin of the incubation time of self-induced GaN nanowires". *Appl. Phys. Lett.* *99* (Jul 2011), 033102.
- [12] DEBNATH, R. K., R, M., RICHTER, T., STOICA, T., CALARCO, R., AND LUTH, H. "Mechanism of molecular beam epitaxy growth of GaN nanowires". *Appl. Phys. Lett.* *90* (2007), 123117.
- [13] DUBROVSKII, V. G. "Incubation Time of Heterogeneous Growth of Islands in the Mode of Incomplete Condensation". *Tech. Phys. Lett.* *42* (2016), 1103.
- [14] EFTYCHIS, S., J.KRUSE, T.KOUKOULA, TH.KEHAGIAS, PH.KOMNINOU, A.ADIKIMENAKIS, TSAGARAKI, K., M.ANDROULIDAKI, P.TZANETAKIS, E.ILIOPOULOS, AND A.GEORGAKILAS. "Understanding the effects of Si(111) nitridation on the spontaneous growth and properties of GaN nanowires". *J. Cryst. Gr.* *442* (2016), 8.
- [15] FERNANDEZ-GARRIDO, S., GEELHAAR, J. K. Z. L., AND BRANDT, O. "Monitoring the Formation of Nanowires by Line-of-Sight Quadrupole Mass Spectrometry: A Comprehensive Description of the Temporal Evolution of GaN Nanowire Ensembles". *Nano Lett.* *15* (2015), 1930.
- [16] FOXON, C. T., NOVIKOV, S., HALL, J. L., CAMPION, R. P., CHERNS, D., GRIFFITHS, I., AND KHONGPHETSAK, S. "A complementary geometric model for the growth of GaN nanocolumns prepared by plasma-assisted molecular beam epitaxy". *J. Cryst. Gr.* *311* (2009), 3423.

- [17] FURTMAYR, F., VIELEMEYER, M., STUTZMANN, M., ARBIOL, J., ESTRADE, S., PEIRO, F., MORANTE, J. R., AND EICKHOFF, M. "Nucleation and growth of GaN nanorods on Si (111) surfaces by plasma-assisted molecular beam epitaxy - The influence of Si- and Mg-doping". *Appl. Phys. Lett.* 104 (2008), 034309.
- [18] GALOPIN, E., L, L., PATRIARCHE, G., TRAVERS, L., GLAS, F., AND HARMAND, J. C. "Morphology of self-catalyzed GaN nanowires and chronology of their formation by molecular beam epitaxy". *Nanotechnology* 22 (2011), 245606.
- [19] HESTROFFER, K., AND DAUDIN, B. "A RHEED investigation of self-assembled GaN nanowire nucleation dynamics on bare Si and on Si covered with a thin AlN buffer layer". *Phys. Status Solidi RRL* 7 (2013), 835.
- [20] HU, C.-W., HIBINO, H., OGINO, T., AND TSONG, I. S. T. "Hysteresis in the (1x1)-(7x7) first-order phase transition on the Si (111) surface.". *Surface Science* 487 (2001), 191.
- [21] JOHANSSON, J., SCENSSON, C. P. T., MARTENSSON, T., SAMUELSON, L., AND SEIFERT, W. "Transport Model for Semiconductor Nanowire Growth". *J. Phys. Chem. B* 109 (2005), 13567.
- [22] KNELANGEN, M., CONSONNI, V., TRAMPERT, A., AND RIECHERT, H. "In situ analysis of strain relaxation during catalyst-free nucleation and growth of GaN nanowires". *Nanotechnology* 21 (2010), 245705.
- [23] LYMPERAKIS, L., AND NEUGEBAUER, J. "Large anisotropic adatom kinetics on nonpolar GaN surfaces: Consequences for surface morphologies and nanowire growth". *Phys. Rev. B* 79 (2009), 241308(R).
- [24] RISTIC, J., CALLEJA, E., FERNANDEZ-GARRIDO, S., CERUTTI, L., TRAMPERT, A., JAHN, U., AND PLOOG, K. H. "On the mechanisms of spontaneous growth of III-nitride nanocolumns by plasma-assisted molecular beam epitaxy". *J. Cryst. Gr.* 310 (2008), 4035.
- [25] SUZUKI, T., AND HIRABAYASHI, Y. "First Observation of the Si (111)-7x7-1x1 Phas Transition by the Optical Second Harmonic Generation". *Jpn. J. Appl. Phys.* 32 (1993), L610.
- [26] TAKAYANAGI, K., TANISHIRO, Y., TAKAHASHI, M., AND TAKAHASHI, S. "Structural analysis of the Si(111)-7x7 by UHV-transmission

- electron diffraction microscopy". *Journal of Vacuum Science & Technology A* 162 (1985), 163.
- [27] TELIEPS, W., AND BAUER, E. "The (7x7)-(1x1) phase transition on Si (111)". *Surface Science* 162 (1985), 163.
- [28] ZETTLER, J. K., CORFDIR, P., GEELHAAR, L., RIECHERT, H., BRANDT, O., AND FERNNDEZ-GARRIDO, S. "Improved control over spontaneously formed GaN nanowires in molecular beam epitaxy using a two-step growth process". *Nanotechnology* 26 (2015), 445604.

The role of substrate temperature in spontaneous GaN nanowire growth

As we have seen in the previous chapter, the kinetic processes occurring on the initial substrate surface, and on the side facets of a formed NW are crucial for the NW nucleation and in the elongations process. These processes are defined by the minority atoms (Ga adatoms) that are present. The behaviour of the adatoms (i.e., density and diffusion length) strongly depends on the temperature of the surface on which the adatoms are diffused throughout the NW nucleation and elongation stages. The temperature should be low enough to minimize Ga adatom desorption, and high enough to enable adatom diffusion during the NW nucleation and elongation stages.

The complicated effect of substrate temperature on the Ga adatom kinetics is reflected on the final GaN NW characteristics. The NW density, height and diameter strongly depend on the temperature used [2, 10]. Although this has been extensively studied for the case of GaN NWs grown on bare Si (111) substrates [2, 5, 10], the case of GaN NWs grown with the use of a thin AlN prelayer on top of the Si substrates is not well documented. In this chapter we aim to address this, and find which characteristics, and in which range, are affected.

In order to study the substrate temperature effects on the nucleation stage, we grew a series of samples at different temperatures. The substrate temperature for every sample was kept constant throughout the growth. Since this affected mainly the nucleation stage, as we will see in detail in the following, the effects on the elongation stage could not be clearly identified. For that reason, two more series of samples were grown, following a two-step growth process (two different substrate temperatures during the growth). The substrate temperatures and growth times for all samples are shown in Table 5.1.

Table 5.1: A short description of the samples used to study the effects of the substrate temperature. All the samples included in the table were grown on bare Si (111) wafers, with the use of 1.5 nm AlN prelayer. The Ga and N fluxes corresponded to GaN equivalent growth rates of 84.6 nm/h and 430 nm/h.

	Growth T_{sub} ($^{\circ}$ C)		Growth duration (min)		Sample Name
One Step Gr.	760		180		OS760 ¹
One Step Gr.	780		180		OS780
One Step Gr.	790		180		OS790
One Step Gr.	800		180		OS800
One Step Gr.	730		20		OS730
	IGS T ($^{\circ}$ C)	FGS T ($^{\circ}$ C)	IGS duration (min)	FGS duration (min)	Sample No
Two Step Gr.	730	750	20	160	TS750-160
Two Step Gr.	730	760	20	160	TS760-160
Two Step Gr.	730	770	20	160	TS770-160
Two Step Gr.	730	780	20	160	TS790-160
Two Step Gr.	730	790	20	160	TS790-160
Two Step Gr.	730	800	20	160	TS800-160
Two Step Gr.	730	780	3	177	TS730-3
Two Step Gr.	730	780	6	174	TS730-6

5.1 One-step growth

Samples were grown at four different substrate temperatures (kept constant throughout the process), namely $T_{sub} = 760$ $^{\circ}$ C, 780 $^{\circ}$ C, 790 $^{\circ}$ C and 800 $^{\circ}$ C. Fig. 5.1 shows cross-section (first row), tilted-view (middle row) and top-view (bottom row) SEM micrographs of these samples. By inspecting the figure, two main trends are apparent. First, the NW number density decreases significantly with substrate temperature. This is particularly prominent at the highest T_{sub} of 800 $^{\circ}$ C studied. In the SEM images taken for this sample, only three NWs are present. Second, the height of the NWs decreases with increasing T_{sub} .

We study these trends quantitatively in Fig. 5.2. In the plot of Fig. 5.2(a), we see that the average NW height changes from ~ 850 nm for GaN NWs grown at $T_{sub} = 760$ $^{\circ}$ C, down to 95 nm for $T_{sub} = 800$ $^{\circ}$ C. Additionally to the average NW height, a significant decrease is also observed in the minimum and maximum height values that were recorded.

The plot of Fig. 5.2(b) shows how the NW density changes with substrate temperature. For the lowest temperatures of 760 $^{\circ}$ C and 780 $^{\circ}$ C, the density does not change significantly (1×10^9 cm^{-2} and 1.2×10^9 cm^{-2} respectively). However, for the higher temperatures of 790 $^{\circ}$ C and 800 $^{\circ}$ C the density is drastically reduced by more than two orders of magnitude (down to $\sim 1 \times 10^7$

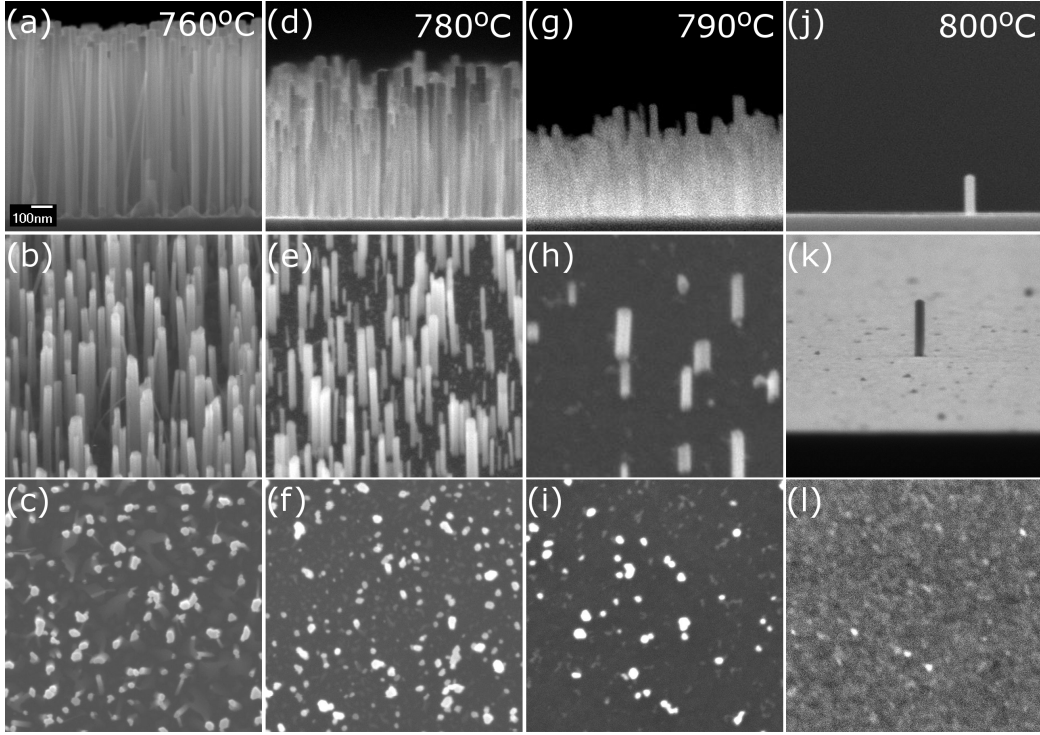


Figure 5.1: One-step growth NW samples. Cross-section (top row), tilted (middle row) and top view (third row) SEM micrographs of samples grown at $760\text{ }^{\circ}\text{C}$ (a, b and c), $780\text{ }^{\circ}\text{C}$ (d, e and f), $790\text{ }^{\circ}\text{C}$ (g, h and i) and $800\text{ }^{\circ}\text{C}$ (j, k and l). The Ga- and N- fluxes used were 84.6 nm/h and 430 nm/h respectively, and the total GaN deposition time was 3 h.

cm^{-2}). This reduction reflects the exponential dependence of the island nucleation rate on the inverse substrate temperature. While at $T_{sub} = 800\text{ }^{\circ}\text{C}$, the GaN island nucleation is almost eliminated (fig. 5.1), the presence of even a few NWs that were visible in the SEM micrographs (Fig. 5.1(j), (k) and (l)) suggests that once the initial GaN NW forms, the elongation of the NW proceeds, even at $T_{sub} = 800\text{ }^{\circ}\text{C}$. The reduction of NW density at high temperatures was also observed by Consonni et al [5]. In section 5.2 we will show that a two-step growth process with a low-T initial growth stage, can restore the density for higher values of substrate temperature.

Interestingly, for substrate temperatures higher than $780\text{ }^{\circ}\text{C}$, the measured average diameter increases with increasing temperature. This is shown in Fig. 5.3.a. This increase that was also observed in other studies [10] could be related to an increase in the stable nucleus size at higher temperatures [8].

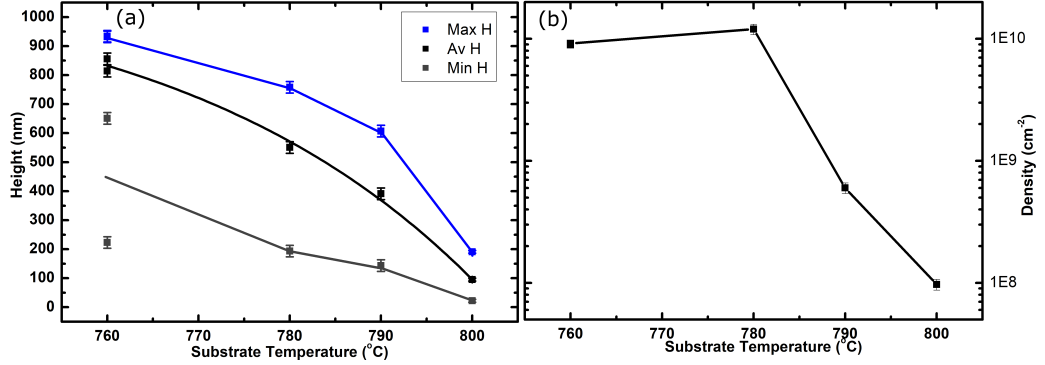


Figure 5.2: Graphs showing the relation of (a) height and (b) density as a function of temperature. The measurements were made for samples with GaN NWs grown at different T_{sub} (760°C, 780°C, 790°C and 800°C), from SEM micrographs. For the case of $T_{sub} = 760^\circ\text{C}$, two samples were grown and illustrated in the graphs.

During the growth of the samples, RHEED observations allowed us to estimate the incubation time τ of the GaN NWs (i.e. duration until the first Ga spots started appearing). Fig. 5.3.b shows how τ changes as a function of temperature. Two additional samples grown at lower substrate temperatures (730°C and 745 °C) are included, to increase the temperature range. These samples were grown for the first 20 min in the same growth conditions as the rest that are used in this series, but later their temperature was changed, as part of the two-step series that will be analysed in the following. The observed incubation time, τ , increases exponentially with the growth temperature (Fig.5.3), according to the Arrhenius law.

The nucleation energy was calculated from a linear fit to the $\ln(\tau) = f(1/kT)$ relation (inset in Fig. 5.3.b) and was found to be 7.5 ± 0.5 eV. This value is for GaN nucleating on AlN, with Ga and N growth rates equal to 84.6 nm/h and 430 nm/h. In the case of GaN nucleating on a Si_xN_y layer, the nucleation energy found throughout the literature varies from 4.9 eV to 10.2 eV in different works [6, 11]. The wide range of the nucleation energy values recorded, could be due to the different conditions used for NW growth, and the different methodologies used for evaluating the incubation time.

As highlighted in the beginning of this section, the substrate temperature is only one condition that affects the Ga adatom kinetics. Another important factor, that should be taken into account (especially when comparing MBE growth results) that defines the Ga adatom density is the flux for Ga and N atoms used and their ratio III/V flux ratio). To this end, when comparing with the work [2], that used similar fluxes with the ones used in our exper-

iments ($F_{Ga}=93.6$ nm/h, $F_N = 360$ nm/h), we find a similar change in the density reduction with increasing the substrate temperature.

The above findings contribute to improving our physical understanding for the role of substrate temperature in the NW formation, for the case that a thin AlN prelayer is used. As the substrate temperature increases, the nucleation of the NWs is suppressed, due to the increase in the incubation time, as described by the Arrhenius law. The increased incubation period at high substrate temperatures corresponds to less time for the NW elongation, during the total 180 min of growth. This results in shorter NWs, compared to the lower- T_{sub} samples. The correlation of the incubation time with the final dimensions and morphological characteristics of NWs, does not allow us to securely isolate the effect of temperature on the NW elongation stage. In order to achieve this, we followed a two-step growth process, as described in the following section.

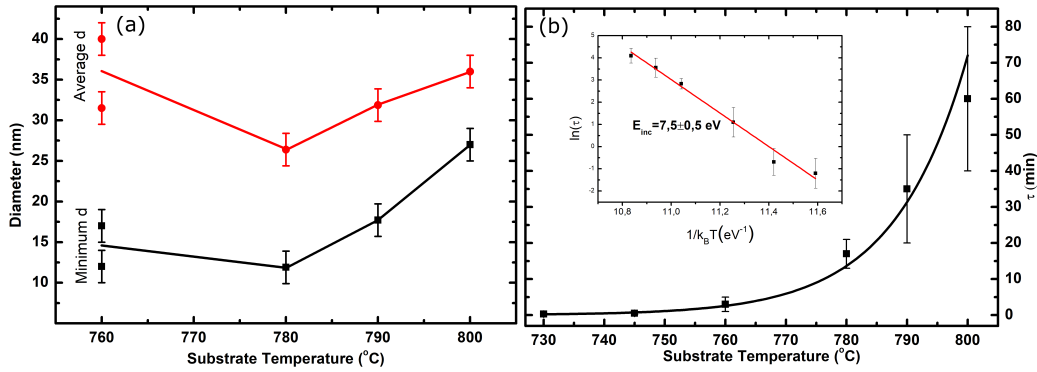


Figure 5.3: Graphs showing (a) the average (red circles) and minimum (black squares) diameter as a function of temperature and (b) the time needed for the appearance of the first GaN 3D spots in the RHEED pattern, τ , as a function of temperature. Samples with GaN NWs grown at 760°C, 780°C, 790°C and 800°C for a duration of 3h, under identical growth conditions (see text) were used. Additionally for (b), RHEED observations for samples grown using the same Ga and N fluxes, at temperatures of 730°C and 745°C for the first 20 min were used. The inset in (b) shows the linear fit performed for the calculation of the E_{inc} of GaN on the crystalline AlN prelayer used.

5.2 Two-step growth

Having established the role of the substrate temperature on the nucleation of GaN NWs on a thin AlN prelayer on Si (111), we now turn our attention to

the substrate temperature effect on the NW elongation. Using the findings from section 5.1, we chose a low- T_{sub} initial growth stage (IGS) in order to achieve a fast NW nucleation. The second and final growth stage (FGS) of GaN NWs was at a higher substrate temperature, in order to suppress further nucleation of the NWs [2, 12], and isolate the nucleation from elongation process. Although this would ensure a faster nucleation, it was initially unclear how the duration of the initial growth stage would affect the final result. For this reason, an initial series of samples was focused on the effects of the IGS time duration (t_{IGS}). After finding the optimal t_{IGS} , a second series of samples was grown focussing on the role of the temperature during the FGS, i.e., of the elongation stage of the NWs. A short description of the samples used, that includes the substrate temperature, time duration and sample name can be found in Table 5.1. The N and Ga fluxes, and the total GaN deposition time were identical to the samples grown for the study of substrate temperature effects in the one-step growth process.

The samples had the same T_{IGS} and t_{IGS} , but different T_{FGS} .

5.2.1 The role of the duration of the low substrate temperature step

Three samples, with an identical T_{IGS} of 730°C and different t_{IGS} (3, 6 and 20 min, respectively) were grown. The T_{FGS} was constant for all samples, and equal to 780°C. The total deposition time for active N and Ga atoms was 3 h for all three samples. These samples were compared with the one-step growth, at 780°C. In Fig. 5.4, the cross-section (5.4.a, b, c and d), tilted (5.4.e, f, g and h) and top view (5.4.i, j, k and l) SEM micrographs of these samples are shown.

All the samples that included a first step of GaN grown at 730°C exhibited a rough parasitic layer at the base of the NWs. This layer is formed due to the increased density of Ga adatoms on the surface at this substrate temperature, owing to the lower Ga desorption rate [1, 10]. In order to have a better understanding of this layer's morphology, a sample was grown for 20 min at 730°C. SEM micrographs of this sample (Fig. 5.5) reveal that some NWs nucleated within the parasitic layer.

Figure 5.6.a shows the average and maximum values of the height of GaN NWs, compared to the t_{IGS} used in the various two-step grown samples. The average NW height of all the samples, with a low- T_{sub} initial growth stage is $\sim 35\%$ larger than that of the one-step growth (with $t_{IGS} = 0$). This is attributed to the faster nucleation at 730°C, as concluded from RHEED observations (Fig. 5.3.b). The average GaN NW height for the two-step

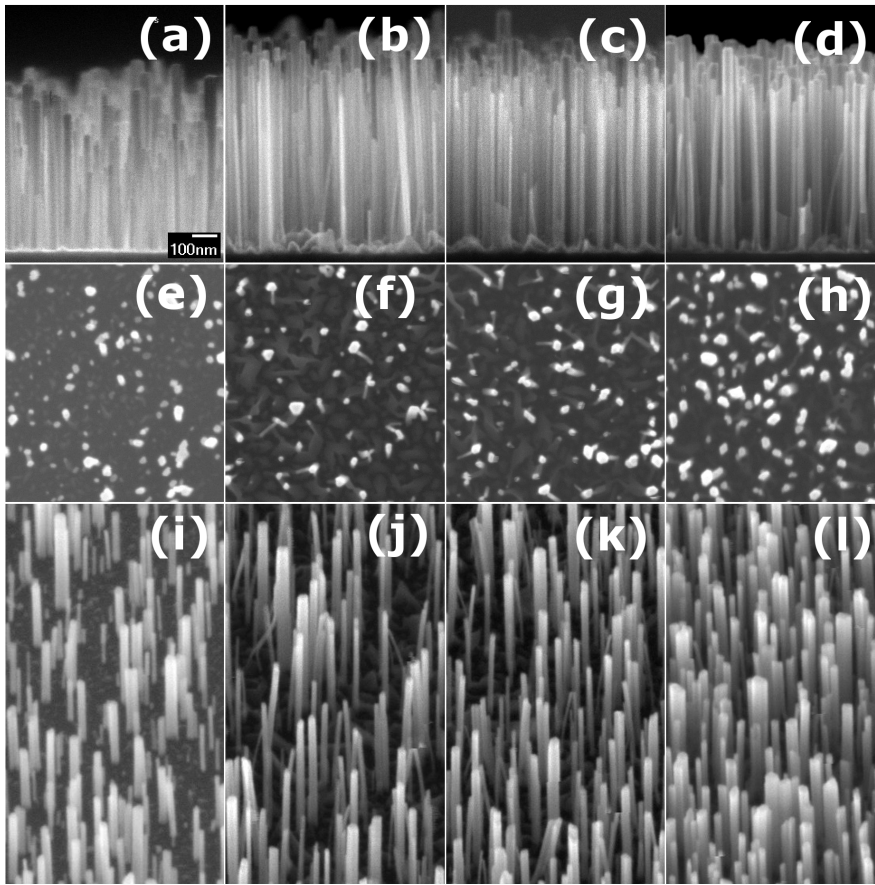


Figure 5.4: SEM micrographs of cross-section (top row), top (middle row) and tilted view (bottom row) for samples with $t_{IGS} = 0$ (a, e, i), $t_{IGS} = 3$ min (b, f and j), $t_{IGS} = 6$ min (c, g, k) and $t_{IGS} = 20$ min (d, h, l).

samples does not vary significantly for the different t_{IGS} values studied. The same behaviour is also observed for the maximum GaN NW height values measured in the various samples.

In contrast to the average height of the GaN NWs, a significant difference is observed in the height distribution of NWs, as shown in Fig. 5.6.b. All the samples with a two-step process have a narrower distribution than that of the one-step process ($t_{IGS} = 0$ min). In the case of $t_{IGS} = 3$ min and 6 min, the height distribution contains some outliers i.e., a few short NWs away from the main distribution. As the nucleation of GaN NWs continues throughout the NW growth process [2], we attribute the existence of these extremely short NWs in a delayed nucleation, that occurred during the later stages of the FGS. However, such outliers are closer to the main distribution for the case of the sample with $t_{IGS} = 20$ min suggesting that the delayed

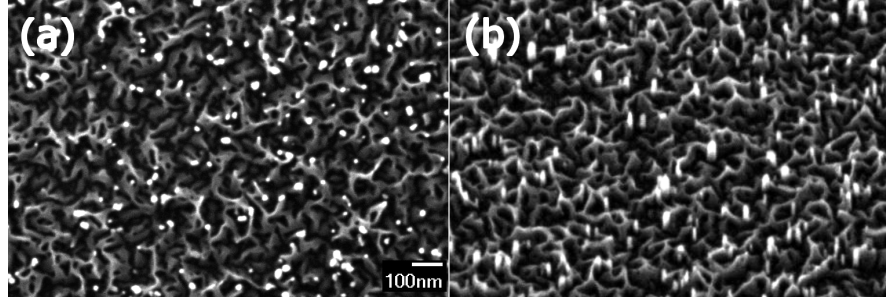


Figure 5.5: SEM micrographs of the sample growth at $T_{sub} = 730\text{ }^{\circ}\text{C}$, for a total growth duration of 20 min, with N and Ga fluxes equal to 430 nm / h and 84.6 nm / h ; (a) top and (b) tilted view.

NW nucleation is minimal in this case.

GaN NW density measurements are also in agreement with the suppressed nucleation during the FGS. The NW number density measured for the single step grown sample at 730°C for 20 min, has a larger density ($12 \times 10^9\text{cm}^{-2}$) than that for samples with $t_{IGS} = 3$ and 6 min ($7.5 \times 10^9\text{cm}^{-2}$ and $9 \times 10^9\text{cm}^{-2}$ respectively). The larger density suppresses the formation of new NWs due to the increased diffusion of Ga adatoms to the already formed NWs [9]. In accordance with this, the NW number density increases with t_{IGS} , as shown in Fig. 5.7. We conclude that the majority of the nucleation events for the sample with $t_{IGS} = 20$ min occur during the lower temperature IGS, and negligible nucleation occurs during the 160 min duration of the FGS.

In the initial work of Carnevale et al [2] which proposed a two-step GaN NW growth process, the IGS is referred to as the nucleation stage. We prefer to distinguish the NW nucleation stage from the IGS, because in some occasions both the NW nucleation stage and part of the NW elongation stage [3] occur during the IGS, while nucleation of isolated NWs can also occur during the FGS.

The relation of the GaN NW diameter on the duration of the initial growth stage (t_{IGS}) is shown in Fig. 5.8. An increased diameter is observed for the sample with $t_{IGS} = 20$ min. We attribute this to the longer elongation stage taking place at 730°C , for NWs that nucleated in the first minutes of the IGS. This would result in NWs with larger diameters, according to the larger radial growth that has been found for NWs that grow at lower temperatures [2, 5].

Our results show a correlation of the duration of the low temperature IGS, with the morphological characteristics of the NWs. While the height of the NWs does not show any dependence on the t_{IGS} , the height distribution revealed a suppression of the nucleation of NWs throughout the FGS when

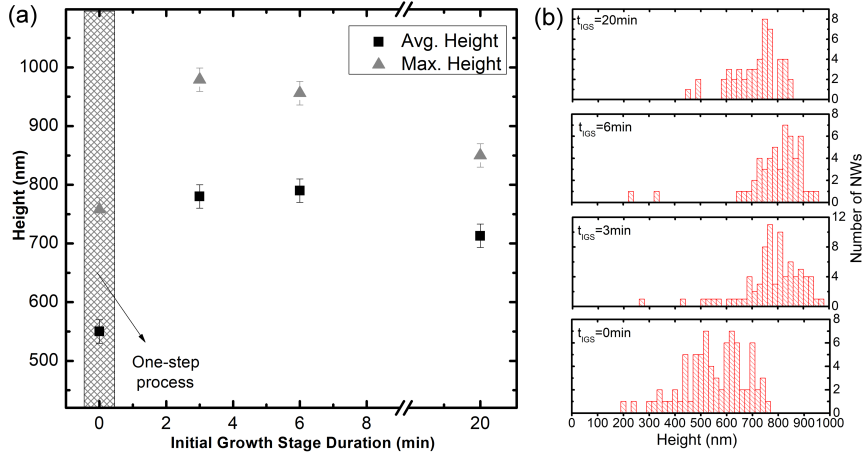


Figure 5.6: (a) Average and maximum heights of the GaN NWs grown with different time durations of the IGS stage ($t_{IGS} = 0, 3$ min, 6 min and 20 min) and with $T_{IGS} = 730^\circ\text{C}$ and $T_{FGS} = 780^\circ\text{C}$. (b) the height distributions for samples grown with different duration of the initial growth stage.

a larger t_{IGS} was used. The NW diameter and density are correlated with the duration of the IGS. For the growth conditions used in our MBE setup, control over the range of 26 - 40 nm for the diameter and $7,5 - 13 \times 10^9 \text{ cm}^{-2}$ for the density can be achieved, by varying the t_{IGS} between 3 and 20 min.

Our findings can be compared with the work of Zettler et al [12]. Although their growth conditions ($F_{Ga} = 330 \text{ nm/h}$, $F_N = 660 \text{ nm/h}$) were different from our experiments, they performed a similar study on the duration of the IGS, for GaN NWs grown on nitridated Si (111). Their samples were grown with $T_{IGS} = 815^\circ\text{C}$ and $T_{FGS} = 845^\circ\text{C}$, for a total duration of 270 min. Interestingly, although they use a higher Ga growth rate by $\sim 400\%$, they had control over a similar range of NW density with the work presented in this chapter (namely, $\sim 8.5 - 12 \times 10^9 \text{ cm}^{-2}$ for t_{IGS} between 50 and 80 min, respectively). When comparing the NW heights, they also found negligible effect of the t_{IGS} , since the measured NWs for all the two-step samples were in the range of 1.6-1.7 μm .

A key difference between the results of the two works is the presence of the initial GaN parasitic layer in our samples. The use of an initial AlN layer, in combination with the low T_{sub} chosen during the IGS, enhances the 3D islands nucleation of GaN, resulting in the formation of GaN NWs together with the GaN parasitic layer, for all three samples grown. In contrast, in the work of Zettler et al [12], the initial growth durations chosen were such that the NW nucleation stage would be close to the end (for $t_{IGS} = 80$ min), an intermediate stage (for $t_{IGS} = 65$ min), and at the early stages for the

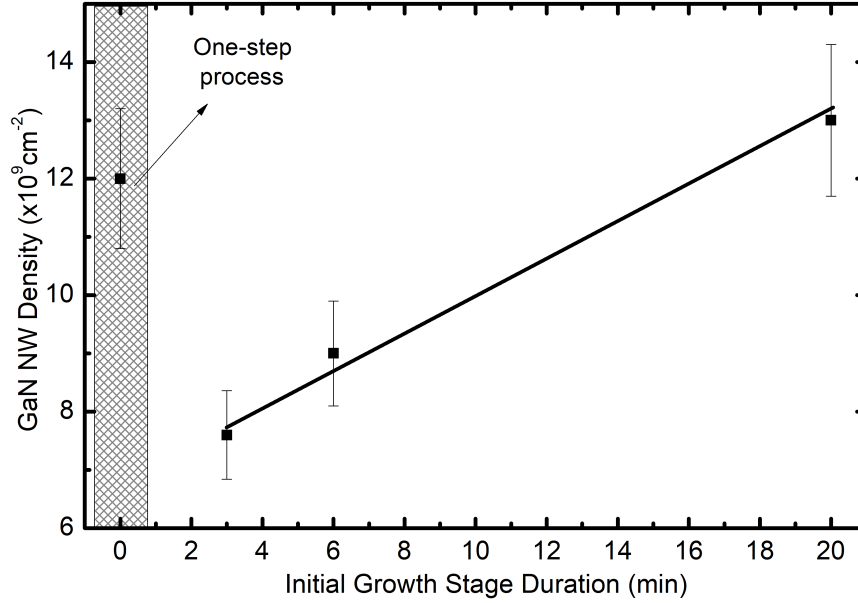


Figure 5.7: The density of GaN nanowires in samples with different duration of the initial growth stage, at $T_{IGS} = 730^\circ \text{C}$, and the same total growth time (3h) and growth conditions ($F_{Ga} = 84.6 \text{ nm/h}$, $F_N = 430 \text{ nm/h}$, $T_{FGS} = 780^\circ \text{C}$). The values of the sample grown directly at 780°C for 3h ($t_{IGS} = 0 \text{ min}$) are also depicted, for comparison with the one step growth. The line is guide for the eyes.

shorter IGS duration (for $t_{IGS} = 50 \text{ min}$). Their choice resulted in separately grown NWs, without the presence of any GaN layer in between them.

5.2.2 The role of substrate temperature during the elongation stage

After finding the optimal initial growth conditions during the IGS, that indicate that the nucleation of new NWs is minimal during the FGS, we turn our attention to the role of the T_{FGS} at the second growth step (T_{FGS}) on the NW morphology. We prepared samples with an identical IGS ($T_{IGS} = 730^\circ \text{C}$, and $t_{IGS} = 20 \text{ min}$) and different T_{FGS} for the rest of the 160 min of GaN growth. The chosen substrate temperatures for the FGS were 750°C , 760°C , 770°C , 780°C , 790°C and 800°C .

Figure 5.9 shows SEM micrographs of the cross-section, top-view and side-view of the samples. From the cross-section micrographs we see that the average NW height is much lower for the higher substrate temperatures of

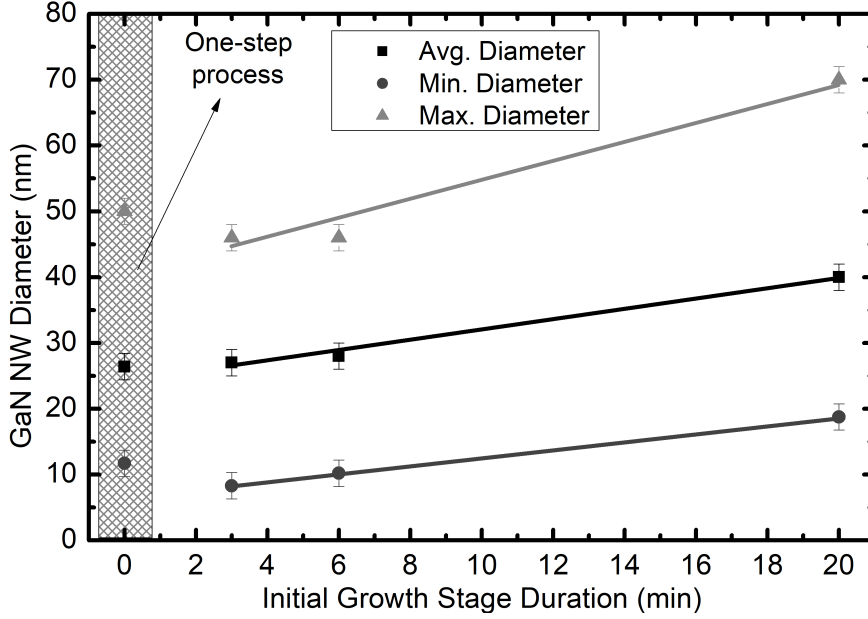


Figure 5.8: Diameter of the GaN NWs, for samples with different initial-growth durations studied (t_{IGS}), at $T_{IGS} = 730^\circ$, and the same total growth time (3h) and growth conditions ($F_{Ga} = 84.6 \text{ nm} / \text{h}$, $F_N = 430 \text{ nm} / \text{h}$, $T_{FGS} = 780^\circ \text{C}$).

790°C and 800°C . This is better shown in the plot of Fig. 5.10, where the average NW height compared to the T_{FGS} is shown. The average NW height increases up to $\sim 20\%$ for T_{FGS} changing from 750°C to 770°C , where the maximum value for the average height is observed (860 nm). As the T_{FGS} further increases, the height decreases down to $\sim 60\%$ of the maximum value, in the case of the sample with $T_{FGS} = 800^\circ \text{C}$.

The maximum height observed at $T_{FGS} = 770^\circ \text{C}$ reveals a change in the GaN nucleation rate at the NW top surface and possible decomposition of GaN at $T_{sub} > 770^\circ \text{C}$. The change of NW height (and thus of the growth rate) may be attributed mainly to the number of adatoms that reach the top NW surface, assuming a low decomposition rate at this temperature. The increased nucleation rate for temperatures up to 770°C , should correspond to an increased amount of Ga adatoms reaching the top NW surface, while a decreasing nucleation rate for the higher temperatures should result from less Ga adatoms reaching the top surface. The above effect is governed by the adatom diffusion length on the NW side facets, which is limited by Ga incorporation (chemisorption) and desorption. Our results suggest that the diffusion length of Ga adatoms on the m-plane side facets increases for sub-

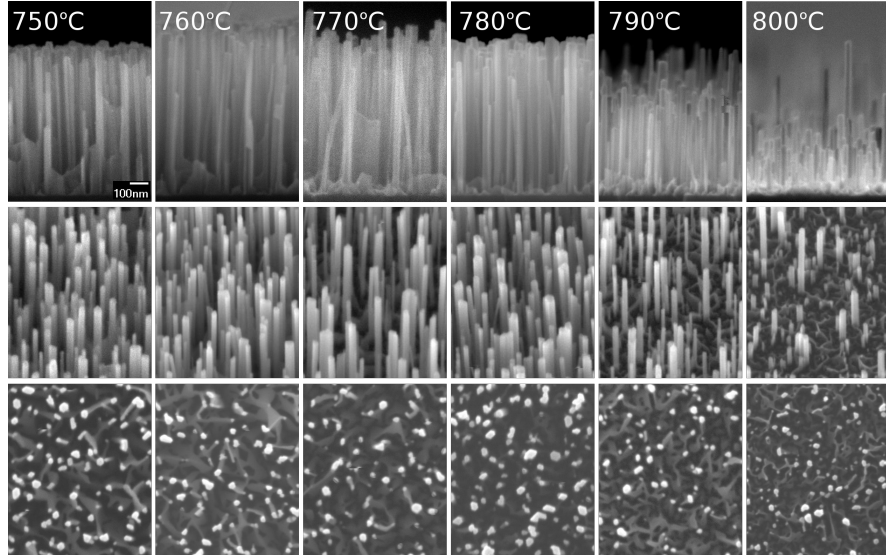


Figure 5.9: SEM images of the cross-section (top row), tilted (middle row) and top (bottom row) view for samples grown with identical growth conditions ($T_{IGS} = 730^\circ$, $t_{IGS} = 20$ min, $F_{Ga} = 84.6$ nm/h, $F_N = 430$ nm/h), but with different T_{FGS} , equal to 750° C, 760° C, 770° C, 780° C, 790° C and 800° C.

strate temperatures up to 770° C, while further increase of the temperature results in the reduction of the diffusion length and/or the increased desorption from the top c-plane surface of the NW. A similar behaviour has been reported in the work of Consonni et al [4], but the crucial temperature that the maximum growth rate was observed was 790° C. The results are in very good agreement, considering the inaccuracies in the determination of substrate temperature in different MBE systems. However, this T_{sub} difference may also be related to a different balance of the surface kinetic processes during growth due to the higher Ga-flux ($F_{Ga}=162$ nm/h), and N-flux in that work [4]. Both, the higher Ga-flux and N-flux would compensate for the increased Ga adsorption during temperature increasing [7].

A comparison of the average heights of GaN NWs in the two-step growth process versus to the one-step growth process can be seen in the graph shown in Fig. 5.10. At higher substrate temperatures, the height of the NWs is significantly larger when a low- T_{sub} (730° C) IGS precedes the final high- T_{sub} NW growth (FGS). For the higher T_{sub} studied, 800° , the sample with the low- T_{sub} initial growth stage exhibited NWs with height 237 % larger compared to the NWs of the sample grown directly, at 800° C (one-step growth).

The density of GaN NWs grown by a two-step growth process does not show any trend with the T_{sub} of the final growth stage (T_{FGS}), as shown

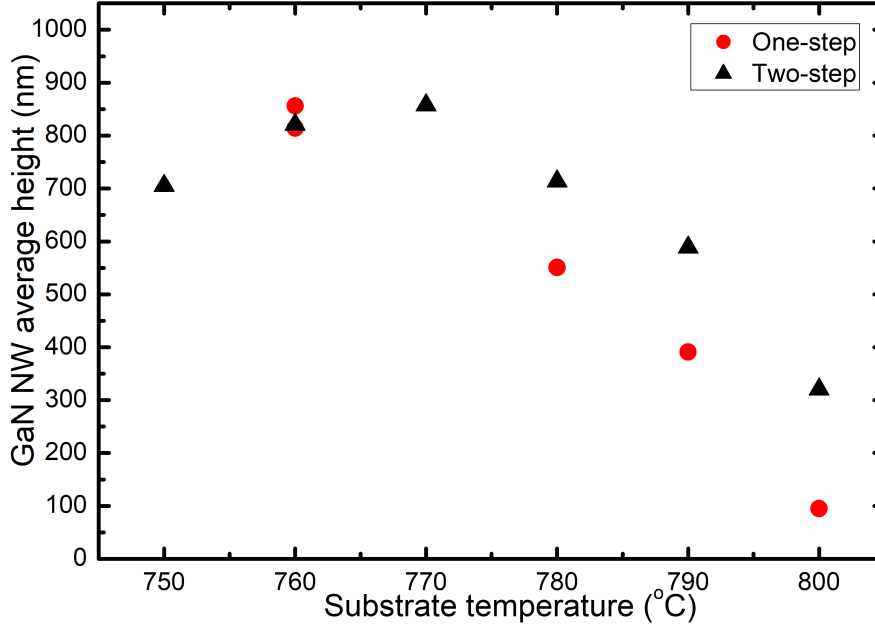


Figure 5.10: The height of GaN NWs grown on 1.5 nm AlN/Si (111) by one-step and two-step growth processes, at different substrate temperatures. In the case of the two-step process the value of T_{FGS} used for 160 min GaN NW growth is used in the plot. The first step of 20 min growth, was accomplished at 730°C. The Ga and N fluxes used were identical for all the samples (84.6 nm / h and 430 nm / h).

in Fig. 5.11. The values measured for all the two-step grown samples are between 9 and $15 \times 10^9 \text{ cm}^{-2}$. A clear observation for the samples grown at the highest temperatures of 790° and 800° is that the density of the NWs grown by the two-step growth process is significantly higher than the one-step growth process, as shown in Fig. 5.11. In the case of the $T_{sub} = 800^\circ\text{C}$, the NW density difference is more than two orders of magnitude (from 9.7×10^7 to $15 \times 10^9 \text{ cm}^{-2}$). This is expected due to the increased Ga desorption at these temperatures, leading to an intense suppression of NW nucleation from the beginning of the growth in the single-step growth process.

A trend for the reduction of the average NW diameter with increasing T_{FGS} was observed, as shown in Fig. 5.12. A total reduction of 33% is observed for T_{FGS} increasing from 750°C to 800°C. This is again attributed to the reduced radial growth at higher substrate temperatures [2, 5], that was also observed in the experiments described in the previous section 5.2.1.

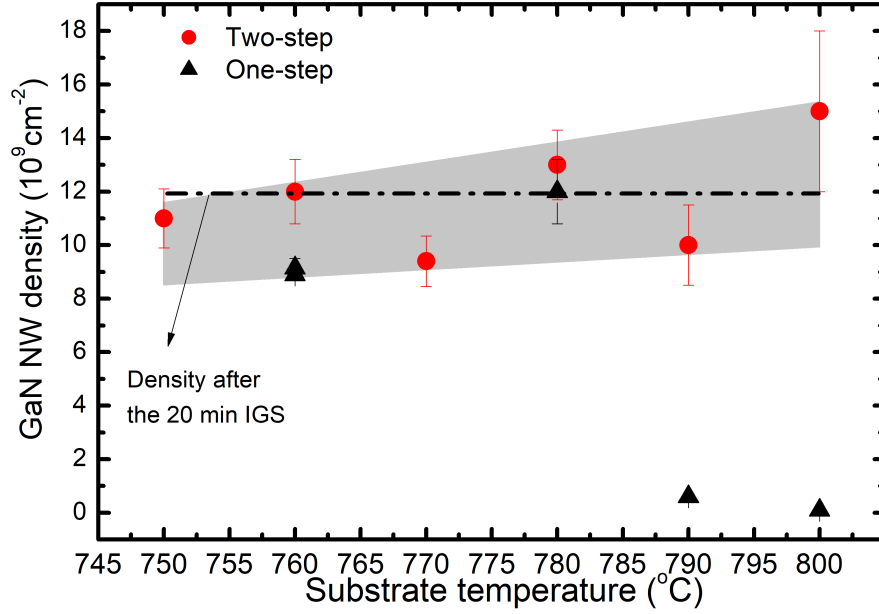


Figure 5.11: The density of GaN NWs grown by a one-step or two-step growth process at different substrate temperatures. In the case of two-step process, initial GaN growth was carried out at 730°C for 20 min. The total growth time for all GaN NW samples was 3h..

5.3 Conclusions

Throughout this chapter we studied the role of temperature on the nucleation and on the elongation stages of GaN NWs. The nucleation of GaN NWs is suppressed as the substrate temperature increases, due to the increased Ga desorption. A nucleation energy of 7.5 ± 0.5 eV was calculated from RHEED measurements of the GaN NW incubation time. A two step growth process with an initial low T_{IGS} and a higher T_{FGS} allowed the nucleation of GaN NWs at the initial growth stage, and their elongation at a high T_{FGS} that would not be feasible with a one-step growth process. Varying the duration of the initial growth stage, allowed for control over the range of 26 - 40 nm for the diameter and 7.5 - 13 $\times 10^9$ cm⁻² for the density. A maximum height was observed for $T_{FGS} = 770$ °C, in a series of samples with identical initial growth stages, and attributed to a significant reduction in the diffusion length of the Ga adatoms on the NW side facets (m-planes) and the increased desorption on the top c-plane surface for $T_{sub} > 760$ °C.

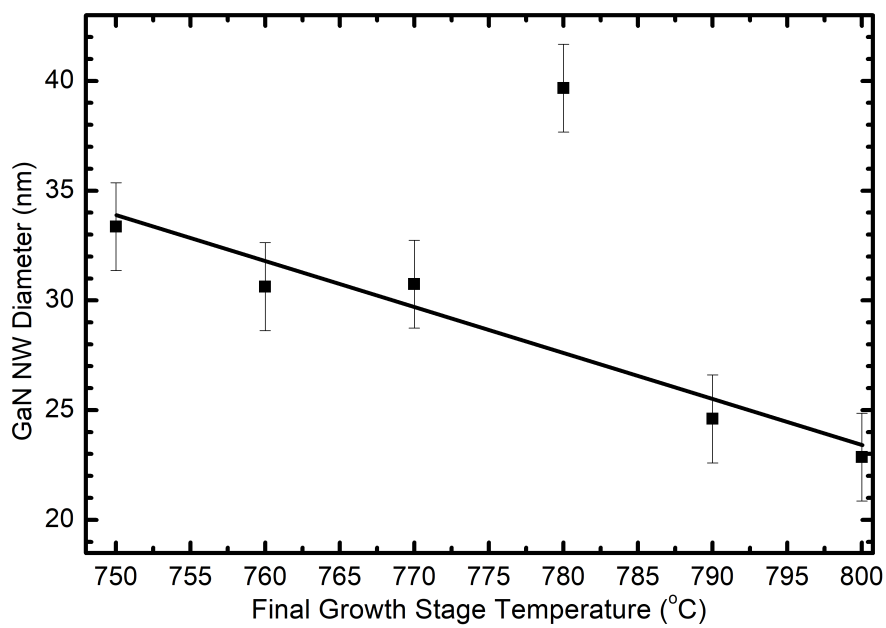


Figure 5.12: The GaN NW average diameter, measured from SEM micrographs of samples grown with a two-step growth process, at different substrate temperatures during the final growth stage. The initial substrate temperature, T_{IGS} was 730°C, and the initial growth duration was 20 min. The Ga and N fluxes used were identical for all the samples (84.6 nm/h and 430 nm/h).

Bibliography

- [1] CALLEJA, E., RISTIC, J., FERNANDEZ-GARRIDO, S., AND M. A. SANCHEZ-GARCIA, L. C., GRANDAL, J., TRAMPERT, A., JAHN, U., SANCHEZ, G., GRIOL, A., AND B.SANCHEZ. "Growth, morphology, and structural properties of group-III-nitride nanocolumns and nanodisks". *Phys. Stat. Solidi (b)* 244 (2007), 2816.
- [2] CARNEVALE, S. D., YANG, J., PHILLIPS, P. J., MILLS, M. J., AND MYERS, R. C. "Three-Dimensional GaN/AlN Nanowire Heterostructures by Separating Nucleation and Growth Processes". *Nano Lett.* 11 (2011), 866.
- [3] CONSONNI, V. "Self-induced growth of GaN nanowires by molecular beam epitaxy: A critical review of the formation mechanisms". *Phys. Status Solidi RRL* 7, 10 (2013), 699.
- [4] CONSONNI, V., DUBROVSKII, V. G., TRAMPERT, A., GEELHAAR, L., AND RIECHERT, H. "Quantitative description for the growth rate of self-induced GaN nanowires". *Phys. Rev. B* 85 (2012), 155313.
- [5] CONSONNI, V., KNELANGEN, M., TRAMPERT, A., GEELHAAR, L., AND RIECHERT", H. "Nucleation and coalescence effects on the density of self-induced GaN nanowires grown by molecular beam epitaxy". *Appl. Phys. Lett.* 98 (2011), 071913.
- [6] CONSONNI, V., TRAMPERT, A., GEELHAAR, L., AND RIECHERT, H. "Physical origin of the incubation time of self-induced GaN nanowires". *Appl. Phys. Lett.* 99 (Jul 2011), 033102.
- [7] FERNANDEZ-GARRIDO, S., KOBLMULLER, G., CALLEJA, E., AND SPECK, J. S. "In situ GaN decomposition analysis by quadrupole mass spectrometry and reflection high-energy electron diffraction". *J. Appl. Phys.* 104 (2008), 033541.

- [8] IBACH, H., Ed. "*Physics of Surfaces and Interfaces*". Springer-Verlag Berlin Heidelberg, 2006.
- [9] KRUSE, J. E., LYMPERAKIS, L., EFTYCHIS, S., ADIKIMENAKIS, A., DOUNDOULAKIS, G., TSAGARAKI, K., ANDROULIDAKI, M., OLZIER-SKY, A., DIMITRAKI, P., IOANNOU-SOUGLERIDIS, V., NORMAND, P., KOUKOULA, T., KEHAGIAS, T., KOMNINO, P., KONSTANTINIDIS, G., AND GEORGAKILAS, A. "Selective-area growth of GaN nanowires on SiO₂-masked Si (111) substrates by molecular beam epitaxy". *J. Appl. Phys.* 119 (2016), 224305.
- [10] RISTIC, J., CALLEJA, E., FERNANDEZ-GARRIDO, S., CERUTTI, L., TRAMPERT, A., JAHN, U., AND PLOOG, K. H. "On the mechanisms of spontaneous growth of III-nitride nanocolumns by plasma-assisted molecular beam epitaxy". *J. Cryst. Gr.* 310 (2008), 4035.
- [11] SOBANSKA, M., KORONA, K. P., ZYTKIEWICKZ, Z. R., KLOSEK, K., AND TCHUTCHULASHVILI, G. "Kinetics of self-induced nucleation and optical properties of GaN nanowires grown by plasma-assisted molecular beam epitaxy on amorphous Al_xO_y". *J. Appl. Phys.* 118 (2015), 184303.
- [12] ZETTLER, J. K., CORFDIR, P., GEELHAAR, L., RIECHERT, H., BRANDT, O., AND FERNANDEZ-GARRIDO, S. "Improved control over spontaneously formed GaN nanowires in molecular beam epitaxy using a two-step growth process". *Nanotechnology* 26 (2015), 445604.

Spontaneous growth of GaN nanowires on Si (111) surfaces: intentional and unintentional Si nitridation

6.1 Introduction

One of the factors that determine the nucleation of GaN Nws, and thus their properties is the initial surface on which Ga and active N and Ga atoms are deposited [3, 6, 11, 19, 24]. In the case of the Si (111) substrates, when active N and Ga atoms are deposited on the substrate at high temperatures ($\sim 760^\circ\text{C}$), a thin amorphous interfacial layer (IL) of Si_xN_y has been reported to form between GaN and the Si surface [3, 5, 10, 11, 13, 19, 23]. The process of nitridation of the Si substrate happens when active nitrogen species reach the Si surface, and can be either intentional or unintentional. In the first case, a nitridation treatment precedes GaN deposition [24], while in the latter case it occurs when active N and Ga atoms reach the Si surface simultaneously [6].

In this chapter, both cases will be presented, and a systematic comparison of spontaneous GaN NW growth on intentionally and unintentionally nitridated Si (111) substrates will be presented. A study of the morphology, structure and optoelectronic properties of the GaN NWs in the two different cases will lead to the correlation of the NW properties with the nanostructure of the GaN/Si interface. In particular, the results reveal how the treatment of the Si surface affects the height distribution, average diameter, angular tilt and twist dispersion, and photoluminescence spectra of the grown NWs.

6.2 Experimental details

Two samples, A and B were grown on on-axis Si (111) substrates. In case of sample A, GaN was deposited directly on a bare Si (111) surface. In case of sample B, the Si (111) surface had been exposed to active nitrogen for 20 minutes prior to the GaN deposition. The substrate temperature during all the steps in both samples was 760°C. The power of the RF source was 300W and the flow rate was 1.6 standard cubic centimeter per minute (sccm). The GaN NW growth lasted for 180 min with N/Ga flux ratio equal to 5. The Ga flux corresponded to an equivalent GaN growth rate of 85 nm/h. Reflected High Energy Electron Diffraction (RHEED) was used for in-situ monitoring during Si surface preparation and GaN growth. The Si (111) substrates were chemically and thermally cleaned as described in section A. Additionally, two Si substrates were removed from the MBE system, one after Si oxide desorption and the other after the exposure of the clean Si surface to the nitrogen beam at 760°C for 20 min, and they were investigated by Atomic Force Microscopy (AFM).

6.3 Experimental results

RHEED showed the 7x7 reconstruction on the thermally cleaned Si (111) surface for both samples, prior to exposure to active nitrogen (N) and Ga fluxes. Depending on the arrangement of the shutters in the growth chamber, there are reports of exposure of the substrate surface to active nitrogen leakage although the shutters are closed, beginning from the time that RF N-plasma is ignited [6, 14, 15, 16, 20]. This leakage is usually confirmed by modification of the 7x7 RHEED pattern. In the used MBE system, which is equipped with a main shutter for the control of active nitrogen exposure, and for the employed nitrogen flux, the 7x7 pattern on the RHEED screen was clearly visible even after the ignition of the N plasma, indicating no active nitrogen incidence on the Si surface. However the Si surface transformed to amorphous material after its 20 min exposure to the nitrogen beam at 760°C.

AFM observations on the Si (111) substrate, which was removed from the MBE system after oxide desorption, revealed a smooth Si (111) surface consisting of monolayer height steps and terraces with typical width of ~ 150 nm, as it would be expected for a misorientation of the Si substrate surface of 0.1° from the exact (111) plane. The morphology of the nitrated Si surface was characterized by a high density of small islands and a much fainter contrast of the Si (111) surface steps. This morphology exhibited no similarities with the large islands with crystallographic shapes that were observed by high

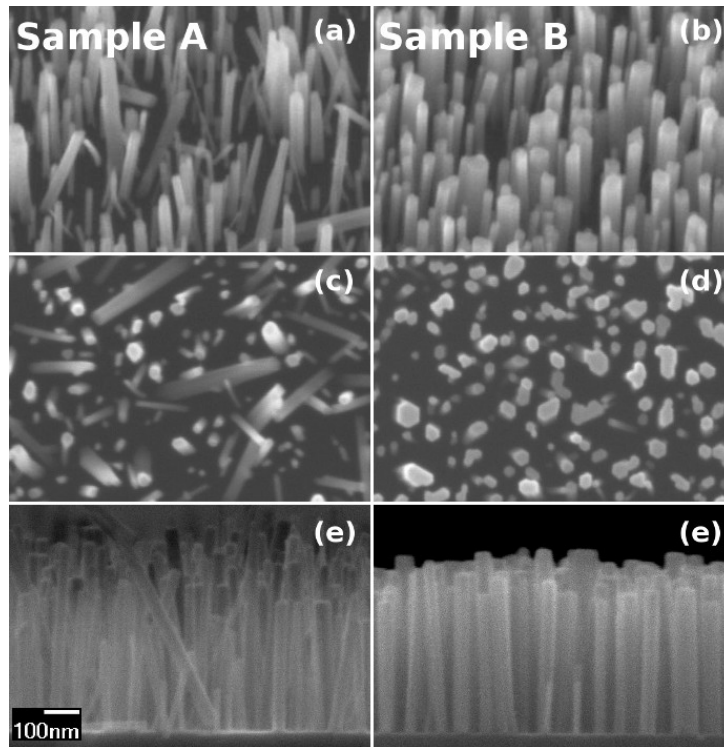


Figure 6.1: FE-SEM micrographs for observation at (a, b) 30 tilt view, (c, d) top view and (e, f) cross-section view showing the GaN nanowires of sample A (a,c,e) and sample B (b,d,f). Sample A of direct GaN growth on Si (111) exhibits increased misalignment of nanowires compared to sample B of GaN growth on intentionally nitridated Si (111) substrate.

temperature nitridation in ref. [24]. The rms surface roughness extracted from $1 \times 1 \mu\text{m}^2$ AFM scans was 0.21 nm.

FE-SEM observations showed that intentional Si nitridation improved the alignment and height homogeneity and increased the diameter of the NWs. No parasitic grained structures of GaN between the NWs were observed in any of the two samples. Figures 6.1.a and 6.1.b are cross-section FE-SEM images of samples A and B, respectively. A better alignment of the GaN NWs is evident for sample B (Fig. 6.1.b), consisting of GaN NWs grown on the intentionally nitridated Si. On the contrary, several inclined (tilted) nanowires are visible in Fig. 6.1.a, for sample A with direct GaN growth on Si. Analysis of the height of the NWs, from the cross-section FE-SEM images, revealed almost the same average height for the two samples (440 nm for sample A and 430 nm for sample B), but a significantly broader height distribution in the case of sample A, as shown in the plot of Fig. 6.2. The

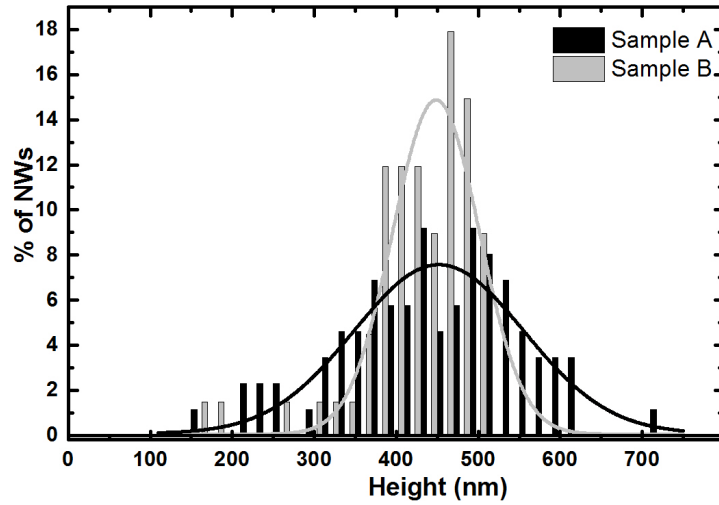


Figure 6.2: Height distribution of the two samples, as measured by FE-SEM images. Sample A (B) height distribution is denoted with black color (grey color). The curves serve as a guide for the eye.

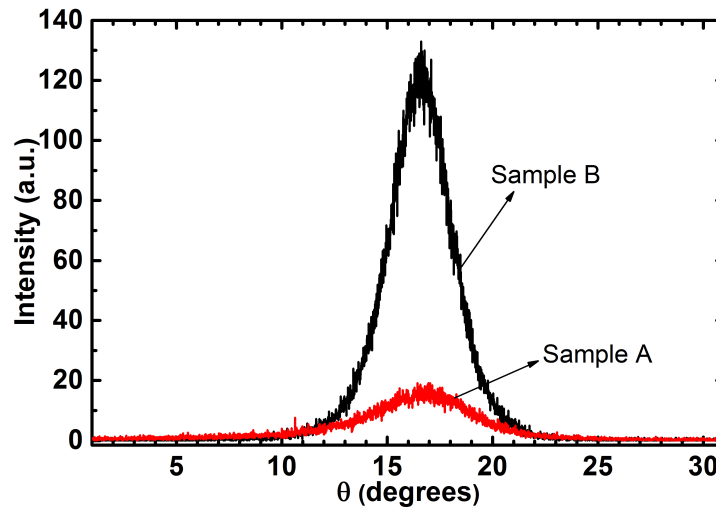


Figure 6.3: XRD rocking curves around the (0002) GaN reflection for samples A and B.

calculated standard deviation for the NW heights was 107 nm for sample A and 68 nm for sample B. The diameters of the NWs were determined from 30 tilt view FE-SEM images and the calculated average NW diameter was 25 nm for sample A and 40 nm for sample B.

The XRD measurements confirmed that the GaN NWs grow along the [0001] axis and they were in agreement with the FE-SEM observations for

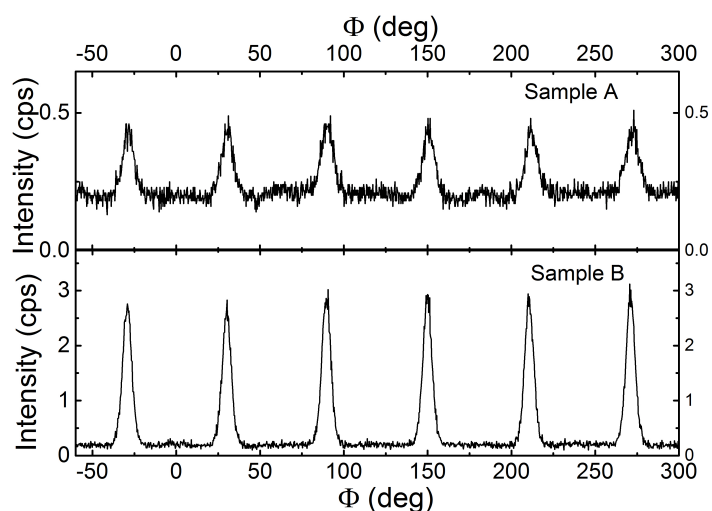


Figure 6.4: ϕ -scan of the (11.4) GaN planes, revealing the twist coherency, with the six-fold symmetry.

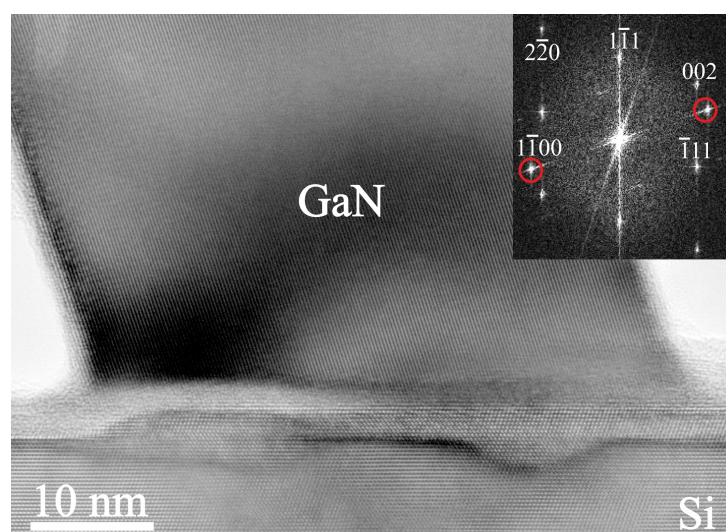


Figure 6.5: Cross-sectional HRTEM image of sample A, along the $[\bar{1}10]_{Si}$ zone axis, illustrating an inclined GaN NW nucleated directly on the Si surface. In the inset, the corresponding FFT diffractogram from the interfacial area shows the orientation relationship between the GaN NW and the Si substrate. Red circles denote the $[1\bar{1}00]$ -type reflections of wurtzite GaN.

the crystallographic alignment of the GaN NW crystals. Figure 6.3 shows the XRD -scans around the (0002) reflection of the two samples. The Full Width at Half Maximum (FWHM) of the (0002) GaN peak of sample B was

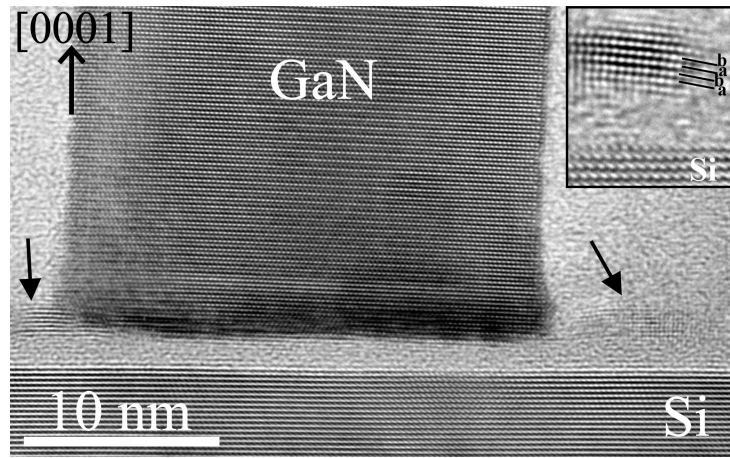


Figure 6.6: HRTEM image of sample B, viewed along the $[11\bar{2}0]_{\text{GaN}}//[\bar{1}10]_{\text{Si}}$ zone axes, showing a slightly inclined GaN NW grown on the thin amorphous Si_xN_y layer of the Si surface. Wurtzite GaN crystalline remnants (arrows) are depicted on either side of the NW.

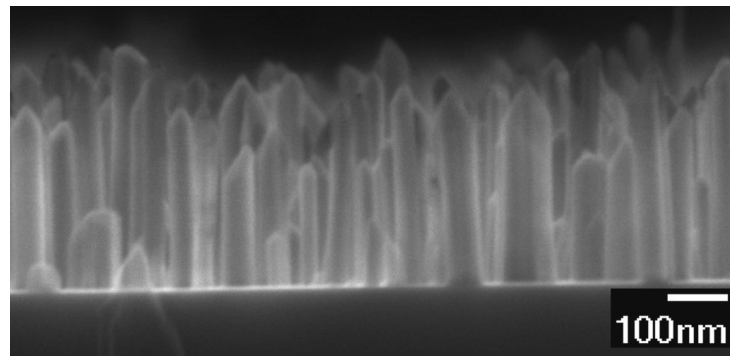


Figure 6.7: FE-SEM image of sample B, after the KOH etching, showing the characteristic etched top part of N-polar GaN NWs.

3.4° while that of sample A was 5.6° . It is clear that intentional nitridation of the Si surface (sample B) resulted in a reduced tilt angle dispersion of the GaN NWs, in comparison to direct GaN on Si growth (sample A).

The angular twist dispersion of the NW crystals was evaluated by XRD ϕ -scans for the asymmetric (11.4) reflections of GaN, and the results are shown in Fig. 6.4. Six-fold symmetry for the (11.4) planes is apparent in both samples. However, the NWs of sample B (nitridated Si) exhibited significantly stronger peak intensities and smaller FWHM values compared to sample A (direct growth), indicating that a larger percentage of GaN NWs was grown with a dominant epitaxial relation with respect to the Si

crystal. The peak intensities were 2.86 counts per second (cps) for sample B compared to 0.45 cps for sample A, whilst the FWHM values were 6.2° and 8.1° , respectively.

An inclined GaN NW nucleated on bare 111 Si surface (sample A) is shown in the cross-sectional HRTEM image of Fig. 6.5, along the $[\bar{1}10]_{Si}$ projection direction. The NW is tilted 19° with respect to the $[1\bar{1}1]_{Si}$ growth direction. Roughening of the Si 111 surface comprising steps, pits and mounts is observed at the nucleation site of the NW, and can be attributed to the unavoidable interaction of the active N species with the Si surface atoms, prior to NWs growth. Simultaneously, this interaction leads to unintentional nitridation of the Si surface and the formation of a thin amorphous Si_xN_y layer, as seen on either side and partially under the inclined NW. In the HRTEM image of Fig. 6.5, only the $(1\bar{1}00)$ planes of the GaN wurtzite structure are resolved, whereas in the corresponding fast Fourier transform (FFT) diffractogram at the GaN/Si interface (inset) the 0002 spatial frequencies are absent under the specific diffracting conditions. This means that the orientation of the NW is far from the expected $[11\bar{2}0]$ zone axis, and the $[0001]_{GaN}$ axis is not only tilted, but also twisted about the $[1\bar{1}1]_{Si}$ growth direction. Hence, no epitaxial relationship can be established for the inclined NWs. Moreover, a high density of tilted NWs also nucleated on the amorphous Si_xN_y layer, with NW tilting attributed to its roughness, resulting as a consequence of the uncontrollable growth. On the other hand, Si surface nitridation, prior to NWs growth, substantially improved the axial alignment of NWs, due to the formation of a homogenous 1.52 ± 0.11 nm thick Si_xN_y layer at the GaN/Si interface, which may also have accommodated any initial Si surface roughness, as shown in the HRTEM image of Fig. 6.6, recorded from sample B.

GaN crystalline remnants up to 2 nm thick are depicted on either side of the NW atop the Si_xN_y layer. The inset presents a magnified image of these nanocrystals, showing the ababab stacking of the wurtzite structure, which might have functioned as potential NW nuclei at the onset of NWs growth [6, 7]. Furthermore, the $(0001)_{GaN} // (1\bar{1}1)_{Si}$, $[11\bar{2}0]_{GaN} // [1\bar{1}0]_{Si}$ epitaxial relationship between the GaN and Si crystal lattices was obtained by selected area electron diffraction (SAED) patterns and HRTEM imaging. Among numerous NWs, occasional small tilts and twists of the $[0001]_{GaN}$ NWs growth axis relative to the $[1\bar{1}1]_{Si}$ growth direction were observed, as a consequence of local thickness fluctuations of the Si_xN_y amorphous interfacial layer.

KOH polarity tests revealed that the majority of the GaN NWs were grown with N-face polarity in both samples, with the possible exemption of a few NWs in sample A. The KOH etching reduced the height of the nanowires and revealed a change of the flat top surface of the NWs to a

sharpened edge, as shown in the FE-SEM image of Fig. 6.7 for sample B, which is characteristic for N-face GaN NWs [15]. In the case of sample A, the observation of a few short NWs with flat tops, after the KOH etching, may indicate that few short Ga-face NWs had also been grown. In the case of sample B, where there was clear etching for all the observed NWs, the averaged height of the NWs was 270 nm, revealing an etching rate of 5.3 nm/min in the 4M KOH aquatic solution (with a pH of 14.6, and total submerged time 30 min, at room temperature).

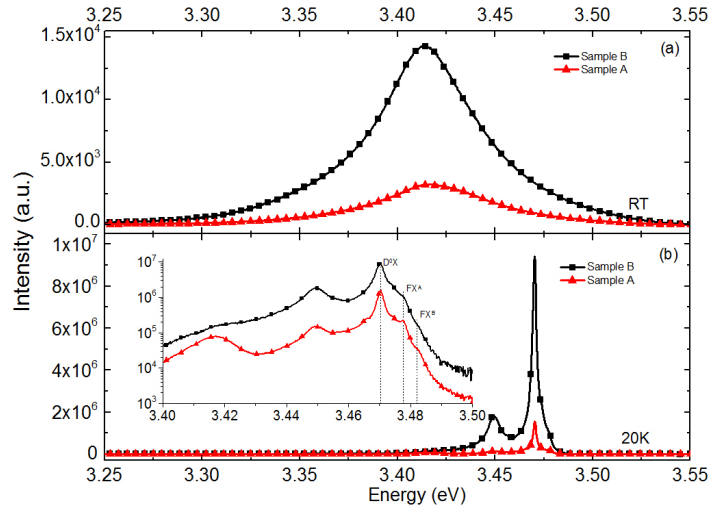


Figure 6.8: Photoluminescence spectra taken (a) at room temperature and (b) at 20K. The inset is the PL spectrum at 20K in the band edge region, showing the different contribution of the defect-emission peak at 3.417 eV in the two samples.

PL studies at room temperature (RT) and at 20 K are presented in Figs. 6.8.a and 6.8.b, respectively. The integrated PL intensity of sample A is 7 times less at 20K and 4 times less at RT than that of sample B, which may indicate a better overall crystalline quality in sample B. The inset of Fig. 6.8.b shows the 20 K PL spectra in logarithmic scale to identify the various emission peaks. The 20 K PL spectra of both samples are dominated by the donor bound exciton (D^0X) emission at 3.470 eV that corresponds to relaxed GaN crystals. The FWHM of this peak was measured at 2.3 meV for sample A and at 2.9 meV for sample B, values consistent with a good crystalline quality of the GaN NWs for both samples. Another strong emission in the 20K PL spectra is located near 3.45eV. Although commonly observed in GaN NW structures, its origins are still unclear [17, 22]. It has been correlated with the two-electron satellite of the D^0X emission [8],

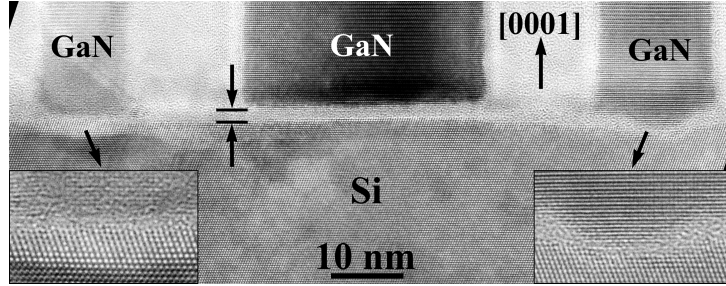


Figure 6.9: Cross-sectional HRTEM image of sample A illustrating three adjacent NWs along the $[11\bar{2}0]_{\text{GaN}}//[\bar{1}10]_{\text{Si}}$ zone axes. Roughening of the Si (111) surface and formation of a thin amorphous Si_xN_y layer are due to unintentional nitridation. The central NW grown on a 1.3 nm thick amorphous Si_xN_y has a larger diameter, due to the absence of crystalline constraints with Si, compared to the other two thin NWs that are partially or fully in contact with the Si substrate, as shown in the insets depicting the corresponding GaN/Si interfaces.

surface Ga-vacancies [12] and Ga interstitials [4]. A relatively weak peak is also observed for both samples at 3.417 eV. Peaks in the range of 3.41-3.42 eV were found to originate either from NW regions close to the interface with the Si substrate [4, 12], or from excitons bound to I1 basal stacking faults [8, 18]. The identified peak appears very clearly in the PL spectra of sample A (inset of Fig. 6.8.b), while it is visible only as a shoulder in sample B. The increased intensity of this defect-emission in sample A indicates a lower crystalline quality compared to sample B, in agreement with the integrated PL intensity result.

6.4 Discussion of results

A significant difference in the GaN/Si interfacial structure of the two samples was observed. An irregular and inhomogeneous interface was formed in the case of sample A, corresponding to direct growth of GaN on bare Si (111) surface. This is attributed to the inhomogeneous exposure of the Si surface to N atoms, as it is covered by three-dimensional GaN islands that nucleate simultaneously with the nitridation of the Si surface [5, 6, 23] and mask the corresponding Si areas from the incident N beam. The Si nitridation is favoured by the extreme N-rich growth conditions (N/Ga flux ratio equal to 5) and the strong Si-N bonds of 4.5 eV [20, 23] and will involve significant migration of Si atoms [3, 10, 19, 21]. The result is a rough Si surface with

mounts, steps and pits, which is partly covered by an amorphous Si_xN_y layer with non-uniform thickness. These large variations at the substrate surface result in non-uniform nucleation and growth of GaN NWs, broadening the distribution of heights and increasing the misalignment of the NWs [3, 5, 11].

The intentional nitridation of the Si (111) substrate, in the case of sample B, resulted to a smooth surface covered homogenously by a 1.52 ± 0.11 nm thick amorphous Si_xN_y layer. The homogenous nitridation of the Si surface may also smooth out any initial roughness present on the thermally cleaned Si (111) surface. In this case, GaN NWs nucleate and grow on a flat and uniform substrate surface, resulting in a narrowed distribution of heights and an improved alignment of the NWs, in agreement with the presented FE-SEM and XRD results of Figs. 6.1, 6.2, and 6.3.

An interesting result is that the GaN NWs exhibited a dominant epitaxial relationship with respect to the Si crystal lattice, when a homogeneous amorphous Si_xN_y layer covered the entire interface (sample B), compared to sample A, where parts of the GaN/Si interface were crystalline. The six-fold symmetry observed in the XRD ϕ -scans for the (11.4) planes, of Fig. 6.4, would not be visible without a specific alignment of the GaN and Si lattices. The comparison of intensities and FWHM values in Fig. 6.4, suggests a superior alignment of NWs, concerning twist angle variations, in the case of sample B. Common SAED patterns of the GaN and Si crystals, revealed the established epitaxial relationship of $(0001)_{\text{GaN}} // (1\bar{1}1)_{\text{Si}}$, $[11\bar{2}0]_{\text{GaN}} // [1\bar{1}0]_{\text{Si}}$. The epitaxial growth of GaN NWs on an intermediate amorphous Si_xN_y layer has been correlated to a very small thickness of the Si_xN_y layer during GaN nucleation, or the presence of crystalline structure in Si_xN_y [2, 24].

Another finding in this work is the dependence of GaN NW diameter on the presence of crystalline or amorphous interface with the Si substrate. According to FE-SEM, the average NW diameter was 25 nm for sample A and 40 nm for sample B. The narrower average diameter in sample A is attributed to the partially crystalline GaN/Si interfaces that impose strain in the NWs, while the strain is negligible for NW growth on amorphous Si_xN_y . This has been described as the effect of epitaxial constraints on the growth [6] and is also supported by the HRTEM image of Fig. 6.9, which illustrates three adjacent GaN NWs in sample A, grown on either amorphous Si_xN_y or crystalline Si. A much smaller diameter appears for the two NWs having a structural interface with Si, while the thicker one in the middle is grown on amorphous Si_xN_y .

The absence of Si_xN_y at the interface is related to the nucleation of epitaxial wurtzite GaN islands directly on the Si (111) substrate surface, with the epitaxial relationship $(0001)\text{GaN} // (111)\text{Si}$. This is different from the work of Borysiuk et al [1] where epitaxial zincblende (001) GaN islands were

nucleated on (001) Si. In that case, wurtzite GaN nanowires evolved from the inclined (111)Ga facets of the cubic GaN (001) islands, and the nanowire c-axis was parallel to the Si [111] direction and the cubic GaN [111] direction.

The incubation time, growth, and size of a stable GaN nucleus is an interplay and compromise between bulk GaN energies, free surface and interface energies, strain energy imposed by epitaxial constraints as well as the impinging fluxes, adatom densities and binding energies of the Ga and N species, i.e. the chemical potentials of the latter. Although in the present work we have little information regarding the actual shape and size of the initial GaN nuclei, the presence of the amorphous Si_xN_y layer indicates that no epitaxial constraints are imposed during NWs growth on these layers. Thus, the strain energy contributions to the free energy of the initial nuclei are negligible. The epitaxial constraints and defective crystalline interfaces in sample A constitute an energetic driving force for smaller interfacial areas and hence smaller NW diameters in sample A. This is not contradictory with the report of Fernandez-Garrido et al [9] of a self-regulated mechanism for the dependence of GaN NW diameter on the used Ga flux (for constant N flux). In their paper [9], GaN growth was continued with different Ga fluxes on pre-existing identical GaN NWs of height 1.5 μm and diameter 86 nm. In the present work, the GaN NWs have average height of 430-440nm for both samples whilst the diameter is 25 nm and 40 nm for samples A and B, respectively. These NWs are at a much earlier stage of growth compared to those of Fernandez-Garrido et al [9] and have been nucleated on different structure Si surfaces. It is thus reasonable to conclude that the observed difference of the GaN NW diameter, between 25 and 40 nm, is indicative of the effects of interfacial structure and strain on the nucleation and growth of GaN NWs.

The KOH polarity tests indicate that GaN NWs nucleating on an amorphous Si_xN_y layer have N-face polarity. However, NWs grown directly on bare Si may contain few Ga-face NWs, in agreement with a previous report [36]. This indicates that certain site(s) of the irregular substrate surface, on which GaN NWs nucleated on sample A, may favour the Ga-face polarity. Thus a controllable way to grow N-face NWs is by intentional nitridation pre-treatment of the Si (111) substrate.

Finally, the better PL properties of sample B could not be attributed to any observed differences in the presence of extended defects (not observed) in the NWs. However, the overall characterization results reveal a correlation of the inferior PL properties (lower integrated intensity, more evident defect emission at 3.417 eV) of sample A with the irregular structure at the GaN/Si interface, which should result to a higher content of electrically active defects in the overgrown NWs. The peak at 3.417eV that is clearly

evident in the 20K PL spectrum of sample A (Fig. 6.8) can originate both from NW regions close to the GaN/Si interface [4, 12] and from the top part of the NWs [8, 18]. In the latter case, emission in the region of 3.42 eV has been attributed to excitons bound to I1 type basal stacking faults that result from the coalescence of different NWs. The irregular structure at the GaN/Si interface increases the misalignment of the GaN NWs and thus will increase their coalescence probability.

6.5 Conclusions

A systematic study of GaN NWs grown either directly on a bare Si (111) substrate or after Si (111) nitridation, has been presented. HRTEM and PL experiments confirmed the high crystalline quality of all NWs. Comparison between the two growth cases allowed for a clear identification of the cause of differences in the alignment and dimensions of the NWs. Silicon nitridation at 760°C for 20 min creates a smooth and homogenous Si_xN_y substrate surface for uniform GaN NW nucleation. On the contrary, direct GaN growth on Si results in a rough and inhomogeneous substrate surface, due to the unintentional nitridation, providing either amorphous or crystalline nucleation sites for the GaN NWs. The presence of the amorphous Si_xN_y allows GaN NW nucleation and growth with negligible strain energy from epitaxial constraints, resulting in larger NW diameters compared to growth on bare Si (111). Furthermore, the relatively flat and uniform Si_xN_y surface permitted an improved alignment of the NWs and a narrower distribution of their heights. The GaN NWs exhibited a dominant epitaxial relationship relative to the Si lattice, which may indicate the presence of ordered regions, at the atomic scale, in the Si_xN_y layer that can influence GaN nucleation. The N-face polarity was detected for GaN NWs nucleating on an amorphous Si_xN_y layer. Finally, the irregular structure at the GaN/Si interface resulted in a higher content of electrically active defects in the overgrown NWs.

Overall, the presented results contribute to a better understanding of the effects of Si nitridation on the spontaneous growth and properties of GaN NWs. They also suggest that a Si (111) nitridation pre-treatment improves the regularity of the spontaneous growth and the properties of the GaN NWs.

Bibliography

- [1] BORYSIUK, J., ZYTKIEWICZ, Z. R., SOBANSKA, M., WIERZBICKA, A., KLOSEK, K., KORONA, K. P., PERKOWSKA, P. S., AND RESZKA, A. "Growth by molecular beam epitaxy and properties of inclined GaN nanowires on Si(001) substrate". *Nanotechnology* 25 (2014), 135610.
- [2] CALLEJA, E., RISTIC, J., FERNANDEZ-GARRIDO, S., CERUTTI, L., SANCHEZ-GARCIA, M. A., GRANDAL, J., A.TRAMPERT, U.JAHN, G.SANCHEZ, A.GRIOL, AND B.SANCHEZ. "Growth, morphology, and structural properties of group-III-nitride nanocolumns and nanodisks". *Phys. Stat. Sol. (b)* 244 (2007), 2816.
- [3] CALLEJA, E., RISTIC, J., FERNANDEZ-GARRIDO, S., CERUTTI, L., SANCHEZ-GARCIA, M. A., GRANDAL, J., TRAMPERT, A., JAHN, U., SANCHEZ, G., GRIOL, A., AND SANCHEZ, B. "Growth, morphology, and structural properties of group-III-nitride nanocolumns and nanodisks". *Phys. Stat. Sol. (b)* 244 (2007), 2816.
- [4] CALLEJA, E., SANCHEZ-GARCIA, M. A., SANCHEZ, F. J., CALLE, F., NARANJO, F. B., MUNOZ, E., JAHN, U., AND PLOOG, K. "Luminescence properties and defects in GaN nanocolumns grown by molecular beam epitaxy". *Phys. Rev. B* 62 (2000), 16826.
- [5] CHEZE, C., GEELHAAR, L., TRAMPERT, A., AND RIECHERT, H. "In situ investigation of self-induced GaN nanowire nucleation on Si". *Appl. Phys. Lett.* 97 (2010), 043101.
- [6] CONSONNI, V. "Self-induced growth of GaN nanowires by molecular beam epitaxy: A critical review of the formation mechanisms". *Phys. Status Solidi RRL* 7 (2013), 699.
- [7] CONSONNI, V., HANKE, M., KNELANGEN, M., GEELHAAR, L., TRAMPERT, A., AND RIECHERT, H. "Nucleation mechanisms of self-induced GaN nanowires grown on an amorphous interlayer". *Phys. Rev. B* 83 (2011), 035310.

- [8] CORFDIR, P., HAUSWALD, C., ZETTLER, J. K., FLISSIKOWSKI, T., LAHNEMANN, J., FERNANDEZ-GARRIDO, S., GEELHAAR, L., GRAHN, H. T., AND BRANDT, O. "Stacking faults as quantum wells in nanowires: Density of states, oscillator strength, and radiative efficiency". *Phys. Rev. B* 90 (2014), 195309.
- [9] FERNANDEZ-GARRIDO, S., KAGANER, V. M., SABELFELD, K. K., GOTSCHKE, T., GRANDAL, J., CALLEJA, E., GEELHAAR, L., AND O.BRANDT. "Self-Regulated Radius of Spontaneously Formed GaN Nanowires in Molecular Beam Epitaxy". *Nano Lett.* 13 (2013), 3274.
- [10] FERNANDEZ-GARRIDO, S., ZETTLER, J. K., GEELHAAR, L., AND BRANDT, O. "Monitoring the Formation of Nanowires by Line-of-Sight Quadrupole Mass Spectrometry: A Comprehensive Description of the Temporal Evolution of GaN Nanowire Ensembles". *Nano Lett.* 15 (2015), 1930.
- [11] FURTMAYR, F., VIELEMEYER, M., STUTZMANN, M., ARBIOL, J., ESTRADE, S., PEIRO, F., MORANTE, J. R., AND EICKHOFF, M. "Nucleation and growth of GaN nanorods on Si (111) surfaces by plasma-assisted molecular beam epitaxy - The influence of Si- and Mg-doping". *J. Appl. Phys.* 104 (2008), 034309.
- [12] FURTMAYR, F., VIELEMEYER, M., STUTZMANN, M., LAUFER, A., MEYER, B. K., AND EICKHOFF, M. "Optical properties of Si- and Mg-doped gallium nitride nanowires grown by plasma-assisted molecular beam epitaxy". *Appl Phys* 104 (2008), 074309.
- [13] GEELHAAR, L., CHEZE, C., JENICHEN, B., BRANDT, O., PFULLER, C., MUNCH, S., ROTHEMUND, R., REITZENSTEIN, S., FORCHEL, A., KEHAGIAS, T., KOMNINO, P., DIMITRAKOPOULOS, G. P., KARAKOSTAS, T., LARI, L., CHALKER, P. R., GASS, M. H., AND RIECHERT, H. "Properties of GaN Nanowires Grown by Molecular Beam Epitaxy". *IEEE Journal. Sel. Top. quantum Electron.* 17 (2011), 878.
- [14] HESTROFFER, K., AND DAUDIN, B. "A RHEED investigation of self-assembled GaN nanowire nucleation dynamics on bare Si and on Si covered with a thin AlN buffer layer". *Phys. Status Solidi RRL* 7 (2013), 835.
- [15] HESTROFFER, K., LECLERE, C., BOUGEROL, C., RENEVIER, H., AND DAUDIN, B. "Polarity of GaN nanowires grown by plasma-assisted molecular beam epitaxy on Si(111)". *Phys. Rev. B* 84 (2011), 245302.

- [16] HESTROFFER, K., LECLERE, C., CANTELLI, V., BOUGEROL, C., RENEVIER, H., AND B.DAUDIN. "In situ study of self-assembled GaN nanowires nucleation on Si(111) by plasma-assisted molecular beam epitaxy". *Appl. Phys. Lett.* 100 (2012), 212107.
- [17] JAYAPRAKASH, R., AJAGUNNA, D., GERMANIS, S., ANDROULIDAKI, M., TSAGARAKI, K., GEORGAKILAS, A., AND PELEKANOS, N. T. "Extraction of absorption coefficients from as-grown GaN nanowires on opaque substrates using all-optical method". *Opt. Express* 22 (2014), 19555.
- [18] KORONA, K. P., RESZKA, A., SOBANSKA, M., PERKOWSKA, P. S., WYSMOLEK, A., KLOSEK, K., AND ZYTKIEWICZ, Z. R. "Dynamics of stacking faults luminescence in GaN/Si nanowires". *J. Lumin.* 155 (2014), 293.
- [19] KUMAR, P., TUTEJA, M., KESARIA, M., WAGHMARE, U. V., AND SHIVAPRASAD, S. M. "Superstructure of self-aligned hexagonal GaN nanorods formed on nitrided Si(111) surface". *Appl. Phys. Lett.* 101 (2012), 131605.
- [20] LARGEAU, L., GALOPIN, E., GOGNEAU, N., TRAVERS, L., GLAS, F., AND HARMAND, J. C. "N-Polar GaN Nanowires Seeded by Al Droplets on Si(111)". *Cryst. Growth Des.* 12 (2012), 2724.
- [21] SABELFELD, K. K., KAGANER, V. M., LIMBACH, F., DOGAN, P., BRANDT, O., GEELHAAR, L., AND RIECHERT, H. "Height self-equilibration during the growth of dense nanowire ensembles: Order emerging from disorder". *Appl. Phys. Lett.* 103 (2013), 133105.
- [22] SAM-GIAO, D., MATA, R., TOURBOT, G., RENARD, J., WYSMOLEK, A., DAUDIN, B., AND GAYRAL, B. "Fine optical spectroscopy of the 3.45eV emission line in GaN nanowires". *J. Appl. Phys.* 113 (2013), 043102.
- [23] STOICA, T., SUTTER, E., MEIJERS, R. J., DEBNATH, R. K., CALARCO, R., LUTH, H., AND GRUTZMACHER, D. "Interface and Wetting Layer Effect on the Catalyst-Free Nucleation and Growth of GaN Nanowires". *Small* 4 (2008), 751.
- [24] WIERZBICKA, A., ZYTKIEWICZ, Z. R., KRET, S., BORYSIUK, J., DLUZEWski, P., SOBANSKA, M., KLOSEK, K., RESZKA, A.,

TCHUTCHULASHVILI, G., CABAJ, A., AND LUSAKOWSKA, E. "Influence of substrate nitridation temperature on epitaxial alignment of GaN nanowires to Si(111) substrate". *Nanotechnology* 24 (2013), 035703.

Effects of ultrathin AlN prelayer on GaN nanowires

7.1 Introduction

A typical observation in PAMBE growth of GaN NWs on Si (111) substrates concerns the presence of amorphous Si_xN_y interlayer at the GaN NW/Si interface, resulting from unintentional nitridation of the Si surface [5, 11, 14, 17, 20]. The intentional Si (111) nitridation before GaN deposition has been found to improve the alignment of the GaN NWs and to narrow the distribution of their heights, as a result of improved homogeneity of the Si_xN_y interfacial layer [11]. Alternatively, the initial growth of an AlN prelayer on Si (111) has been used to avoid nitridation of the Si surface and formation of amorphous Si_xN_y , thus creating a crystalline interface [5, 24, 27]. The AlN prelayer accelerates the nucleation of GaN NWs and improves their alignment [5, 24, 27]. However, this interfacial AlN layer is also a barrier for carrier transport through the interface in NW devices and it is thus necessary to minimize its thickness.

A good physical understanding of the GaN NWs nucleation with the assistance of AlN prelayers on Si, and the optimization of the growth and properties of GaN NWs, requires a systematic comparison of NW growth processes with different amounts of deposited AlN. Although PAMBE enables control of deposition thickness at the scale of an atomic layer, there has been no investigation of the effects of AlN prelayer thicknesses less than 1.8 nm [16, 29] concerning GaN NW growth. This chapter paper provides missing quantitative information for the dependence of the morphological and structural characteristics of GaN NWs on the amount of deposited AlN, for nominal deposition thickness in the range from 0 to 1.5 nm. In addition, the used MBE system setup allows the simultaneous incidence of N and Al atoms on the surface, avoiding the common practice of depositing an Al

prelayer [6, 16, 17, 22] on the Si surface.

The growth and properties of the GaN NWs have been analyzed by Reflection high energy electron diffraction (RHEED), field-emission scanning electron microscopy (FE-SEM), X-ray diffraction (XRD) and high-resolution transmission electron microscopy (HRTEM). It is shown that even depositing a fraction of an AlN monolayer could enhance GaN NW nucleation and crystallographic alignment, although amorphous Si_xN_y is still formed at the GaN/Si interface. An AlN prelayer of 1.5 nm nominal thickness, prevents Si surface nitridation and improves the homogeneity of the nucleation of GaN NWs, with negligible parasitic GaN formation between them. The misfit strain of AlN on Si (111) is immediately relaxed, whilst formation of $\beta\text{-Si}_3\text{N}_4$ is evident for a short time before AlN nucleation.

7.2 Experimental Details

In some PAMBE growth chambers, nitridation of the Si (111) substrate surface is evident, by modification of the 7×7 Si (111) reconstruction, as soon as the RF source nitrogen plasma is turned on [16, 17, 29]. The deposition of Al prior to the ignition of the nitrogen plasma is commonly used [6, 16, 17, 22] for protecting the Si (111) surface from nitridation, which however may also result to formation of the Al-Si γ phase [23]. Our PAMBE growth chamber is equipped with a main shutter that limits the unintentional exposure of the Si substrate to active nitrogen species, and thus allows the simultaneous exposure of the surface to group-III and N atoms.

Several GaN NW samples were grown and the first growth step comprised deposition of an AlN prelayer on the atomically clean Si (111) surface, with AlN nominal thickness of 0.22 ± 0.04 nm or 0.38 ± 0.06 nm, or 0.54 ± 0.07 nm or 1.5 ± 0.20 nm. The substrate temperature was ~ 760 °C, the N/Al flux ratio was 1.6 and the AlN growth rate was 195 nm/h. The AlN/Si structures were then annealed under nitrogen flux for 20 min to reach a stable structure and avoid potential structural modification under the excessive nitrogen flux impinging on the surface during the subsequent N-rich growth of GaN NWs. Then GaN NWs were grown for 3h, under N-rich conditions with N/Ga flux ratio equal to 5, and a Ga flux equivalent to GaN growth rate of 84.6 nm/h. In order to confirm the reproducibility of results for AlN prelayer thickness of 0.38 and 0.54nm, two GaN NW samples were grown for each AlN thickness, both giving identical morphological results of the GaN NWs. For the case of 1.5nm AlN, three samples were grown that also gave identical morphological results.

A reference sample (0 nm AlN) was grown by omitting the first growth

step of AlN prelayer deposition. In this case, the 3h GaN NWs growth followed the 20 min annealing under nitrogen flux (nitridation) of the atomically clean Si (111) surface.

All the GaN NW samples were grown using substrate rotation to optimize their uniformity, so that cross-correlation of results by different analytical techniques is meaningful. An additional experiment of AlN growth on Si (111), aimed to provide further insight into the physical process of AlN nucleation, was carried out without substrate rotation, for continuous recording by a charge-coupled device (CCD) camera of the RHEED pattern evolution along the $\langle 10\bar{1}0 \rangle_{AlN} / \langle \bar{2}11 \rangle_{Si}$ azimuth.

7.3 Experimental Results

7.3.1 RHEED observations for different samples

The 20 min nitridation of the clean Si (111) surface, which exhibited a 7×7 reconstruction, resulted to an amorphous Si_xN_y layer, evident by a diffused RHEED pattern without the appearance of any spots or streaks. This RHEED observation remained constant up to 15 min of GaN deposition on the nitridated Si (111) surface, indicating a 15 min delay for GaN nucleation. A typical pattern of spots elongated along arcs [7, 13] appeared after the 15th minute, suggesting the nucleation of three-dimensional (3D) GaN islands on the amorphous Si_xN_y/Si surface with a substantial misorientation of their crystals. The RHEED pattern was changing with rotation according to the azimuth of incidence of the RHEED electron beam ($\langle \bar{2}11 \rangle$ or $\langle 0\bar{1}1 \rangle$, i.e. every 30°) suggesting a twist coherency of the nucleated GaN crystals. This was confirmed by XRD analysis of the finally grown GaN NWs that has been presented in chapter 6 [11], and is also in agreement with the work of Wierzbicka et al [28].

For all the samples that had an AlN prelayer deposited on Si, at the end of the 20 min annealing of AlN under active nitrogen flux a typical 1×1 RHEED pattern, corresponding to the AlN (0001) surface was observed. This indicates the epitaxial growth of AlN on the Si surface, but the RHEED pattern could result either by an AlN layer that fully covers the substrate, or a coexistence of crystalline AlN islands with amorphous Si_xN_y regions at the surface. After GaN deposition, spotty RHEED patterns started appearing with a time delay depending on the AlN prelayer thickness. The spots for 0.22, 0.38, 0.54 and 1.5 nm thicknesses started appearing at 12.5 ± 1.5 , 12.5 ± 2.5 , 4 ± 1 min and less than 1 min respectively.

A comparison of the RHEED patterns along the $\langle 11\bar{2}0 \rangle_{AlN}$ azimuth,

after 5 min of GaN deposition is provided in Fig. 7.1 for the GaN NW samples grown on substrates with different AlN prelayer thickness (0.22 nm, 0.38 nm, 0.54 nm and 1.5 nm). In the case of samples with AlN prelayer nominal thickness of 0.22 nm and 0.38 nm, there were no GaN RHEED spots visible after 5 min, suggesting that there has been no nucleation of 3D GaN islands within that time (Figs. 7.1(a), (b)). For these samples (0.22 nm and 0.38 nm AlN prelayer thickness), GaN RHEED spots elongated along arcs started appearing at a time (12.5 min) close to that observed for GaN deposition on the nitridated Si surface (without any AlN prelayer). However, at the end of the 3h GaN NW growth, the RHEED pattern consisted of circular spots, without any elongation along arcs.

The RHEED pattern at the 5th minute of GaN deposition on the sample with AlN nominal prelayer thickness of 0.54 nm is shown in Fig. 7.1.c. It consists of both, streaks and spots, suggesting the substantial nucleation of GaN islands before their shape transformation to NWs [7, 18]. For the case of 1.5 nm AlN prelayer, no streaks are visible in the RHEED pattern taken after 5 min of GaN deposition (Fig 7.1.d) suggesting that the growth had proceeded to the final stage of formation and growth of GaN NWs.

7.3.2 NWs morphology and structure

FE-SEM revealed the strong dependence of the morphological characteristics of the GaN NWs on the AlN prelayer thickness, for the range of ultrathin AlN thicknesses studied in this paper. A major increase in NW height was observed with increasing the AlN prelayer thickness from 0 to 0.28 nm, then to 0.38 nm and then to 0.54 nm, as shown in the cross-sectional FE-SEM micrographs of Fig. 7.2. In the case of 0.54 nm of AlN prelayer, there was a lot of parasitic GaN growth in the intermediate regions between the formed GaN NWs, as can be seen in Fig. 7.2.d. On the contrary, in the case of GaN NW growth on 1.5 nm AlN, the parasitic GaN growth was significantly reduced and there was a better height homogeneity (Fig. 7.2.e).

For quantification of the morphological characteristics of the GaN NWs that were grown for 3h, their height, diameter and density were measured from FE-SEM micrographs of a cross-section and the top surface of each sample at vertical view and 30° tilted view. The determined values have been plotted versus AlN prelayer thickness in Figs. 3(a)-(c). The average GaN NW height (Fig. 7.3.a) increased from 430 nm, for GaN deposition on the nitridated Si surface (Fig. 7.2.(a)) to 850 nm for GaN deposition on 0.54 nm AlN prelayer (Fig. 7.2.d. For the case of 1.5 nm AlN prelayer (Fig. 7.2.e), the average GaN NW height was the same as for the case of 0.54 nm, AlN (Fig. 7.2.d) suggesting a saturation of the GaN NW height for the growth

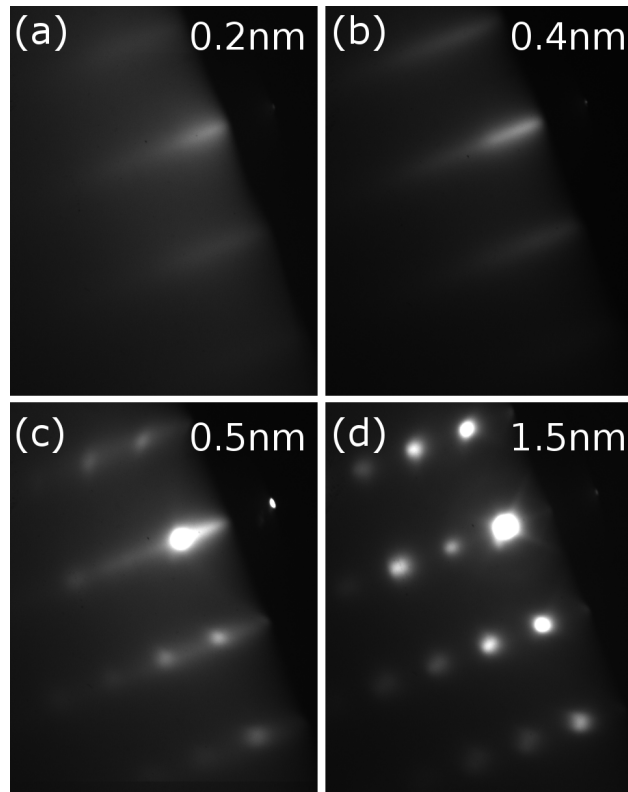


Figure 7.1: RHEED patterns for electron beam incidence along the $\langle 11\bar{2}0 \rangle_{\text{GaN}}$ azimuth after 5 minutes of GaN deposition, for samples with AlN prelayer thickness of (a) 0.2, (b) 0.4, (c) 0.5 and (d) 1.5 nm.

conditions used.

The average NW diameter (Fig. 7.3.b) decreased from ~ 40 nm to ~ 25 nm with increasing the AlN prelayer thickness from 0 to 0.54 nm respectively. Interestingly, in the case of samples with 1.5 nm AlN, the GaN NW diameter increased to 35 nm. The GaN NW density (Fig. 7.3.c) decreased from $\sim 2 \times 10^{10} \text{ cm}^{-2}$, in the case of no AlN prelayer, to $\sim 6 \times 10^9 \text{ cm}^{-2}$ for 0.54 nm AlN prelayer. Again, the GaN NW density of samples with 1.5 nm AlN prelayer thickness did not follow the decreasing trend of the samples with thinner AlN prelayers, but was increased to $1 \times 10^{10} \text{ cm}^{-2}$.

The crystallographic alignment of the GaN NWs, estimated from XRD measurements, also exhibited a monotonic dependence on AlN prelayer thickness for samples with AlN thickness up to 0.54 nm. Figure 7.3.d shows the full width at half maximum (FWHM) of XRD ω -scans around the (0002) reflection. The XRD FWHM decreases from 3.4° , in the case of GaN NWs grown without any AlN prelayer, to 0.96° in the case of the two GaN NW

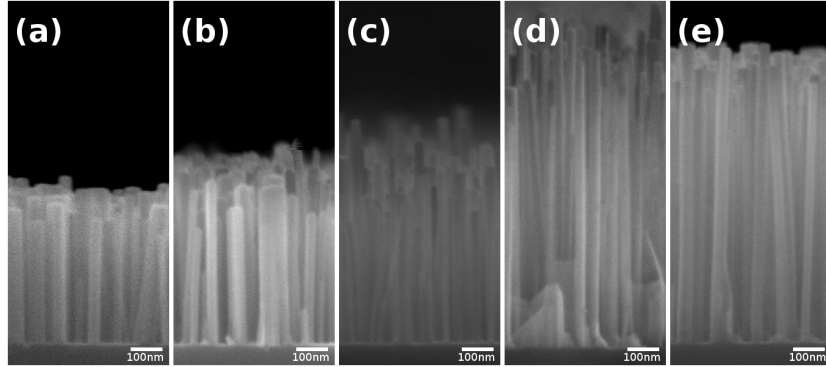


Figure 7.2: Cross-sectional FE-SEM micrographs of GaN NWs grown on: (a) nitridated Si (111) surface or after depositing on Si (111) an AlN prelayer with nominal thickness (b) 0.22nm, (c) 0.38nm, (d) 0.54nm and (e) 1.5nm.

samples with 0.54 nm of AlN. One of the two samples with 0.4 nm of AlN prelayer thickness, had an XRD FWHM value of 3.35° , that does not follow the decreasing trend, but this is attributed to damage of the surface of the specific sample that could affected the XRD measurements. The XRD FWHM of the samples with 1.5 nm AlN prelayer exhibited a slight increase compared to the 0.54 nm AlN, being of 1.3° . This XRD FWHM increase might be due to secondary effects in GaN NW growth such as NW coalescence occurring for high NWs [2, 4, 9], or some mechanical instability against bending that is present during the measurement. In the case of 0.54 nm AlN prelayer, which resulted to the same height of GaN NWs, similar GaN NW coalescence may have been limited by the GaN parasitic growth around the NWs that sometimes covers the NWs up to a height of ~ 300 nm, and thus stabilizing their orientation against bending.

HRTEM imaging of the sample with 0.38 nm of AlN prelayer showed the presence of amorphous interfaces between the GaN NWs and the Si substrate (Fig. 7.4). In Fig. 7.4, a HRTEM image of the amorphous GaN NWs/Si interface is depicted, along the $[11-20]_{\text{GaN}}//[110]_{\text{Si}}$ projection direction, while no AlN layer could be identified by HRTEM. We attribute the amorphous material in the nitridation of the Si (111) surface, forming Si_xN_y , although we cannot exclude the presence of Al atoms, in the amorphous region.

Besides wurtzite GaN NWs, sparse crystalline island-like regions of non-polar m-plane GaN were also identified (Fig. 7.5). These GaN crystals either exhibit an amorphous interface with the Si substrate (Fig. 7.5), or in some cases they are in direct contact with it (Fig. 7.6).

In the case of the sample with 1.5 nm of AlN prelayer thickness, a clear crystalline AlN interface between the GaN NWs and the substrate was iden-

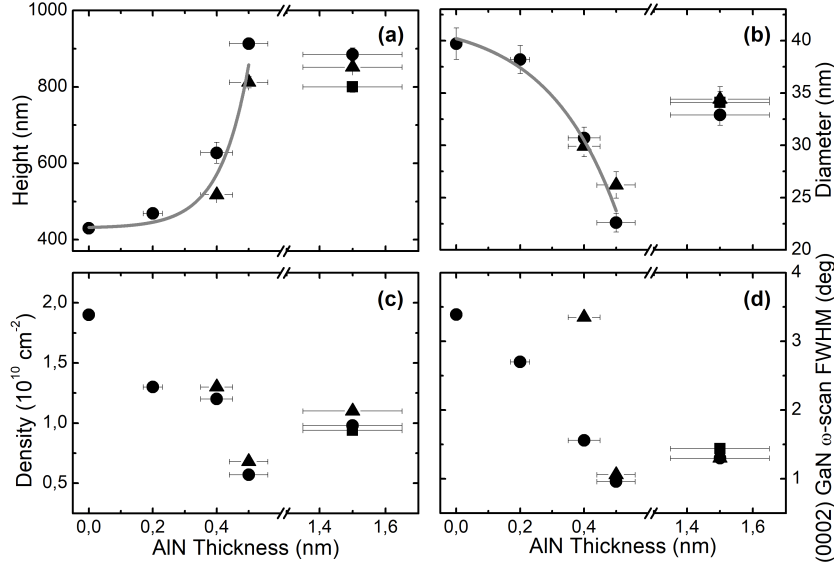


Figure 7.3: (a) Height, (b) diameter, (c) density and (d) (0002) GaN ω -scan FWHM of GaN NWs grown spontaneously on Si (111) with different AlN prelayer thickness.

tified by HRTEM, with no trace of amorphous Si_xN_y (Fig. 7.7). The AlN crystalline layer is continuous but exhibits a considerable surface roughness and resembles a dot-like structure, as shown in the HRTEM image of Fig. 7.7, in agreement with Landre et al [21]. The corresponding geometrical phase analysis (GPA) map of the out-of-plane lattice strain components revealed that both the GaN NW and the AlN prelayer were nearly strain-free (Fig. 7.8). From Fig. 7.8.8(b), we can deduce that the AlN influenced interfacial area is $\sim 2.5\text{nm}$, considerably larger than the nominal AlN thickness. Moreover, small interfacial GaN pyramidal domains forming inversion domain boundaries with the NWs, were also observed growing among them, indicating different polarities between NWs and pyramidal domains. KOH etching tests performed on all the samples revealed that the grown NWs were N-polar suggesting that the pyramidal domains are Ga-polar.

7.3.3 RHEED observations during the first stages of AlN deposition

For a better understanding of the AlN growth on Si (111) surface, it was deemed necessary to make a growth experiment with no substrate rotation, to allow continuous recording of the RHEED pattern while Al and N atoms

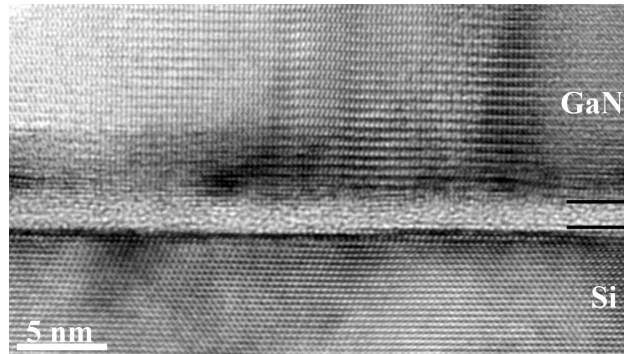


Figure 7.4: (a) HRTEM image of a GaN NW with 0.38 nm AlN prelayer showing the GaN/Si interface, projected along $[11\bar{2}0]_{\text{GaN}}//[110]_{\text{Si}}$ zone axes (z.a.). The amorphous interfacial layer is clearly visible.

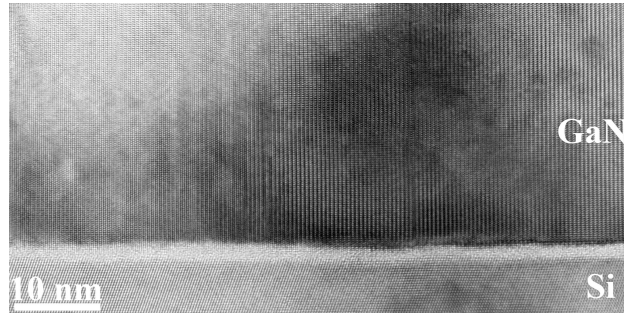


Figure 7.5: HRTEM image of the sample with 0.38 nm AlN prelayer, projected along $[11\bar{2}0]_{\text{GaN}}//[110]_{\text{Si}}$ z.a., illustrating a non polar m -plane GaN crystal sharing an amorphous interface with the Si substrate. Basal plane SFs are also visible in GaN.

were deposited on the surface. The RHEED pattern was recorded along the $[\bar{2}11]_{\text{Si}}/[10\bar{1}0]_{\text{AlN}}$ azimuth. A 7×7 RHEED pattern was visible prior any deposition on the Si surface (Fig. 7.9(a)). As soon as the main shutter was opened, the 7×7 pattern disappeared and a 8×8 pattern (Fig. 7.9(b)) appeared for a few seconds that is attributed to $\beta\text{-Si}_3\text{N}_4$ (0001) [1, 17]. After the disappearance of the 8×8 pattern, the 1×1 pattern of the Si (111) surface started to faint away, while a 1×1 pattern with larger spacings of the streaks, corresponding to the AlN (0001) surface started appearing and prevailed (Fig. 7.9(c)).

The average intensities for the RHEED patterns discussed above (Figs. 7.9(a), (b) and (c)) are depicted in Figs. 7.9(d), (e) and (f), respectively. The intensities were calculated along a selected horizontal rectangular region, marked by gray dashed lines. For the 7×7 reconstruction all the reconstruc-

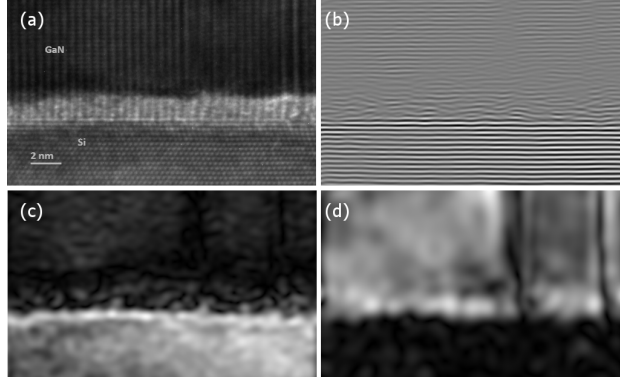


Figure 7.6: a) HRTEM image showing another crystal of m -plane GaN in the sample with 0.38 nm AlN prelayer, where the thin bright contrasted interfacial layer is in focus. It is clear that this area is crystalline, corresponding to the c -planes of GaN. b) Bragg image taken by Fourier filtering of (a), indicating the flat Si surface. c) Fourier filtered image from (a) showing the amplitude of the 111-Si frequency. d) Fourier filtered image from (a) showing the amplitude of the c -GaN frequency.

tion streaks but the 5th one are clearly distinguishable (Fig. 7.9(d)), while for the 8×8 reconstruction, only the 3rd and 5th reconstruction streaks are visible (Fig. 7.9(e)). The lattice constant of AlN $a_{AlN(0001)}$ was estimated by the measured distance of the (01)-order AlN bulk line from the (00) one (a_{01AlN}) in Fig. 7.9(c), and the corresponding distance (a_{01Si}) for the Si (111) surface in Fig. 7.9(b), using the equation :

$$a_{AlN(0001)} = \frac{a_{01Si}}{a_{01AlN}} \times a_{Si(111)} \quad (7.1)$$

where $a_{Si(111)}$ was assumed to have the strain free value of 0.384 nm. This resulted to $a_{AlN(0001)} = 0.308 \pm 0.003$ nm, which translates to a compressive strain value of $\varepsilon_a = -0.0103$ ($a_{AlN(0001)nominal} = 0.3112$ nm). These results indicate that AlN is practically fully relaxed on the Si substrate from the first stages of its growth.

For monitoring the evolution of the 7×7 Si and the 8×8 β -Si₃N₄ reconstructions with time, the intensity of the 4th and 3rd reconstruction streaks, respectively, was extracted from a selected area of the RHEED patterns centered at each streak (vertical black lines in Figs. 7.9(a), (b) respectively). The 3rd streak of the 8×8 reconstruction was chosen due to its higher brightness than the other visible streak of the 8×8 reconstruction (Fig. 7.9(b)). It should be pointed out that the 3rd streak may also correspond to the $8/3 \times 8/3$ reconstruction [1], suggesting the coexistence of both the 8×8 and

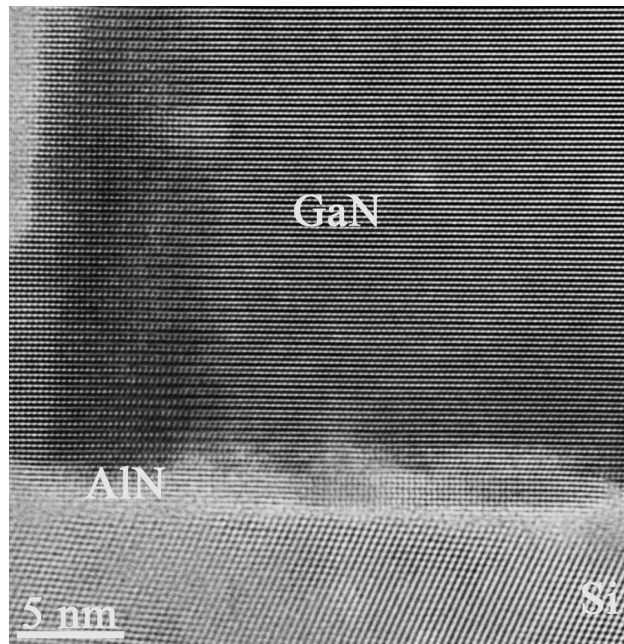


Figure 7.7: HRTEM image of the GaN NWs sample with 1.5 nm AlN prelayer thickness showing GaN NWs/AlN/Si interface, projected along $[11\bar{2}0]_{\text{GaN}}//[110]_{\text{Si}}$ z.a.. No amorphous interfacial layer at the GaN/AlN/Si interface can be detected. The AlN layer presents a dot-like albeit continuous form, where a GaN NW nucleates directly on top of it.

the $8/3 \times 8/3$ reconstructions.

The proximity of the two chosen streaks of the 7×7 and 8×8 reconstruction in the RHEED pattern results to interference of their intensities. In order to monitor the intensity changes of each streak separately, a background region was defined for each streak (vertical rectangles with black dotted lines in Figs. 7.9(a), (b)). The mean intensity in the background region was subtracted from that of the black line. The results of this analysis have been plotted in Fig. 7.10(a)) and show the immediate disappearance of the 7×7 reconstruction (gray line) and the simultaneous appearance of the 8×8 reconstruction (black line) as soon as the main shutter opens and allows the incidence of the N and Al beams on the 7×7 Si (111) surface. The 8×8 reconstruction is observed for almost 2 sec and then disappears.

For tracking the evolution of RHEED from the exposed Si and AlN surface areas on the substrate, the intensity along a thin rectangular region on top of the (01) bulk line of Si (vertical rectangle with black dashed lines in Figs. 7.9(a),(b)) and AlN (vertical rectangle with black dashed line in Fig. 7.9(c)) was recorded, and the results have been plotted in Fig. 7.10(b). The gray

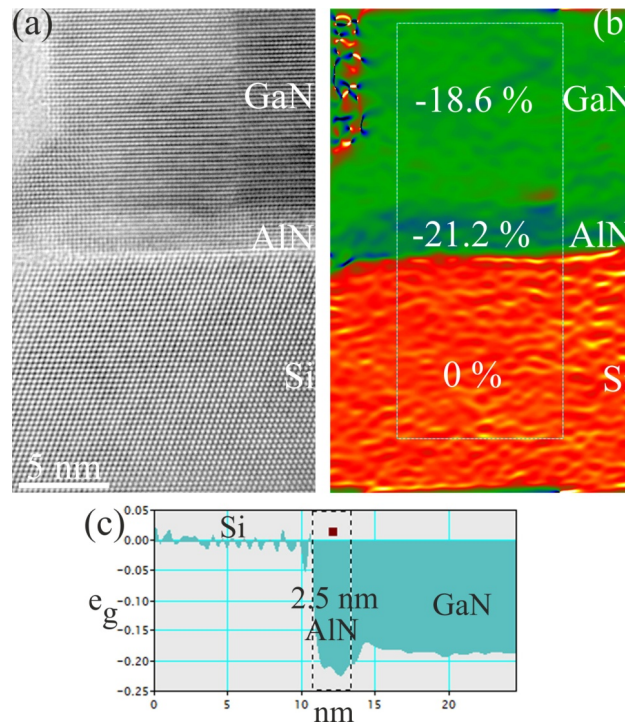


Figure 7.8: (a) HRTEM image of a part of the previous GaN/AlN/Si interface. (b) Corresponding GPA map of the lattice strain component along the growth direction. (c) Corresponding line profile of the lattice strain of the (0002) GaN and AlN planes. The average calculated strain is $-21.2(\pm 0.6)\%$ for AlN and $-18.6(\pm 0.3)\%$ for GaN, implying an almost strain-free configuration.

curve shows the evolution of the intensity of the AlN RHEED streak. It starts appearing at $t=5.5$ sec, which corresponds to 0.3 nm AlN nominal deposition thickness, and reaches full intensity at $t=12.2$ sec, corresponding to 0.66 nm AlN, while the Si streak (black curve in Fig. 10(b)) gradually faints out, and disappears at the same time. It should be pointed out that the GaN NW samples with 0.38 and 0.54 nm AlN (marked with triangles in Fig. 7.10(b)) coincide in the region of high inclination of the AlN intensity, suggesting that the coverage of the surface with AlN rapidly changes in this region and causes the large morphological differences of GaN NWs, as they were observed.

7.4 Discussion

The overall results showed that increasing the nominal thickness of deposited AlN from 0 to 0.22, 0.38 and 0.54 nm, accelerates the nucleation of GaN on the Si (111) surface, and results to significant differences in the density, morphology and height of the grown GaN NWs (Figs. 7.2 7.3). The RHEED observations indicate the increasing presence of crystalline AlN (0001) on the Si substrate surface when the nominal deposition thickness exceeds ~ 0.3 nm (Fig. 7.10(b)). However, HRTEM identified the presence of amorphous GaN NWs/Si interfaces in the investigated sample with 0.38 nm AlN prelayer (Fig. 7.4). The apparent discrepancy between RHEED and HRTEM observations can be resolved if AlN is in the form of distributed microscopic crystalline regions. An amount of deposited AlN equal to 0.38 nm (~ 1.5 ML), is not sufficient to cover the major part of the Si surface due to the 3D growth mechanism of AlN on Si (111). As a result, the surface cannot be protected from the nitridation process and the formation of amorphous Si_xN_y . Such a process could explain the absence of AlN in HRTEM observations.

The increase of crystalline AlN coverage on the Si substrate, could provide sites for heterogeneous GaN nucleation, in the overall amorphized Si surface. This would result in a faster 3D GaN nucleation, that was observed from RHEED. A similar amount of ultrathin AlN, that was not identified by HRTEM, was also used in our previous work [19]. The enhanced nucleation due to such a layer, was adequate to improve the selectivity of the GaN NW arrays by enhancing nucleation within the open windows, but not on the SiO_2 mask used. On the contrary, the use of 1.5 nm of AlN, resulted in a decoupling of the interaction between the mask-window surface, and NWs grew both, in the windows, and on the mask [19].

The shorter duration of the NWs nucleation stage, for increased AlN deposition, implies a longer duration of their elongation stage during the 3h total duration of GaN deposition. Previous works that focused on the changes of GaN NW characteristics with time, found an increase in the NW diameter and height as the NW elongation time increased [4, 10]. According to this, one would expect both the height and diameter of the GaN NWs in our samples to increase with increasing AlN thickness, since it increases the NW elongation time. Although our results concerning the average NW height are in agreement with this (Fig. 7.3), the average NW diameter exhibits the opposite behavior (Fig. 7.3(b)), i.e., it decreases for samples with longer elongation periods. This is because the increase of the NW diameter with time holds true under the assumption that the radial growth during the NW elongation stage is the only factor affecting the NW diameter (i.e., identical

NW nucleation conditions and initial surfaces). However, this is not the case for the samples studied in this work. Another factor that plays a key role in the final NW diameter is the size of the GaN nuclei prior to the final GaN nuclei/NWs transformation (nuclei critical size) [8]. The reduction of the GaN NW average diameter observed (56 % reduced diameter from 0 nm to 0.54 nm of AlN), suggests that, for the samples studied, the GaN nuclei critical size was decreased by increasing the amount of initially deposited AlN. The increase in NW diameter due to the longer elongation stage, was not enough to compensate for the effects of the reduced critical NW nuclei size.

A finding in our previous work [11] was that when GaN NWs nucleate on a partially crystalline Si interface, they result to smaller diameter NWs compared to nucleation on a fully amorphous Si_xN_y layer that does not imply any misfit strain in the overgrown GaN crystal [11]. This is also in agreement with the observed decrease of the GaN NW diameter, with increasing AlN prelayer thickness from 0, to 0.22, 0.38 and 0.54 nm, as shown in Fig. 7.3(b). It is noted that according to the RHEED study, deposition of 0.54 nm AlN has not covered the entire Si (111) surface yet (Fig. 7.10(b)).

The initial GaN NW diameter is also correlated with the average NW height. Debnath et al [9] showed that in the case of spontaneously grown GaN NWs, thinner NWs have a larger axial growth rate for a diffusion induced (DI) growth process. According to this, the smaller initial NW diameter for samples with increased AlN, would result in a larger axial growth rate, thus leading to the higher NWs observed. It should be noted that during the elongation stage, GaN NWs grow through a DI process [25], during which Ga adatoms diffuse towards and impinge on the top surface of the NW. As such, the final height of the NWs, depends on kinetic and geometric factors, such as shadowing effects [10, 26].

The increase of crystalline AlN coverage on the Si substrate facilitates GaN nucleation, and this could be expected to result in a higher density of GaN NWs. However, the measured NW densities exhibit the opposite behavior (Fig. 7.3(c)), the density of GaN NWs decreases with increasing the AlN prelayer thickness. This may be related to coalescence effects and the fact that not all the nucleated GaN islands evolve into GaN NWs, but they also evolve in a parasitic, faceted rough GaN layer. This is indeed in agreement with the HRTEM observations (in the case of the sample with 0.38 nm AlN prelayer) that identified pyramidal domains and with the SEM observations (for the sample with 0.54 nm AlN, Fig. 2(d)), that showed increased parasitic GaN growth. From these we can conclude that an increased number of GaN islands did not evolve into NWs, with increasing the AlN thickness up to 0.54 nm of AlN.

The identification of inversion domain boundaries between GaN NWs and pyramidal domains from HRTEM, in combination with the N-polarity of the GaN NWs (resulting from KOH etching tests) suggests that the parasitic GaN layer is Ga-polar. Such Ga-polar faceted layers have been observed to grow between NWs ([30] and references therein). This would suggest that a mechanism related to the polarity of the AlN crystallites could also be present, affecting the density of the (N-polar) GaN NWs. The presence of both, Al- and N- polar AlN crystallites would be present in the samples studied, as AlN growth on Si (111) substrates has been found to contain domains with both, N- and Al- polarities [3]. Al-polar AlN crystallites would result in Ga-polar nuclei, that would not evolve into NWs [12]. However, a definite conclusion cannot be drawn regarding the effect of polarity, as numerous phenomena have been associated with the AlN polarity. For example, we have found that in PAMBE of AlN on nonpolar substrates with diamond crystal structure, increasing the AlN thickness switches its polarity from Al-face to N-face [15].

The consistent deviation of the results for 1.5 nm AlN prelayer from the clear trend observed for AlN thickness in the range 0-0.54 nm (Fig. 7.3) indicates a substantial difference in the GaN nucleation and NW formation processes, due to the crystalline AlN interfacial layer that completely covers the Si (111) surface (Figs. 7.7, 7.8). On the contrary, GaN nucleation occurs on an amorphous Si_xN_y layer with embedded AlN nuclei when a thinner AlN prelayer (0.22-0.54 nm) is used. The crystalline AlN interfacial layer is expected to provide more homogeneous GaN nucleation, following a shape transformation and a final relaxation process resulting in GaN NWs formation, as it has been described by Consonni et al [8].

Finally, an 8×8 RHEED reconstruction was immediately formed (Fig. 7.9(b)), when Si surface was exposed simultaneously to the N and Al beams. This was attributed to the presence of crystalline $\beta\text{-Si}_3\text{N}_4$, and disappeared after the first 2 seconds (Fig. 7.10(a)). Interestingly, Hestroffer et al [17] also found evidence of such a reconstruction forming momentarily, even in the case when an Al was first used to cover the Si (111) surface.

7.5 Conclusions

This work builds on the existing knowledge concerning the use of AlN prelayer for the spontaneous nucleation and growth of GaN NWs on Si (111) and reveals quantitative insights about the effects of increasing the amount of deposited AlN, with nominal thickness between 0 and 1.5 nm. Significant differences in the nucleation, density and morphological characteristics of

GaN NWs are observed, even for AlN nominal thickness in the range of 0 - 0.5 nm that is not sufficient for full coverage of the Si (111) substrate by a crystalline AlN layer. The deposition of 0.2 – 0.5 nm AlN accelerates the 3D GaN nucleation on Si (111) by providing crystalline AlN nuclei as heterogeneous nucleation sites in the overall amorphized Si surface. This results in an increased height of GaN NWs, significant improvement of their crystallographic alignment and height homogeneity, and a decrease in the NW diameter and density. A full coverage of the Si substrate by crystalline AlN is achieved for 1.5 nm AlN deposition, which suppresses the formation of an amorphous Si_xN_y interlayer and improves the homogeneity of GaN NW nucleation.

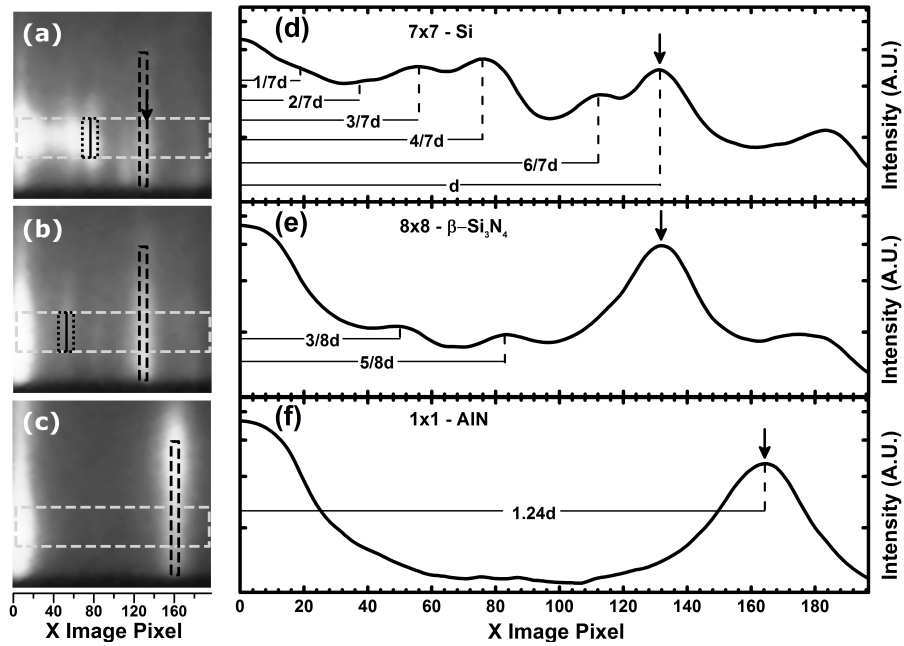


Figure 7.9: RHEED patterns for electron beam incidence along the $\langle 10\bar{1}0 \rangle$ AlN/ $\langle \bar{2}11 \rangle$ Si azimuth showing (a) the 7×7 Si (111) reconstruction, taken 0.4 sec before opening the main shutter, (b) the 8×8 β -Si₃N₄ (0001) reconstruction, taken 1.2 sec after the opening of the main shutter, and (c) the AlN pattern, taken 11.3 sec after the main shutter opening, as they were recorded for the case of AlN deposition. The averaged pixel intensity along the horizontal X-axis, for the rectangular regions depicted in gray dashed line in (a), (b) and (c), are shown in (d), (e) and (f), respectively. The position of the (01)-order RHEED bulk line of Si (111) (d, e) and AlN (0001) (f) are indicated by black arrows, with the X-axis representing the X-pixel distance along the chosen rectangle. The dotted rectangles in (a) and (b) define the background regions, for the 7×7 and 8×8 streak intensity, as defined by the enclosed solid line.

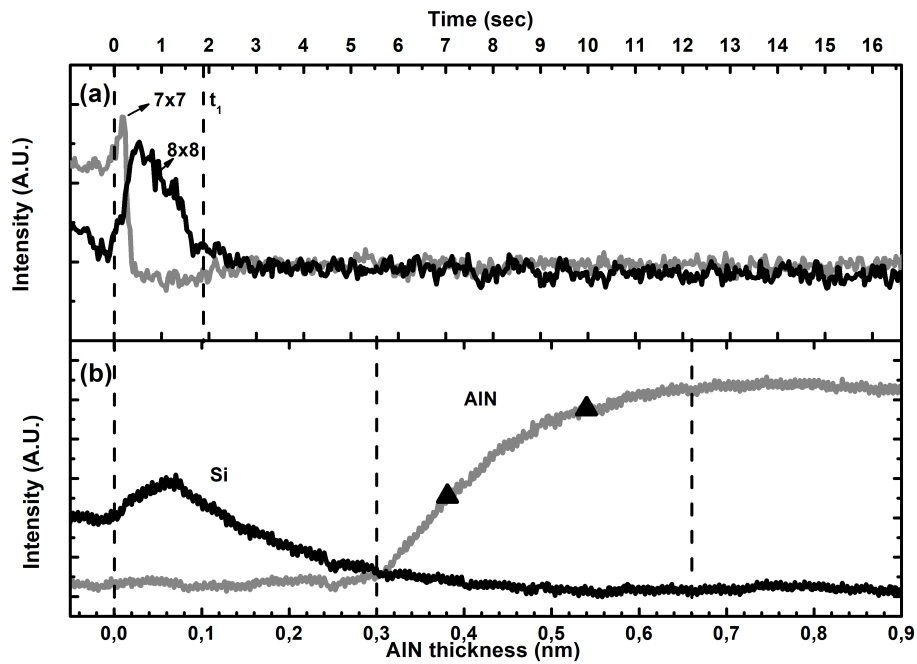


Figure 7.10: Analysis of RHEED observations during the growth of AlN on Si (111) substrate that initially exhibits the 7×7 surface reconstruction: (a) Time evolution of the reconstructions 7×7 Si (111) (gray curve) and 8×8 β - Si_3N_4 (black curve), and (b) Variation of the intensity of the RHEED (01) bulk lines of Si (111) (black curve) and AlN (0002) (gray curve) versus the deposited AlN thickness.

Bibliography

- [1] AHN, H., WU, C.-L., GWO, S., WEI, C. M., AND CHOU, Y. C. "Structure Determination of the $\text{Si}_3\text{N}_4/\text{Si}(111)-(8\times 8)$ Surface: A Combined Study of Kikuchi Electron Holography, Scanning Tunneling Microscopy, and ab initio Calculations". *PRL* 86 (2001), 2001.
- [2] BERTNESS, K. A., ROSHKO, A., SANFORD, N. A., BARKER, J. M., AND DARYDOV, A. V. "Spontaneously grown GaN and AlGaN nanowires". *J. Cryst. Gr.* 287 (2006), 522.
- [3] BRUBAKER, M. D., LEVIN, I., DAVYDOV, A. V., ROURKE, D. M., SANFORD, N. A., BRIGHT, V. M., AND BERTNESS, K. A. "Effect of AlN buffer layer properties on the morphology and polarity of GaN nanowires grown by molecular beam epitaxy". *J. Appl. Phys.* 110 (2011), 053506.
- [4] CALARCO, R., MEIJERS, R. J., DEBNATH, R. K., STOICA, T., SUTTER, E., AND LUTH, H. "Nucleation and Growth of GaN Nanowires on Si(111) Performed by Molecular Beam Epitaxy". *Nano Lett.* 7 (2007), 2248.
- [5] CALLEJA, E., RISTIC, J., FERNANDEZ-GARRIDO, S., CERUTTI, L., SANCHEZ-GARCIA, M. A., GRANDAL, J., TRAMPERT, A., JAHN, U., SANCHEZ, G., GRIOL, A., , AND SANCHEZ, B. "Growth, morphology, and structural properties of group-III-nitride nanocolumns and nanodisks". *Phys. stat. sol. (b)* 244 (2007), 2816.
- [6] CONSONNI, V. "Self-induced growth of GaN nanowires by molecular beam epitaxy: A critical review of the formation mechanisms". *Phys. Status Solidi RRL* 7 (2013), 699.
- [7] CONSONNI, V., HANKE, M., KNELANGEN, M., GEELHAAR, L., TRAMPERT, A., AND RIECHERT, H. "Nucleation mechanisms of self-induced GaN nanowires grown on an amorphous interlayer". *PRB* 83 (2011), 035310.

- [8] CONSONNI, V., KNELANGEN, M., GEELHAAR, L., TRAMPERT, A., AND RIECHERT, H. "Nucleation mechanisms of epitaxial GaN nanowires: Origin of their self-induced formation and initial radius". *PRB* 81 (2010), 085310.
- [9] DEBNATH, R. K., R, M., RICHTER, T., STOICA, T., CALARCO, R., AND LUTH, H. "Mechanism of molecular beam epitaxy growth of GaN nanowires". *Appl. Phys. Lett.* 90 (2007), 123117.
- [10] DUBROVSKII, V. G., CONSONNI, V., GEELHAAR, L., TRAMPERT, A., AND RIECHERT, H. "Scaling growth kinetics of self-induced GaN nanowires". *Appl. Phys. Lett.* 100 (2012), 153101.
- [11] EFTYCHIS, S., KRUSE, J., KOUKOULA, T., KEHAGIAS, T., KOMNINO, P., ADIKIMENAKIS, A., TSAGARAKI, K., ANDROULIDAKI, M., TZANETAKIS, P., ILIOPOULOS, E., AND GEORGAKILAS, A. "Understanding the effects of Si (111) nitridation on the spontaneous growth and properties of GaN nanowires". *J. cryst. Gr.* 442 (2016), 8.
- [12] FERNANDEZ-GARRIDO, S., KONG, X., GOTSCHKE, T., CALARCO, R., GEELHAAR, L., TRAMPERT, A., AND BRANDT, O. "Spontaneous Nucleation and Growth of GaN Nanowires: The Fundamental Role of Crystal Polarity". *Nano Lett.* 12 (2012), 6119.
- [13] FERNANDEZ-GARRIDO, S., ZETTLER, J., GEELHAAR, L., AND BRANDT, O. "Monitoring the Formation of Nanowires by Line-of-Sight Quadrupole Mass Spectrometry: A Comprehensive Description of the Temporal Evolution of GaN Nanowire Ensembles". *Nano Lett.* 15 (2015), 1930.
- [14] FURTMAYR, F., VIELEMAYER, M., STUTZMANN, M., ARBIOL, J., ESTRADÉ, S., PEIRO, F., MORANTE, J. R., AND EICKHOFF, M. "Nucleation and growth of GaN nanorods on Si (111) surfaces by plasma-assisted molecular beam epitaxy - The influence of Si- and Mg-doping". *J. Appl. Phys.* 104 (2008), 034309.
- [15] GEORGAKILAS, A., ARETOULI, K., AND TSAGARAKI, K. "Method for Heteroepitaxial growth of III metal-face polarity III-nitrides on substrates with diamond crystal structure and III-nitride semiconductors". "PCT/EP2013/058560 (Apr 24, 2013), pub. no: WO/2013/160383 A1 (Oct 31, 2013)".
- [16] HESTROFFER, K., AND DAUDIN, B. "A RHEED investigation of self-assembled GaN nanowire nucleation dynamics on bare Si and on Si

- covered with a thin AlN buffer layer". *Phys. Status Solidi RRL* 7 (2013), 835.
- [17] HESTROFFER, K., LECLERE, C., CANTELLI, V., BOUGEROL, C., RENEVIER, H., AND DAUDIN, B. "In situ study of self-assembled GaN nanowires nucleation on Si(111) by plasma-assisted molecular beam epitaxy". *Appl. Phys. Lett.* 100 (2012), 212107.
- [18] KNELANGEN, M., CONSONNI, V., TRAMPERT, A., AND RIECHERT, H. "In situ analysis of strain relaxation during catalyst-free nucleation and growth of GaN nanowires". *Nanotechnology* 21 (2010), 245705.
- [19] KRUSE, J. E., LYMPERAKIS, L., EFTYCHIS, S., ADIKIMENAKIS, A., DOUNDOULAKIS, G., TSAGARAKI, K., ANDROULIDAKI, M., OLZIER-SKY, A., DIMITRAKIS, P., IOANNOU-SOUGLERIDIS, V., NORMAND, P., KOUKOULA, T., KEHAGIAS, T., KOMNINOU, P., KONSTANTINIDIS, G., AND GEORGAKILAS, A. "Selective-area growth of GaN nanowires on SiO₂-masked Si (111) substrates by molecular beam epitaxy". *J. Appl. Phys. Lett.* 113 (2016), 224305.
- [20] KUMAR, P., TUTEJA, M., KESARIA, M., WAGHMARE, U., AND SHIVAPRASAD, S. "Superstructure of self-aligned hexagonal GaN nanorods formed on nitrided Si(111) surface". *Appl. Phys. Lett.* 101 (2012), 131605.
- [21] LANDRE, O., BOUGEROL, C., RENEVIER, H., AND DAUDIN, B. "Nucleation mechanism of GaN nanowires grown on (111) Si by molecular beam epitaxy". *Nanotechnology* 20 (2009), 415602.
- [22] LARGEAU, L., GALOPIN, E., GOGNEAU, N., TRAVERS, L., GLAS, F., AND HARMAND, J.-C. "N-Polar GaN Nanowires Seeded by Al Droplets on Si(111)". *Cryst. Growth Des.* 12 (2012), 2724.
- [23] LOUARN, A. L., VEZIAN, S., SEMOND, F., AND MASSIES, J. "AlN buffer layer growth for GaN epitaxy on (111) Si: Al or N first?". *J. Cryst. Growth* 311 (2009), 3.
- [24] MUSOLINO, M., TAHRAOUI, A., FERNANDEZ-GARRIDO, S., BRANDT, O., TRAMPERT, A., AND L. GEELHAAR, H. R. "From nucleation to growth of catalyst-free GaN nanowires on thin AlN buffer layer". *Nanotechnology* 26 (2015), 085605.
- [25] RISTIC, J., CALLEJA, E., FERNANDEZ-GARRIDO, S., CERUTTI, L., TRAMPERT, A., JAHN, U., AND PLOOG, K. H. "On the mechanisms

- of spontaneous growth of III-nitride nanocolumns by plasma-assisted molecular beam epitaxy". *J. Cryst. Growth* 310 (2008), 4035.
- [26] SABELFELD, K. K., KAGANER, V. M., LIMBACH, F., DOGAN, P., BRANDT, O., GEELHAAR, L., AND RIECHERT, H. "Height self-equilibration during the growth of dense nanowire ensembles: Order emerging from disorder". *Appl. Phys. Lett.* 103 (2013), 133105.
- [27] SONGMUANG, R., LANDRE, O., AND DAUDIN, B. "From nucleation to growth of catalyst-free GaN nanowires on thin AlN buffer layer". *Appl. Phys. Lett.* 91 (2007), 251902.
- [28] WIERZBICKA, A., ZYTKIEWICZ, Z. R., KRET, S., BORYSIUK, J., DLUZEWski, P., SOBANSKA, M., KLOSEK, K., RESZKA, A., TCHUTCHULASHVILI, G., CABAJ, A., AND LUSAKOWSKA, E. "Influence of substrate nitridation temperature on epitaxial alignment of GaN nanowires to Si(111) substrate". *Nanotechnology* 24 (2013), 035703.
- [29] YAMABE, N., SHIMOMURA, H., SHIMAMURA, T., AND OHACHI, T. "Nitridation of Si(111) for growth of 2H-AlN(0001)/ β -Si₃N₄/Si(111) structure". *J. Cryst. Growth* 311 (2009), 3049.
- [30] ZUNIGA-PEREZ, J., V. CONSONNI, L. L., KONG, X., TRAMPERT, A., FERNANDEZ-GARRIDO, S., BRANDT, O., RENEVIER, H., KELLER, S., HESTROFFER, K., WAGNER, M. R., REPARAZ, J. S., AKYOL, F., RAJAN, S., RENNESSON, S., PALACIOS, T., AND FEUILLET, G. "Polarity in GaN and ZnO: Theory, measurement, growth, and devices". *Appl. Phys. Rev.* 3 (2016), 041303.

GaN NW growth on off-axis Si (111) wafers

In this chapter we study the effects of GaN NWs growth on off-axis Si (111) substrates. More specifically we focus on the $(0001)_{\text{GaN}}//(\text{111})_{\text{Si}}$ epitaxial relation for GaN NWs grown on Si (111) substrates with different miscut angles, and for GaN NWs grown on nominally identical Si (111) off-axis substrates (with miscut angle of 3.7°) but different interfacial structures.

8.1 Effects of the Si (111) miscut angle on GaN NWs growth

In this section, we focus on the effects of the miscut of Si (111) wafers on the spontaneous growth of GaN NWs. For this reason we used an identical growth process in Si (111) substrates with different miscut angles towards the $[2-1-1]_{\text{Si}}$ direction (i.e., nominally 0° , 1° , 3° and 5°).

Table 8.1: Results of the XRD measurements for samples with GaN NWs grown on off-axis Si (111) substrates with different miscut angles, showing the nominal and measured tilt angle (in respect to the substrate surface) of the Si (111) planes (α_{Si}), the measured tilt angle of the GaN (0001) planes (α_{GaN}), the relative angle between GaN (0001) and Si (111) tilt direction on the substrate surface ($\Delta\beta$) and the GaN (0001) tilt angle projected on the plane derived by the Si [111] direction and the surface normal (γ).

Sample No	Nominal α_{Si} ($^\circ$)	Measured α_{Si} ($^\circ$)	Measured α_{GaN} ($^\circ$)	$\Delta\beta$ ($^\circ$)	γ
Mis0	0	0.24	0.65	19.05	0.62
Mis1	1	0.82	0.45	1.09	0.45
Mis3	3	2.97	1.43	3.01	1.43
Mis5	5	4.42	1.52	18.47	1.44

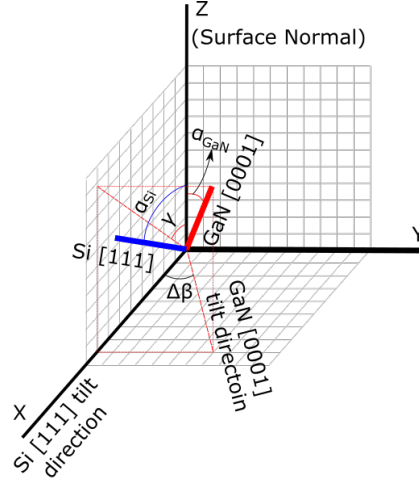


Figure 8.1: Illustration showing the relative direction of the normal on the substrate surface (Z -axis) and the Si [111] (blue line) and GaN [0001] (red line) crystal directions. The drawing also shows the Si [111] tilt angle, α_{Si} , the GaN [0001] tilt angle, α_{GaN} , the angle between the GaN [0001] tilt direction and the Si [111] tilt direction, $\Delta\beta$, and the projected GaN [0001] tilt angle towards the Si [111] tilt direction, γ . The apparent angles are larger compared to the real values, for illustrative reasons

The Si (111) wafers described in this subsection, were initially cleaned with Piranha ($H_2SO_4:H_2O_2$ 4:1), and after careful rinsing in deionized water (DI), the Si substrates were dipped into HF solution ($HF:H_2O_2$ 1:10) for 30 sec. After rinsing again in DI, the Si substrates were immediately loaded into the load chamber of the MBE system, in order to avoid oxidization of the surface. After an initial outgas of the substrate at $800^\circ C$, we deposited a thin nucleation layer consisting of AlN and GaN (i.e., 0.35 nm and 0.8 nm) at $765^\circ C$ and $685^\circ C$, respectively. This was followed by 20 min of nitridation at $760^\circ C$. Finally, GaN was deposited at $760^\circ C$ under nitrogen rich conditions for a duration of 3h. This procedure was used in our early GaN NWs growth experiments, and although the interfacial structure of the specific samples was not studied by HRTEM, from a similar sample study (i.e., HRTEM study of a sample with 0.38 nm AlN prelayer on Si, presented in Chapter 7) we expect the formation of an amorphous Si_xN_y interfacial layer. However, as the Si miscut angle plays a significant role in the GaN/AlN nucleation process, the structure and morphology of the interfacial region in each sample could be different.

In order to identify the relation of the Si [111] and GaN [0001] directions, ω -scans centered at the Si (111) and GaN (0002) planes were performed

for different ϕ angles. After the appropriate fitting [1] we found the tilt angle and tilt direction for the Si [111] and GaN [0001] crystal directions in comparison to the normal direction (z -axis) on the surface of the off-axis Si (111) substrates. Figure 8.1 illustrates the tilt angles of the Si [111] (α_{Si}), and GaN [0001] (α_{GaN}) crystal directions, and the misorientation angle $\Delta\beta$ between the corresponding tilt directions on the plane of the substrate surface. The apparent angles in Fig. 8.1 are larger compared to the real values, for illustrative reasons. We also calculated the projection of α_{GaN} on the plane defined by the Si [111] direction and the surface normal, γ , as can be seen in Fig. 8.1. This calculation was performed because the tilting direction of the GaN (0002) planes was not identical with the tilting direction of the Si (111) planes (i.e., $\Delta\beta \neq 0$). However, due to the small value of $\Delta\beta$ ($<20^\circ$), α_{GaN} was almost identical to γ for all the samples. The results of the above measurements can be seen in Table 8.1.

Fig. 8.2.a, shows how the difference $\Delta\beta$ in the tilt direction of the Si (111) and GaN (0001) planes changes, compared to the off-axis Si (111) wafer miscut angle α_{Si} . On Si substrates with miscut angles of 0.82° and 2.97° the tilt direction of GaN (0001) planes is almost identical with that of the Si (111) planes ($\Delta\beta = 1.09^\circ$ and 3.01° respectively). For Si substrates with miscut angles of 0.24° and 4.42° , although the measured $\Delta\beta$ is larger compared to the aforementioned ones (19.05° and -18.47° respectively), they still show a preferential alignment of the GaN (0001) tilting with the Si (111) tilting. Fig. 8.2.b, shows α_{GaN} and γ compared to α_{Si} . As we can see both α_{GaN} and γ increase with the Si miscut angle (MIS3 and MIS5). We interpret these results as indicating that the $(0002)_{GaN} // (111)_{Si}$ epitaxial relation between the GaN NWs and the Si substrate appears to be dominant even on off-axis Si (111) substrates.

Interestingly, as can be seen in Fig. 8.3, the morphological characteristics of GaN NWs also change with increasing the miscut angle of the Si wafers. Figs. 8.4.a, b and c show the measured diameter, height and density of the GaN NWs with the measured miscut angle of the off-axis Si (111) wafers. The most notable change observed is the reduction of the NW diameter with increasing Si miscut angle (Fig. 8.4.a). We also observe a trend for reduced NW height with increasing Si (111) miscut angle (i.e., 200 nm reduction for 4.4° miscut angle compared to 0.25° miscut), as well as an increase of 30% in the NW density (from $1.3 \times 10^{10} \text{cm}^{-2}$ to $1.7 \times 10^{10} \text{cm}^{-2}$). These differences in the NW morphological characteristics reflect changes in the NW growth procedure. The smaller NW diameter, and smaller height suggest a delay in the NW nucleation (i.e., larger incubation time) for samples with larger miscut angles.

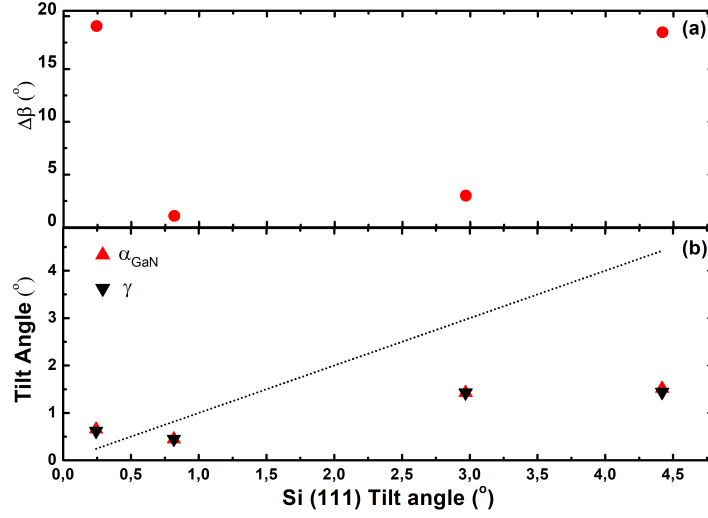


Figure 8.2: Results of the XRD measurements for GaN NWs grown on Si (111) substrates with increasing miscut angles (0.24° , 0.82° , 2.97° and 4.42°). Graph (a) shows (a) the relative angle of the Si (111) and GaN (0001) directions ($\Delta\beta$) and graph (b) shows the tilt angle of GaN (0001) planes (α_{GaN}) and its projection on the Si [111] / substrate surface normal plane (γ)

8.2 Effects of the interfacial structure on GaN NW growth on off-axis Si (111) wafers

In this section, we studied the role of different interfacial structures between the GaN NWs and the Si (111) off-axis substrates (with 3.7° nominal miscut angle towards the $[2\bar{1}\bar{1}]$ direction). For this reason, samples with different growth procedures were grown.

For samples MisNitr1 and MisNitr2, the initial substrate surface was intentionally exposed to active nitrogen for 20 min, at 760°C and 750°C , respectively. Then active nitrogen species and Ga atoms were deposited at nitrogen rich conditions (N:Ga = 5:1), but at different fluxes (i.e. the Ga-limited nominal GaN growth rates were 84.6 nm/h for MisNitr1 and 78.7 nm/h for MisNitr2). The difference of the fluxes was due to a large time-difference between the growth of the two samples, that resulted to some changes of the source. Nevertheless, the differences are not significant in order to affect the interfacial structure, or the epitaxial relation. According to Chapter 6, this growth procedure is expected to form an amorphous Si_xN_y

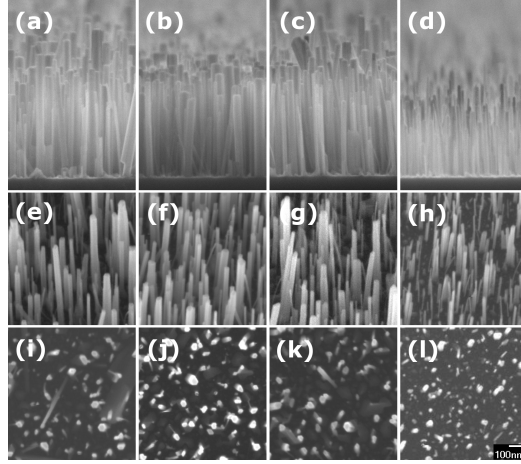


Figure 8.3: Cross-section (top row), tilted (middle row) and top view (third row) SEM micrographs of GaN NWs grown on Si (111) substrates with increasing miscut angles: 0.24° (a, e, i), 0.82° (b, f, j), 2.97° (c, g, k) and 4.42° (d, h, l).

interfacial layer between the GaN NWs and the Si (111) substrate.

The comparison of GaN NWs grown on on-axis and off-axis Si (111) substrates after intentional nitridation of the substrate surface could help to clarify the growth of GaN on nitridated Si. This investigation was aimed to identify whether the [0001] axis of the GaN NWs will be aligned with the substrate surface normal or the Si [111] crystal direction. This would confirm or not the epitaxial growth of GaN NWs through the Si_xN_y interfacial layer.

Sample MisNitSiN was identical with sample MisNitr2, with the difference that after the intentional exposure of the Si substrate to active nitrogen, an additional layer of 10 nm of SiN (nominally) was deposited, prior any GaN deposition. In-situ Si_xN_y deposition was accomplished with a special Si sublimation source. In the case of sample MisAlN, 1.5 nm of AlN was deposited on the initial Si surface, followed by exposure to active nitrogen for 20 min, followed by GaN growth under conditions identical with sample MisNitr1.

According to the above growth procedures, the three different interfacial structures studied were a thin (~ 1.5 nm) amorphous Si_xN_y layer (samples MisNitr1 and MisNitr2), a thicker (~ 11.5 nm) amorphous Si_xN_y layer (sample MisNitSiN) and a crystalline AlN interlayer.

We performed XRD measurements (as described in the previous section) in order to determine accurately the Si (111) miscut angle (α_{Si}), the GaN [0001] tilt angle (α_{GaN}), and the difference between the Si (111) and GaN (0001) tilt directions ($\Delta\beta$). Additionally, we measured the full width half

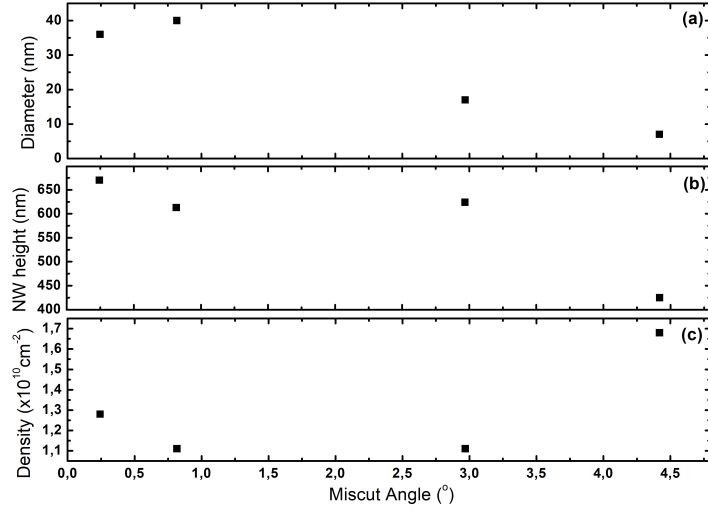


Figure 8.4: Results of SEM image measurements for GaN NWs grown on Si (111) substrates with different miscut angles, showing (a) the diameter, (b) the NW height and (c) the density of the GaN NWs

maximum (FWHM) of the GaN (0002) rocking curves. The results of these measurements together with the calculated GaN (0001) tilt direction projected towards the Si(111) miscut direction (γ) are shown in Table 8.2. Similarly with the previous section, due to the small $\Delta\beta$, γ is almost identical with α_{GaN} .

In Fig. 8.5, we see α_{Si} and α_{GaN} angles for the samples studied, and their difference ($|\alpha_{\text{GaN}} - \alpha_{\text{Si}}|$), according to the expected interfacial structures. The sample with the thicker amorphous Si_xN_y interfacial layer (~ 11.5 nm) exhibited a larger difference between the two tilt angles compared to that of the samples with the thin, 1.5 nm Si_xN_y layer (i.e., 1.14° compared to $\sim 0.5^\circ$). Additionally, the measured value of the FWHM of $(0002)_{\text{GaN}}$ RC and angle $\Delta\beta$ were also larger for the sample with the thicker amorphous layer (Fig. 8.6). These results suggest that with increasing the thickness of the amorphous Si_xN_y , the epitaxial relation between GaN NWs and the Si (111) substrate (that is present for samples with thin amorphous Si_xN_y interfacial layer, according to our findings in Chapter 6) is weakened.

It should be noted that the measured $\Delta\beta$ for the two GaN NW samples grown on nitrated Si (that forms a thin amorphous interfacial layer), samples MisNitr1 and MisNitr2, was significantly different (16.79° and 4.75° respectively). However, both $\Delta\beta$ values were very small, suggesting that the tilt of the GaN (0001) NW plane is approximately aligned with the tilt of the off-axis Si substrate. Even more, the FWHM of $(0002)_{\text{GaN}}$ RC was identical

Table 8.2: Results of XRD measurements for samples with GaN NWs grown on off-axis Si (111) substrates with nominal 3.7° miscut angle towards the Si [2-1-1] direction. We can see the results of the tilt angle (in respect to the substrate surface) of the Si (111) plane (α_{Si}), the measured tilt angle of the GaN (0001) planes (α_{GaN}), the relative angle between GaN (0001) and Si (111) tilt direction on the substrate surface ($\Delta\beta$), the FWHM of the GaN (0002) RC, and GaN (0001) tilt angle projected on the plane derived by the Si [111] direction and the surface normal (γ).

Sample Name	Interfacial structure	α_{Si}	α_{GaN}	$\Delta\beta$	(0002) _{GaN} FWHM	γ
MisNitr1	1.5 nm amorphous Si _x N _y	3.96	3.42	-16.79	4.9	3.41
MisNitr2	1.5 nm amorphous Si _x N _y	3.7	4.17	-4.75	4.9	3.69
MisNitSiN	11.5 nm amorphous Si _x N _y	3.6	2.44	-22.23	8.31	2.438
MisAlN	1.5 nm crystalline AlN	3.71	1.14	-2.11	0.9	1.14

for both of these samples (4.9°).

Surprisingly, the difference between Si (111) and GaN (0001) tilt angles is larger for the sample of the GaN NWs grown after the deposition of an AlN prelayer on Si. As we showed in Chapter 7, the presence of a crystalline AlN interfacial layer enhances the epitaxial relation between the substrate and the grown GaN NWs. Accordingly one would expect a smaller difference between the two tilt angles.

Differences between the tilt angles of off-oriented substrates and epilayers have been observed by Nagai for InGaAs layers grown on miscut GaAs surfaces [2] and attributed to a misfit strain relaxation mechanism. According to Nagai's model (Fig. 8.7), the difference between the tilt angles of the substrate and of the epitaxial layer ($\Delta\alpha$) depend on the miscut angle (step length), the step height of the substrate (h_{Si}) and the lattice constant of the epitaxial layer, as shown in the equations 8.1-8.3.

$$\tan(\Delta\alpha) = \frac{c_{AlN}/2 - h_{Si}}{L} \quad (8.1)$$

$$\tan(\alpha_{Si}) = \frac{h_{Si}}{L} \quad (8.2)$$

$$\tan(\Delta\alpha) = \frac{c_{AlN}/2 - h_{Si}}{h_{Si}} \times \tan(\alpha_{Si}) \quad (8.3)$$

As a consequence from equation 8.1 $\Delta\alpha$ is negative when $c_{AlN}/2 < h_{Si}$. When GaN is grown on AlN (0002), it follows the same growth direction (i.e. (0002)_{GaN}//(0002)_{AlN}) and any tilt observed for the GaN crystal is

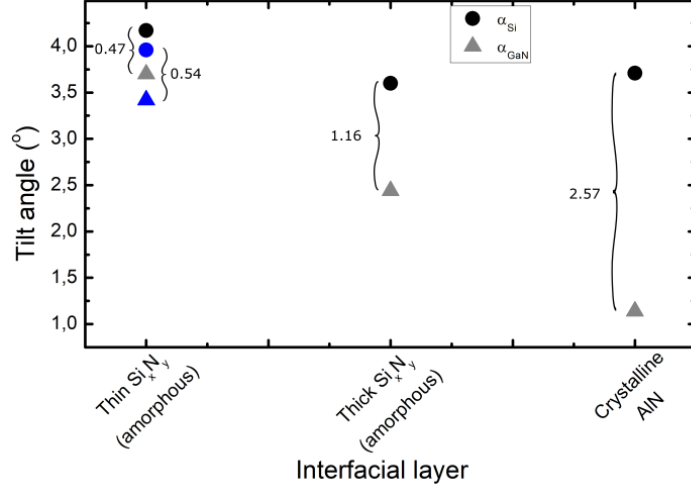


Figure 8.5: The miscut angle (α_{Si}) and the GaN (0002) tilt angle (α_{GaN}) can be seen for GaN NWs grown on miscut Si (111) wafers, with different interfacial layers. The difference between the two angles for each sample is marked.

induced by the AlN/Si interfacial structure [3]. The measured difference between the two tilt angles ($\alpha_{GaN} - \alpha_{Si}$) was -2.56° , compared to -0.740° calculated from the Nagai model ($c_{AlN}/2 = 2.491\text{\AA}$, $h_{Si} = 3.135\text{\AA}$). The sign of $\Delta\alpha$ is in agreement with Nagai's strain relaxation concept. However, the situation is more complex at the highly lattice mismatched AlN/Si interface that contains a high density of misfit dislocations. It is anticipated that the presence of steps favors a particular Burgers vector component vertical to the interface which result to the observed tilting.

8.3 Conclusions

Overall, our findings from this chapter suggest that the $(0001)_{GaN} // (111)_{Si}$ epitaxial relation is dominant in the GaN NW growth on off-axis Si (111) substrates for all the samples studied. The results reveal that the the miscut angle of the Si (111) substrates affects the GaN NWs nucleation and elongation processes and thus their morphological characteristics. We found a weaker $(0001)_{GaN} // (111)_{Si}$ epitaxial relation for the thicker amorphous Si_xN_y interfacial layers. The epitaxial relation of GaN NWs with the Si (111) crystal even in the case of the intentionally deposited 10 nm Si_xN_y interfacial layer, suggest that local regions of the Si_xN_y layer should have preserved

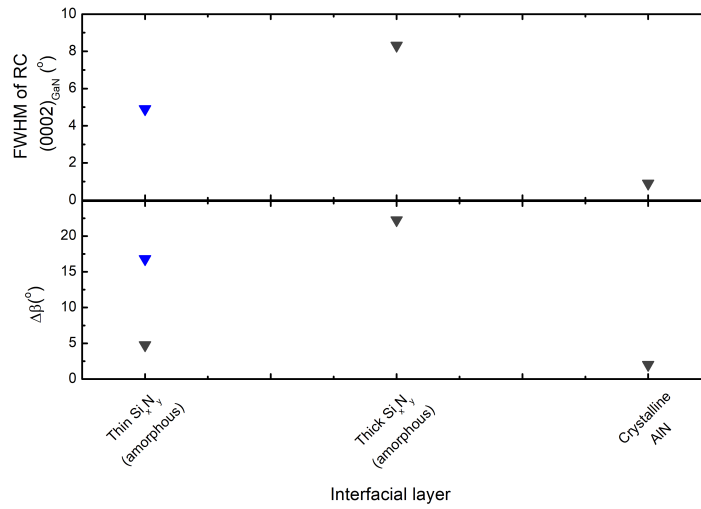


Figure 8.6: The FWHM of the $(0002)_{\text{GaN}}$ RC and the difference in the tilt directions between Si (111) and GaN (0002) ($\Delta\beta$) can be seen for NWs grown on nominally 3.7° off-axis Si (111) substrates, with different interfacial structures.

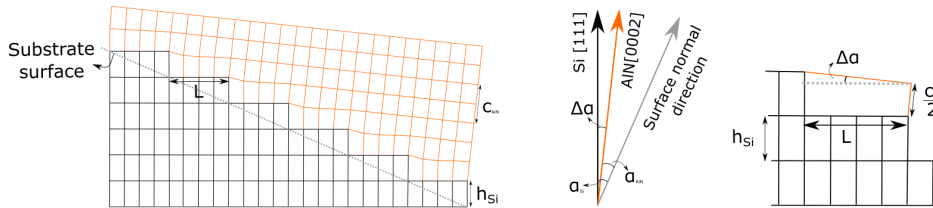


Figure 8.7: Schematic of the Nagai model, explaining the tilt between the substrate (Si (111), with black lines) and the epitaxial layer (AlN (0002), with orange line). The substrate surface is shown with a gray, dotted line.

their crystalline structure. Finally, the significant tilt angle observed between GaN [0001] and Si [111] for the case of GaN NWs grown on an AlN crystalline prelayer, cannot be explained by Nagai's model. The tilting of the AlN (0001) layer relative to the Si (111) crystal is attributed to the structure of the misfit dislocation network at the AlN/Si interface, which is induced by the presence of substrate steps.

Bibliography

- [1] M. A. Moram and M. E. Vickers. "X-ray diffraction of Nitrides". *Rep. Prog. Phys.*, 72:036502, 2009.
- [2] H. Nagai. "Structure of vapordeposited $\text{Ga}_x\text{In}_{1-x}\text{As}$ crystals". *J. Appl. Phys.*, 45:3789, 1974.
- [3] H. F. Liu, L. Zhang, S. J. Chua, and D. Z. Chi. "Crystallographic tilt in GaN-on-Si (111) heterostructures grown by metalorganic chemical vapor deposition". *J. Mater. Sci.*, 49:3305, 2014.

Selective-area growth of GaN NWs on bare Si (111) substrates

We analyze a method to selectively grow straight, vertical gallium nitride nanowires by plasma-assisted molecular beam epitaxy (MBE) at sites specified by a silicon oxide mask, which is thermally grown on silicon (111) substrates and patterned by electron-beam lithography and reactive-ion etching. The investigated method requires only one single MBE growth process, i.e., the SiO₂ mask is formed on silicon instead of on a previously grown GaN or AlN buffer layer. We present a systematic study involving various mask patterns, characterization by scanning electron microscopy, transmission electron microscopy, and photoluminescence spectroscopy, as well as numerical simulations, to evaluate how the dimensions (window diameter and spacing) of the mask affect the distribution of the nanowires, their morphology, and alignment, as well as their photonic properties. Capabilities and limitations for this method of selective-area growth of nanowires have been identified. A window diameter less than 50 nm and a window spacing larger than 500 nm can provide single nanowire nucleation in nearly all mask windows. Numerical simulations help in the understanding of the kinetics of Ga adatoms occurring on the surface, and identify the importance of the geometrical characteristics of the mask in achieving good selectivity. The results are consistent with a Ga diffusion length on the silicon dioxide surface in the order of approximately 1 μm .

9.1 Introduction

As we have mentioned in the previous chapters, spontaneous growth of GaN NWs by PA-MBE results in high quality GaN crystals that can be grown on a variety of different substrates with high lattice-mismatch. The defect free nature of the NW crystal makes NWs ideal for applications in optoelec-

tronic devices. However, other applications, such as vertical transistors [5] and on-chip optical interconnections [4] require a better control of the NW positioning and arrangement than the one obtained from the spontaneously grown method. This is commonly achieved through the selective-area growth method (SAG). During this procedure, the nucleation sites are specified on a nitridated titanium mask, that is deposited either on GaN templates [12] or on GaN buffer layers [1]. Alternatively, silicon oxide [16, 18] or silicon nitride [3] masks on AlN layers have also been used. The window openings in these masks are most commonly defined by electron-beam lithography, or alternatively with focused ion-beam [19], photolithography [3] and colloidal lithography [2].

A critical step towards the success of the SAG method, is the preparation of the masked samples on which GaN will finally be deposited. This preparation is a multi-step process, which complicates the production of such samples. Any technique that reduces the steps required for the mask preparation, and thus simplifies the procedure, could greatly facilitate the application of the SAG method. In this work we apply such a technique and demonstrate its potential for success. We use a thermally prepared SiO₂ mask on Si (111) substrates, without any pre-deposition prior to the mask preparation (in contrast to what is commonly used) [13, 14]. This requires only one growth process in the MBE growth chamber, avoiding the presence of the buffer layer. Previous such attempts [6] failed to achieve selectivity, and had not resulted in well separated NWs. We enhance this technique by depositing an ultrathin AlN layer on top of the SiO₂ mask, prior to GaN growth and show that this leads to improved results.

Additionally, we perform systematic parameter study of the mask geometrical characteristics i.e. the diameter of the windows (D_w) and distances between them (S). We complement this with numerical calculations in order to investigate the effect of surface diffusion of gallium adatoms on the substrate and the geometric characteristics of the pattern mask on the nucleation of GaN inside the mask windows.

9.2 Experimental details

A 20 nm thick SiO₂ layer was thermally grown on the Si (111) surface and subsequently nanostructured by electron-beam lithography and reactive-ion etching with an Ar/CHF₃ mixture, by collaborating researchers (P. Dimitrakis, V. Ioannou-Sougleridis, A. Olziersky and P. Normand) of the Institute of Nanoscience and Nanotechnology, National Center of Scientific Research (NCSR) "Demokritos". The polymethyl methacrylate (PMMA) electron-

resist was removed by oxygen-plasma ashing before another layer of photoresist is applied to the substrates. After a photo-lithography step, a 2×2 cm² central region of the substrate, that carries the nanopatterns, is protected by a remaining photoresist, while the surrounding region undergoes an HF treatment exposing the Si (111) bare surface. This exposed area will serve as reference for RHEED observations. The remaining photoresist is removed by a second oxygen ashing followed by wet etching in Piranha solution (H₂SO₄:H₂O₂, 1:1) and other organic residuals. The final nano-pattern areas are shown in Fig. 9.1. Both hexagonal or square arrays of circular windows, with nominal D_w ranging from 20 nm to 200 nm and S between 50 nm and 10 μ m were prepared.

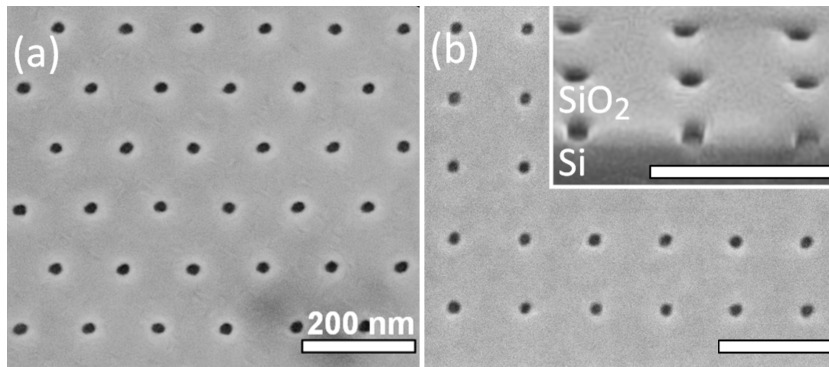


Figure 9.1: SEM images showing the processed patterns in 20 nm-thick thermally grown SiO₂ masks on Si (111) substrates with (a) hexagonal and (b) square lattices of circular windows (window diameter: $D_w = 20$ nm, window period/spacing: $S = 125$ nm). Inset of (b): Tilted cross-sectional view of the square lattice. The scale bar is 200 nm for all micrographs.

Prior to loading the substrates to the MBE system, they were dipped in a 1% HF solution for 20 sec, in order to remove the residual native oxide formed in the windows and the unmasked Si (111) surface of part of the wafer (used for spontaneous GaN NW growth). The substrate preparation treatment inside the MBE system was similar to the case of bare Si (111) substrates. The substrates were heated prior to any deposition at 800 °C, and there was a clear indication of the 7×7 pattern on the bare Si (111) surface that surrounded the central SiO₂ masked area. Although the HF etching process is expected to affect the final openings of the windows, inspection of empty windows in grown patterns revealed that the final openings were not significantly affected by this process (Fig. 9.2).

Different amounts of AlN prelayer were initially deposited on the patterned Si (111) wafers and annealed under active nitrogen, in order to study

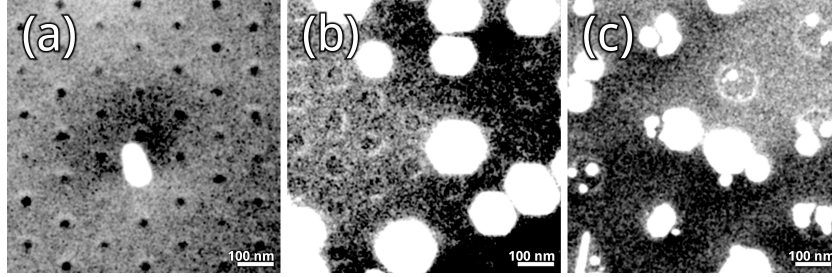


Figure 9.2: Top-view SEM images of some of the windows in the SiO_2 masks with window diameter D and spacing S , which have stayed partially empty during the growth of the nanowires. (a) $D_w = 20$ nm, $S = 125$ nm; (b) $D_w = 40$ nm, $S = 125$ nm; and (c) $D_w = 80$ nm, $S = 250$ nm.

its role on the nucleation and growth of the GaN NWs. GaN was deposited for a total growth time of 3h, at a constant substrate temperature of 760°C . The Ga:N incident flux ratio was kept constant at approximately 1:5, using fluxes of ~ 80 nm / h and ~ 430 nm / h of equivalent GaN growth rate under Ga and N limited growth rate conditions, respectively.

The results of the growth were evaluated through electronic microscopy techniques (SEM and TEM), and PL measurements. Simulations of the diffusion of Ga-adatoms were performed by the collaborating researcher Liverios Lymperakis of the Max Planck Institute für Eisenforschung in Düsseldorf, in order to gather insight into the atomistic processes during the incubation phase of the GaN NWs. In these simulations, the adatom density at each site of the substrate surface is determined by the equilibrium between arrival, evaporation, and diffusion rates. They qualitatively describe the spatial distribution of the adatom chemical potential and densities on the surfaces of the mask and its windows. Hence, they provide valuable insight on the nucleation probabilities as a function of mask geometry, i.e., window spacing and diameters and adatom diffusion lengths.

9.3 Results and discussion

The successful epitaxial growth of GaN NW patterns is a result of the right combination of the MBE growth conditions (i.e. substrate temperature and active N and Ga fluxes) and appropriate mask characteristics (i.e. mask material, window diameter and window distances). Additionally, the initial deposition of a small amount of AlN is also crucial, as revealed by our experiments.

9.3.1 Role of AlN prelayer

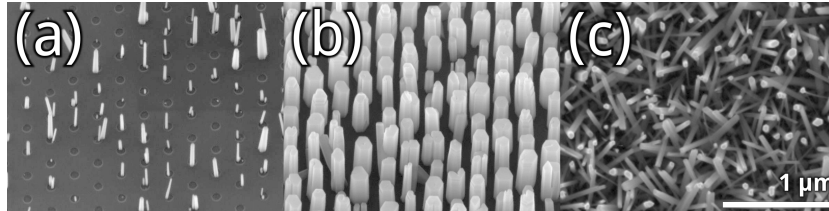


Figure 9.3: SEM tilted view images showing the same region of patterned mask ($S = 250$ nm and $D_W = 60$ nm) for 3 different GaN NW samples, grown on identically grown conditions but with different amounts of AlN deposition. (a) No AlN was deposited, (b) 0.4 nm of AlN was deposited, (c) 1.5 nm of AlN was deposited. The scale in all three images is shown in (c).

We studied the effects of 0 nm, 0.4 nm and 1.5 nm of nominal AlN prelayer thicknesses. Fig. 9.3 shows the growth results, for the three different cases that were studied, for mask windows with $D_W = 60$ nm and $S = 250$ nm. In the case that no AlN prelayer was deposited, and the patterned substrate was exposed for 20 min to active nitrogen, SEM images (Fig. 9.3.a) revealed partial nucleation of GaN NWs in the window holes. This suggests that GaN NW nucleation on the nitridated (Si_xN_y formation) surface within the windows is preferred compared to the surface of the SiO_2 mask. This may reflect a smaller incubation time for GaN nucleation on Si_xN_y compared to SiO_2 , although it could be also related to the thinner Si_xN_y layer (~ 1.5 nm) expected to form from nitridation of the Si (111) surface [9], compared to the thicker (~ 20 nm) thermally prepared SiO_2 . Additionally, there could also be crystalline domains inside the amorphous Si_xN_y , something that would also reduce the incubation time for GaN nucleation, compared to nucleation on the amorphous SiO_2 mask.

When a nominal thickness of 1.5 nm AlN was initially deposited on the patterned substrate (Fig. 9.3.c), GaN NWs were nucleated both inside the windows and on the surface of the SiO_2 mask. This indicates that the amount of deposited AlN prelayer was enough to enhance the nucleation both on the window surface, but also on the SiO_2 mask, which would otherwise be suppressed. The enhanced nucleation of GaN NWs after initial deposition of 1.5 nm AlN, can be attributed to the stronger bonding of the Ga, N adatoms on the AlN surface in comparison to the Si (111) and the amorphous SiO_2 surfaces. It can also be attributed to the smaller interfacial energy of GaN/AlN compared to GaN/Si or GaN/ SiO_2 , or to the epitaxial constraints between GaN and AlN and hence to the stronger driving force for the shape

transition from spherically capped precursors to truncated pyramids [7].

In the intermediate case of 0.4 nm of nominal AlN thickness (Fig. 9.3.b), GaN NWs were grown inside the majority of the windows for several window spacings and diameters, while there was no growth observed on the mask. Although the presence of two monolayers of AlN at the GaN/Si interface has not been identified in the HRTEM investigations presented in the next section, the influence of the 0.4 nm AlN deposition for a better growth selectivity is evident. Following the findings of Chapter 7, concerning the effects of ultrathin AlN prelayers, this could be attributed to the presence of sparse AlN crystalline regions.

9.3.2 Effects of the mask geometrical characteristics

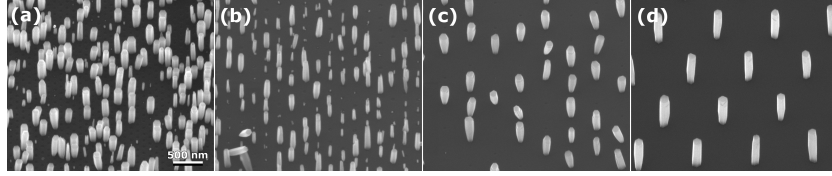


Figure 9.4: SEM images of tilted view of GaN NWs, on mask regions with $D_w = 40$ nm and different window spacings. (a) $S = 125$ nm, (b) $S = 250$ nm, (c) $S = 500$ nm and (d) $S = 1000$ nm.

After identifying that deposition of 0.4 nm AlN resulted in the best growth selectivity compared to 0 nm and 1.5 nm AlN, for mask windows with $S = 250$ nm and $D_w = 60$ nm, we now turn our attention on the effects of the geometrical characteristics of the mask. We performed a parameter study of masks having D_w of 20 nm, 40 nm, 60 nm, 80 nm, 100 nm and 200 nm and S of 125 nm, 250 nm, 500 nm, 1000 nm and 10 μm .

We first consider the effect of different spacings, S , shown in Fig. 9.4. The figure shows the grown GaN NWs in regions with windows having S 125 nm, 250 nm, 500 nm and 1000 nm, and identical diameter $D_w = 40$ nm. For the smallest S studied (125 nm), the growth experiment resulted in many empty windows i.e., windows not occupied by any NW (Fig. 9.4.a). In the other extreme, for $S = 1000$ nm, most of the windows are filled with NWs.

To quantify this trend, we define the filling factor (FF) as the ratio of the number of filled windows with a single, straight GaN NW over the total number of windows, expressed as a percentage. Fig. 9.5.a. shows the FF for different D_w and S . There are two apparent trends. First, the FF decreases as a function of D_w , for window-spacings of 250 nm (blue triangle pointing towards the right), 500 nm (green triangle pointing down) and 1000 nm (red

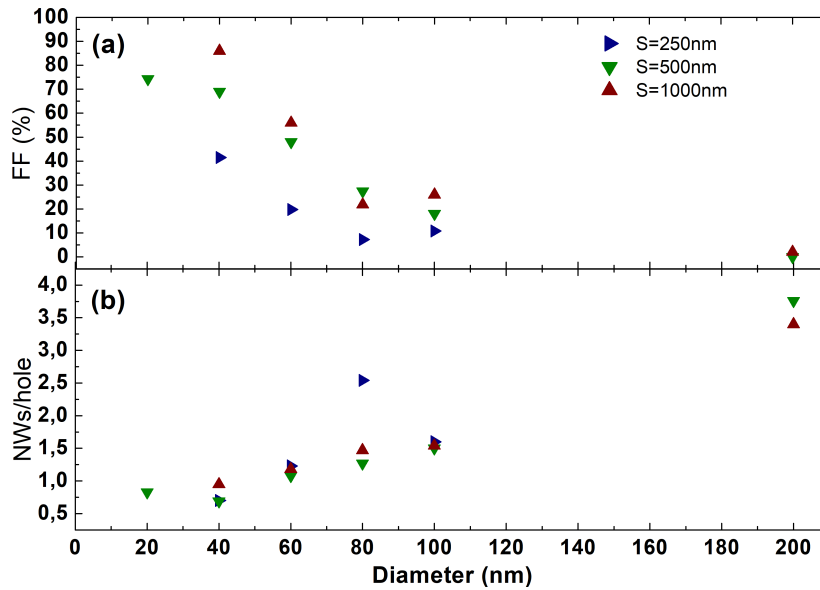


Figure 9.5: Plots illustrating (a) the FF and (b) the average NW number per window, for window spacings of 250 nm (blue triangle pointing towards the right), 500 nm (green triangle pointing down) and 1000 nm (red triangle pointing up), as a function of the window diameter (x -axis).

triangle pointing up). Second, for a given D_w , FF is higher for larger S . For $S = 1000$ nm, the measured FF reaches up to 90%. However, this is not the case for arbitrarily large S . In the case of $S = 10 \mu\text{m}$, we observed extensive GaN nucleation around the vicinity of each window as shown in Fig. 9.6.

Another interesting observation, is that the number of GaN NWs grown per window increases with the window diameter (Fig. 9.7). For the largest window diameter studied (200 nm) we measured up to 6 NWs per window, while the average NW number per window was ~ 4 . The increasing number of NWs per window compared to the window diameter can be clearly seen in Fig. 9.5.b. This also reflects in the reduction of the FF (for single GaN NW per window), observed with increasing window diameter, as shown in Fig. 9.5.a.

We now wish to evaluate the effects of the mask spacing on the morphological characteristics of the NWs. To do this we selected NWs that grew straight, vertically and separately inside the windows of the SiO_2 mask. We present the mean NW height and diameter for windows with $D_w = 40$ nm and different spacings ($S = 125$ nm, 250 nm, 500 nm and 1000 nm) in Fig. 9.8. It turns out that these NWs can have a diameter of 100 nm and more, which is larger compared to the diameter of the mask windows. The NW

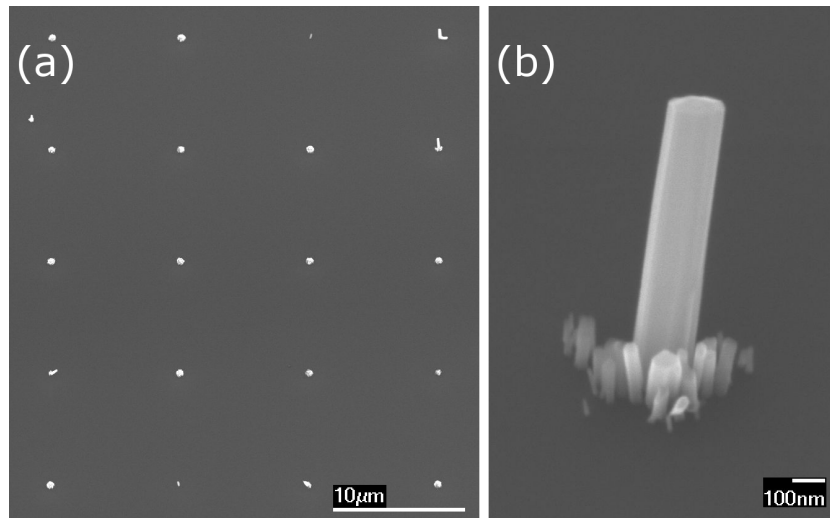


Figure 9.6: SEM images for a sample with a square pattern, with $S = 10 \mu\text{m}$ spacing and $D_w = 25 \text{ nm}$. (a) Top view of the sample, with a small magnification (scale bar is $10 \mu\text{m}$), and (b) SEM micrograph of a tilted-view GaN NW at a larger magnification (scale bar is 100 nm), focusing in the central grown window and in the NWs grown around the window.

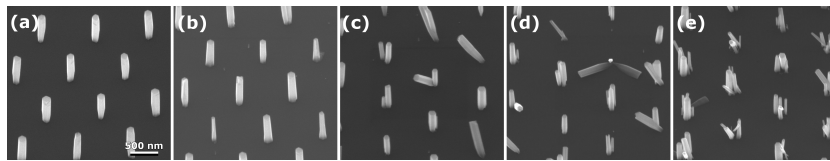


Figure 9.7: SEM images of the tilted view GaN NWs, on regions with $S = 1000 \text{ nm}$, and different window diameters. (a) $D_w = 40 \text{ nm}$ (b) $D_w = 60 \text{ nm}$ (c) $D_w = 80 \text{ nm}$ (d) $D_w = 100 \text{ nm}$ and (e) $D_w = 200 \text{ nm}$.

diameter is also larger than the diameter of the multiple NWs observed in the largest window openings. It is also substantially larger than the diameter of about $20 - 80 \text{ nm}$ of the nanowires grown outside the patterned area.

Under the used growth conditions, the diameters of the single-grown NWs inside the windows increased with the spacing of the windows. Additionally, the NW height is also found to increase with S . Similarly with the spontaneously grown GaN NWs, the height of all the NWs measured was larger than the equivalent Ga-limited GaN film thickness (240 nm) which is a sign of the diffusion induced mechanism described in Chapter 1.

A self regulating mechanism has been described for the growth of InN [8] and GaN nanostructures [10]. According to this mechanism, the NW diameter increases when Ga adatoms that reach the top surface of the NW

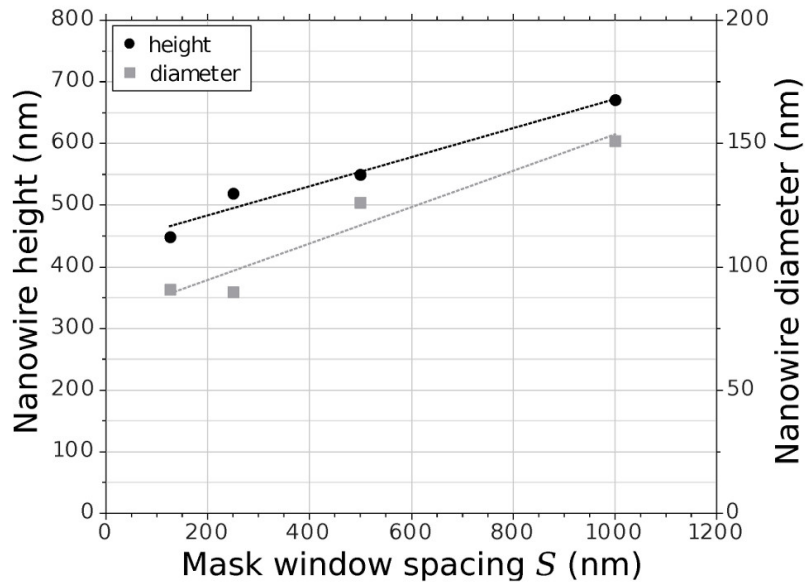


Figure 9.8: Average height (black circles) and diameter (gray squares) of NWs for different window spacing S , taking into account only nanowires that grew straight and separated inside windows of $D_w = 40$ nm diameter. The dotted lines are linear fits to the data.

exceed the amount of directly incident active N[10]. However, the height of the NWs is only a fraction of the equivalent N-limited GaN film thickness (1290 nm).

TEM studies revealed the growth of multiple, coalesced GaN NWs inside each window, in the case of $D_w = 80$ nm, as shown in figure Fig. 9.9.a. Lateral growth of the NWs over the SiO_2 mask is also observed. SAED patterns (inset in Fig. 9.9.a) reveal the good epitaxial relationship between the GaN NWs and the Si substrate. The perfect alignment of the coalesced GaN NWs can be seen in the HRTEM image of Fig. 9.9.b. The identification of limited stacking faults in the grown NWs, shows their superior quality compared to spontaneously grown GaN NWs. We can also identify crystalline Si regions, that are in direct contact with the NW. However, there was no identification of AlN at the interface. This was attributed either to the amorphization of ultrathin AlN during the nitridation, or due to sparse crystalline AlN regions, that allow for nitridation of the Si surface.

Photoluminescence (PL) measurements performed on the samples, showed a dominant emission peak around 3.47 eV, as shown in Fig. 9.10. The full width at half maximum (FWHM) of the PL spectrum of GaN NWs grown in the SiO_2 windows was larger compared to that of the spontaneously

grown NWs, that nucleated outside the pattern region. The FWHM of emission from GaN nanowires, grown in the windows with spacing $S = 500$ nm and diameter $D_W = 80$ nm, was about 6 meV, while the emission from nanowires in windows with $S = 1000$ nm and $D_W = 40$ nm exhibited FWHM of about 14 meV. These values are significantly broader compared to the ~ 2 meV FWHM of PL from nanowires which grew self-arranged outside the patterned (mask) area. These nanowires, grown on the surrounding bare Si (111) surface, show a series of sharper and partially overlapping peaks in the same spectral region. The strongest peak appears at a photon energy of $E_{DX_0} = 3.4705$ eV, which is attributed to the donor bound exciton (DX_0).

The inset in Fig. 9.10 shows the PL spectra taken at room temperature. No further emission peaks have been observed in the entire visible spectrum up to $\lambda=645$ nm, which indicates the excellent quality of the GaN crystals. At room temperature, the PL peaks are broader and appear shifted towards the red at 3.41 eV due to the temperature dependent change of the band-gap [15]. Emission at 3.45 eV is observed only for the thin nanowires (20–80 nm) grown on bare Si, while for the thicker nanowires, grown in the pattern area with window spacing of 500 nm or more, this PL peak is less visible. The 3.45 eV emission has been commonly observed in spontaneously grown GaN nanowires and its origin is still unclear [17]. Our results suggest that it is favored by increasing the GaN surface area per nanowire volume. The increased FWHM for the GaN nanowires grown inside the windows of the mask, as compared to those grown outside the mask, may be related to strain inhomogeneities along the diameter of the nanowires, since they are also partially overgrowing the SiO_2 mask as seen in the HRTEM images in Fig. 6. The dispersion of nanowire diameters could also result in different amount of strain in different nanowires and thus contribute to the increase of the FWHM. It may also indicate incorporation of different amounts of impurities from the mask surface.

Polarity tests were performed on different regions, with different geometrical characteristics. For GaN NWs grown in regions with $S = 1000$ nm and $D_w = 200$ nm, KOH etching revealed clear, pencil-like etched tips (Fig. 9.11.a), suggesting that they were N-polar [11]. However, the results of the KOH tests were not clear on other regions. For regions with $S = 500$ nm and $D_W = 80$ nm (Fig. 9.11.b) some NWs exhibited a clear pencil-like etched tip, but some others had a rough morphology of the top surface of the NW. Such a rough morphology could be the result of broken GaN NWs, or of the coalesced N-polar GaN NWs, that were etched separately.

For a better understanding of the GaN NW nucleation procedure on the patterned substrates, numerical calculations performed by L. Lympirakis determined the nucleation probability on the SiO_2 mask and on the windows

surface during the incubation period. These calculations aimed in providing a qualitative description to the processes governing the selectivity of the patterned samples.

The affinity A of the nucleation process can be written as $A = \Delta\mu_\infty - E$, where $\Delta\mu_\infty = \mu_{Ga} + \mu_N - \mu_{GaN}$ is the bulk supersaturation and μ_{Ga} , μ_N , and μ_{GaN} are the chemical potentials of Ga species, N species, and bulk GaN, respectively. E is always positive and incorporates the contributions to the free energy of the nucleus from the free surface, the nucleus-substrate interface, as well as the strain energy. The chemical potential of the adatoms depends on the temperature and the adatom density and can be written as $\mu = \mu_0 + k_B T \ln(c/c_0)$ where μ_0 and c_0 are the chemical potential and adatom density of a reference state, respectively, k_B is the Boltzmann constant, and T is the growth temperature. Nucleation of GaN on the surface is only possible if the change in the Gibbs free energy of the system is negative, and in turn the affinity of the nucleation becomes positive. For certain supersaturation values $\Delta\mu_\infty$, there is a critical size of nucleus, above which the affinity A is positive and effective as driving force for nucleation.

The model calculates the Ga-adatom density (the minority species), taking into account the equilibrium between arrival, evaporation and diffusion rates of the adatoms on the mask and hole surface. The final density is calculated through the numerical solution of the following steady-state diffusion equation [20] in a periodic array of mask windows having a hexagonal periodicity (Fig. 9.12):

$$\nabla D(\nabla c) - c/\tau_{des} + \phi = 0 \quad (9.1)$$

where D is the diffusion constant, c is the Ga adatom density, ϕ is the impinging Ga flux, and τ_{des} is the desorption-limited lifetime of an adatom. In the periodic array, GaN NWs are assumed to exist at the corners of the array, and are considered acting as sinks for the Ga adatoms. This causes a preferred diffusion towards the grown GaN NWs, thus suppressing the diffusion towards other precursors. The calculated distribution of the chemical potential of Ga adatoms (and thus of the Ga adatom density) can be seen in Fig. 9.12. The adatom density is reduced in the surrounding regions of the occupied windows, resulting in a decreased nucleation probability.

The extent of the affected region would depend on the diffusion length of the Ga-adatoms on the mask. For the neighbouring empty holes, the density of the adatoms (and thus the nucleation probability) would depend on the distance from the already grown GaN NWs. The nucleation probability would be reduced when an empty window is in the depleted region around the grown GaN NW. On the contrary, the nucleation probability would be

independent when the hole is at a large distance from the grown GaN NW.

In Fig. 9.13, we can see how the adatom density, and chemical potential for the surface of the window changes in the window surface, as a function of its diameter. The increased adatom density (and thus chemical potential) observed at the larger diameter holes, would result in an increased nucleation probability per area. This would result in multiple nucleation events per hole, leading to GaN NWs grown at the larger holes, as was observed.

The interaction between the windows, as a function of their distance, is quantified in Fig. 9.14. There we see the Ga adatom chemical potential and the adatom density as a function of the windows spacing, for three different diffusion lengths (400, 500 and 800 nm) and two different window diameters (60 nm and 80 nm). For spacing distances larger than two times the diffusion length, the interaction among the windows is suppressed, and the selectivity is independent of the density of the windows on the mask. On the contrary, when the spacing distance is smaller than the diffusion length, the interaction between the NWs is significant: the presence of a grown NW, reduces significantly the Ga adatom density, and thus the nucleation probability in neighbouring empty windows. The fact that the observed 90 % FF is observed for $S = 1000$ nm, suggests that the diffusion length of Ga adatoms on the mask at $T_{sub} = 760^\circ\text{C}$ is comparable to this value.

9.4 Conclusions

In this chapter, we have analyzed a method of growth of GaN NWs on patterned Si (111) substrates, without the use of any buffer layer. A good selectivity is achieved when a small amount of AlN is initially deposited on top of the patterned substrate, that does not alter the suppression of nucleation events on the mask, but enhances significantly nucleation events in the open mask windows. The absence of a buffer layer grown on Si before the patterning allows for a simplification in the substrate preparation steps, as no additional deposition step of any buffer layer is required.

In the presented work, we determined the role of the geometrical characteristics of the mask (i.e. window diameter and window distance) in controlling the growth and properties of the nanowires, such as selectivity, morphology and alignment. Windows with a smaller diameter than 50 nm, and distance above 500 nm resulted in a large percent of mask windows filled with straight vertical NWs. Larger diameter windows resulted in multiple NWs within each window. For a window distance smaller than 1000 nm, the filling factor was reduced, depending on the distance. The numerical calculations revealed an interaction between neighbouring mask windows. A nucleation

event in one window reduces the probability for nucleation in neighbouring holes that are within a Ga-diffusion-length distance. Combining this key result with our experimental findings, suggests a Ga-adatom diffusion length in the order of $1 \mu\text{m}$, in the growth conditions used. Therefore mask geometries that provide spacing approximately in the same order of the Ga-adatom diffusion length allow for a better filling factor of the mask windows.

These results help to pave the way to establish a nanowire SAG technology for the production of innovative nanoelectronic, photonic, and sensor devices based on the monolithic integration of III-nitride compound semiconductors on silicon.

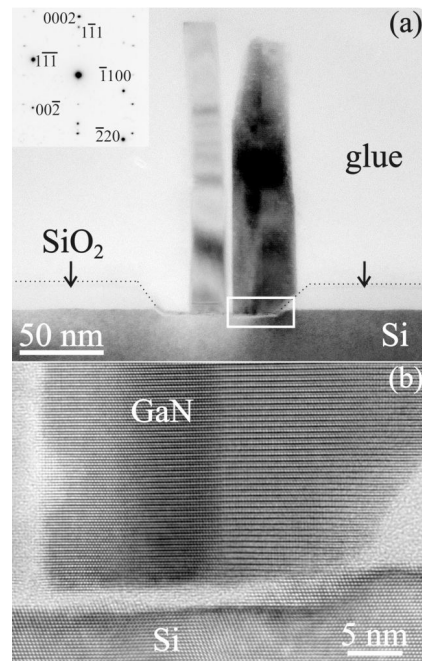


Figure 9.9: (a) TEM image depicting two nanowires in a single window ($D_w=80$ nm, $S=500$ nm), where the right one comprises two coalesced individual nanowires. The corresponding selected area electron diffraction (SAED) pattern (inset) reveals the epitaxial relationship between the Si and GaN lattices. Three-index reflections refer to Si, while four-index reflections belong to the wurtzite structure of GaN. (b) HRTEM image of the interfacial area indicated by the white rectangle in (a), along the $[11\bar{2}0]$ GaN/ $[110]$ Si projection direction, showing the nucleation site and the perfect lattice alignment of the coalesced nanowires. The rough Si surface of the window is covered by a thin amorphous layer of about 2 nm. Nevertheless, the epitaxial relation of GaN with Si remains unaffected.

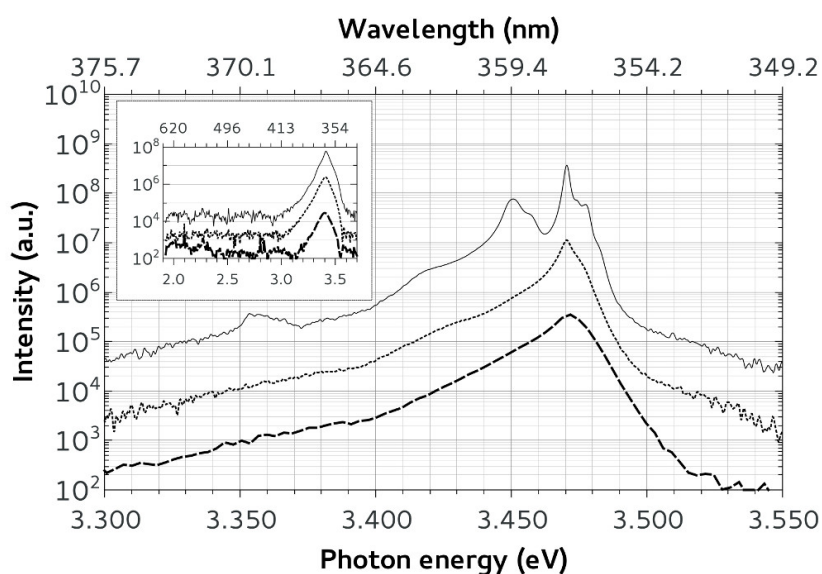


Figure 9.10: Photoluminescence in semi-logarithmic scale taken at 20K of nanowires grown self-arranged (upper, solid line) as well as inside windows with diameter D_w and spacing S of $D_w=80$ nm, $S=500$ nm (middle, dotted line) or $D_w=40$ nm, $S=1000$ nm (lower, dashed line). The inset shows the same measurements at room temperature. Emission happens only in the ultraviolet, no peaks appear throughout the entire measured visible spectrum. (The graphs have been separated by one decade for visibility: solid line $\times 100$, dotted line $\times 10$, and dashed line $\times 1$.)

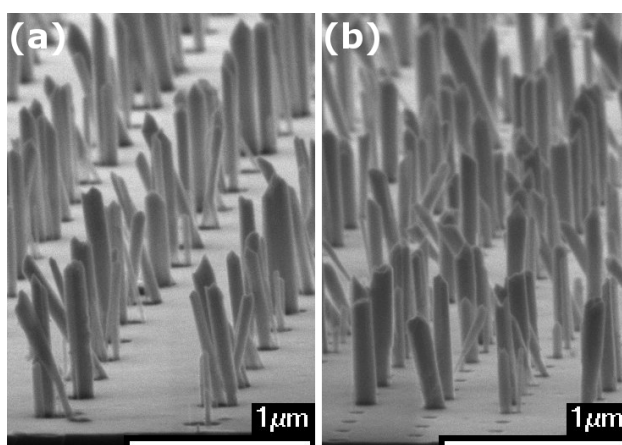


Figure 9.11: Cross-sectional tilted view of KOH etched GaN NWs grown on regions with (a) $S=1000$ nm and $D_w=200$ nm and (b) $S=500$ nm and $D_w=80$ nm

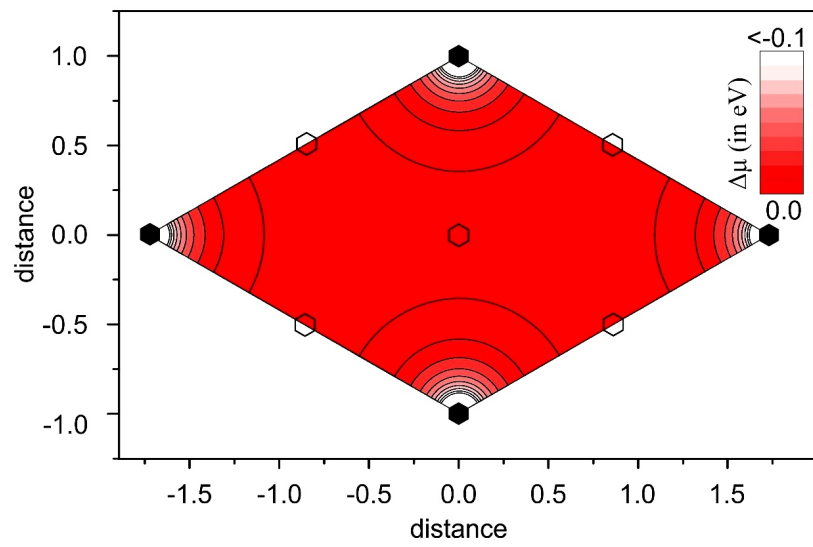


Figure 9.12: Contour plot indicating the chemical potential calculation of Ga adatoms. The open and filled hexagons indicate the position of the empty and filled with NW windows in the mask, respectively. The distances are in units of diffusion length. Periodic boundary conditions are applied in both directions.

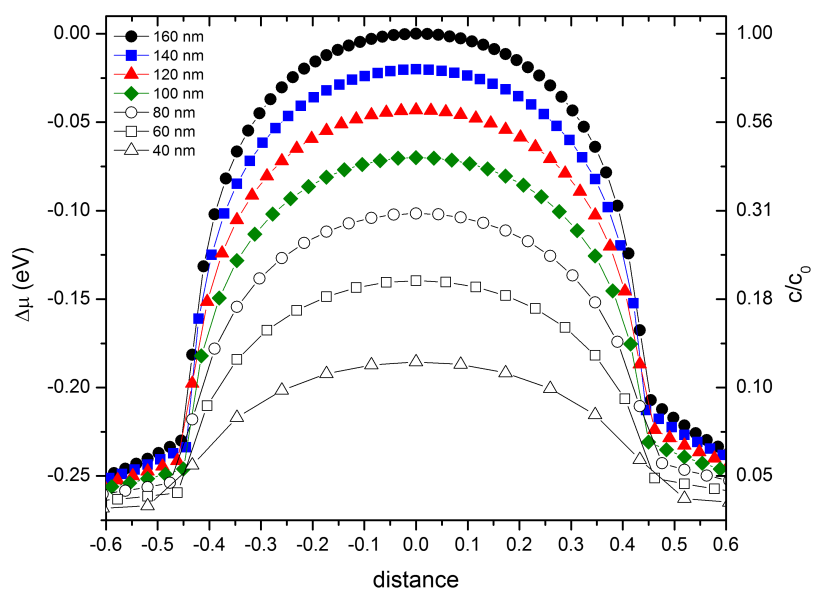


Figure 9.13: Change of the chemical potential $\Delta\mu$ and adatom density c in the window at the center of the supercell as function of distance from the center, for different window diameters. c_0 is the maximum adatom density calculated at the center of the widest window. The distance from the center of the window is in units of window diameter.

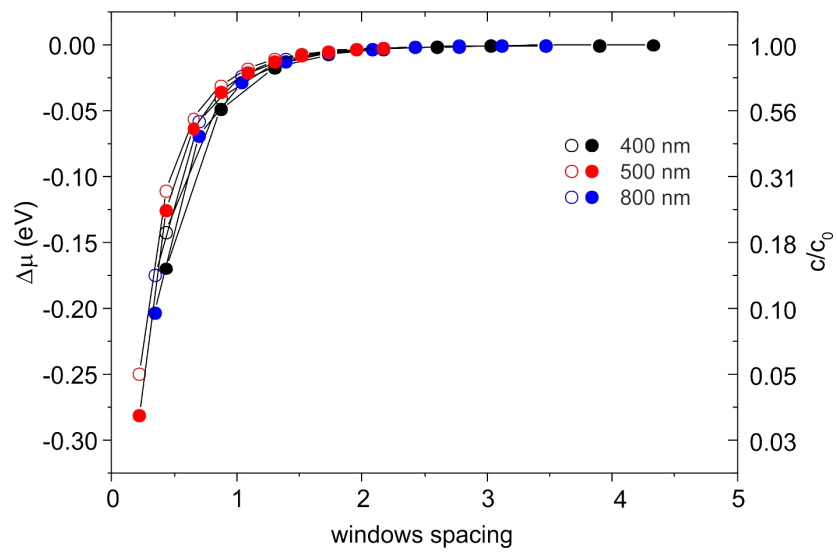


Figure 9.14: Change of the chemical potential $\Delta\mu$ and adatom density c in the window at the center of the supercell as function of the window spacing for various diffusion lengths of 400 nm (black circles), 500 nm (red circles) and 800 nm (blue circles), as well as window diameters of 60 nm (empty circles) and 80 nm (filled circles). c_0 is the maximum adatom density calculated for the maximum window spacing. The window spacing is in units of diffusion lengths.

Bibliography

- [1] ALBERT, S., BENGOCHEA-ENCABO, A., SANCHEZ-GARCA, M. A., KONG, X., TRAMPERT, A., AND CALLEJA, E. "Selective area growth of In(Ga)N/GaN nanocolumns by molecular beam epitaxy on GaN-buffered Si(111): from ultraviolet to infrared emission". *Nanotechnology* 24 (2013), 175303.
- [2] BENGOCHEA-ENCABO, A., ALBERT, S., SANCHEZ-GARCA, M., LOPEZ, L., ESTRADA, S., REBLED, J., PEIRO, F., NATAF, G., DE MIERRY, P., ZUNIGA-PEREZ, J., AND CALLEJA, E. "Selective area growth of a- and c-plane GaN nanocolumns by molecular beam epitaxy using colloidal nanolithography". *J. Cryst. Growth* 1 (2012), 353.
- [3] BERTNESS, K. A., SANDERS, A. W., ROURKE, D. M., HARVEY, T. E., ROSHKO, A., SCHLAGER, J. B., AND SANFORD, N. A. "Controlled nucleation of GaN nanowires grown with molecular beam epitaxy". *Adv. Funct. Mater.* 20 (2010), 2911.
- [4] BRUBAKER, M. D., BLANCHARD, P. T., SCHLAGER, J. B., SANDERS, A. W., ROSHKO, A., DUFF, S. M., GRAY, J. M., BRIGHT, V. M., SANFORD, N. A., AND BERTNESS, K. A. "On-Chip Optical Interconnects Made with Gallium Nitride Nanowires". *Nano Lett.* 13 (2013), 374.
- [5] BRYLLERT, T., WERNERSSON, L. E., LOWGEN, T., AND SAMUELSON, L. "Vertical wrap-gated nanowire transistors". *Nanotech.* 17 (2006), S227.
- [6] CALLEJA, E., RISTIC, J., FERNANDEZ-GARRIDO, S., CERUTTI, L., SANCHEZ-GARCIA, M. A., GRANDAL, J., TRAMPERT, A., JAHN, U., SANCHEZ, G., GRIOL, A., AND SANCHEZ, B. "Growth, morphology, and structural properties of groupIII nitride nanocolumns and nanodisks". *Phys. Status Solidi B* 244 (2007), 2816.

- [7] CONSONNI, V., HANKE, M., KNELANGEN, M., GEELHAAR, L., TRAMPERT, A., AND RIECHERT, H. "Nucleation mechanisms of self-induced GaN nanowires grown on an amorphous interlayer". *Phys. Rev. B* *83* (2011), 035310.
- [8] DIMAKIS, E., ILIOPOULOS, E., TSAGARAKI, K., AND GEORGAKILAS, A. Physical model of InN growth on Ga-face GaN (0001) by molecular-beam epitaxy. *Appl. Phys. Lett.* *86* (2005), 133104.
- [9] EFTYCHIS, S., J.KRUSE, T.KOUKOULA, TH.KEHAGIAS, PH.KOMNINOU, A.ADIKIMENAKIS, TSAGARAKI, K., M.ANDROULIDAKI, P.TZANETAKIS, E.ILIOPOULOS, AND A.GEORGAKILAS. "Understanding the effects of Si(111) nitridation on the spontaneous growth and properties of GaN nanowires". *J. Cryst. Gr.* (2016).
- [10] FERNANDEZ-GARRIDO, S., KAGANER, V. M., SABELFELD, K. K., GOTSCHKE, T., GRANDAL, J., CALLEJA, E., GEELHAAR, L., AND BRANDT, O. "Self-Regulated Radius of Spontaneously Formed GaN Nanowires in Molecular Beam Epitaxy". *Nano Lett.* *13* (2013), 3274.
- [11] HESTROFFER, K., LECLERE, C., BOUGEROL, C., RENEVIER, H., AND DAUDIN, B. "Polarity of GaN nanowires grown by plasma-assisted molecular beam epitaxy on Si(111)". *Phys. Rev. B* (2011).
- [12] KISHINO, K., SEKIGUCHI, H., AND KIKUCHI, A. "Improved Ti-mask selective-area growth (SAG) by rf-plasma-assisted molecular beam epitaxy demonstrating extremely uniform GaN nanocolumn arrays". *J. Cryst. Growth* *311* (2009), 2063.
- [13] KRUSE, J. E., EFTYCHIS, S., TSAGARAKI, K., ANDROULIDAKI, M., DIMITRAKIS, P., OLZIERSKY, A., NORMAND, P., AND GEORGAKILAS, A. "Selective growth of III-nitride nanopillars on Si (111) substrates". In *Book of Ext. Abstracts (23-27 June 2014)*, 22nd International Symposium on Nanostructures: Physics and Technology, Saint Petersburg, Russia. pp. 305306.
- [14] KRUSE, J. E., LYMPERAKIS, L., EFTYCHIS, S., ADIKIMENAKIS, A., DOUNDOULAKIS, G., TSAGARAKI, K., ANDROULIDAKI, M., OLZIERSKY, A., DIMITRAKIS, P., IOANNOU-SOUGLERIDIS, V., NORMAND, P., KOUKOULA, T., KEHAGIAS, T., KOMNINOU, P., KONSTANTINIDIS, G., AND GEORGAKILAS, A. "Selective-area growth of GaN

- nanowires on SiO₂-masked Si (111) substrates by molecular beam epitaxy". *Journal of Applied Physics* 119, 22 (2016), 224305.
- [15] MONEMAR, B. "Fundamental energy gap of GaN from photoluminescence excitation spectra". *Phys. Rev. B* 10 (1974), 676.
- [16] MUSOLINO, TAHRAOUI, A., FERNANDEZ-GARRIDO, S., BRANDT, O., TRAMPERT, A., GEELHAAR, L., AND RIECHERT, H. "Compatibility of the selective area growth of GaN nanowires on AlN-buffered Si substrates with the operation of light emitting diodes". *Nanotechnology* 26 (2015), 085605.
- [17] SAM-GIAO, D., MATA, R., TOURBOT, G., RENARD, J., WYSMOLEK, A., DAUDIN, B., AND GAYRAL, B. "Fine optical spectroscopy of the 3.45eV emission line in GaN nanowires". *J. Appl. Phys.* 113 (2013), 043102.
- [18] SCHUMANN, T., GOTSCHKE, T., LIMBACH, F., STOICA, T., AND CALARCO, R. "Selective-area catalyst-free MBE growth of GaN nanowires using a patterned oxide layer". *Nanotechnology* 22 (2011), 095603.
- [19] SEKIGUCHI, H., KISHINO, K., AND KIKUCHI, A. "Ti-mask Selective-Area Growth of GaN by RF-Plasma-Assisted Molecular-Beam Epitaxy for Fabricating Regularly Arranged InGaN/GaN Nanocolumns". *Appl. Phys. Express* 1 (2008), 124002.
- [20] SHEN, X. Q., KISHIMOTO, D., AND NISHINAGA, T. "Arsenic Pressure Dependence of Surface Diffusion of Ga on Nonplanar GaAs Substrates". *Jpn. J. Appl. Phys., Part 1* 33 (1994), 11.

Summary and future prospects

10.1 Conclusions

The work presented in this dissertation deals with GaN nanowire growth on Si (111) substrates by plasma assisted molecular beam epitaxy. The ongoing research focuses on two methods of GaN NW growth, either the spontaneous self-organized growth, or the selective area growth. This work aimed in expanding the current understanding of GaN NWs formation on Si (111) substrates and the role of the initial surface on which NWs are formed, both in the case of spontaneous self-organized growth and of selective area growth.

The effect of substrate temperature on the growth of GaN NWs by a one-step or a two-step growth procedure was identified (chapter 5). In the one-step case, we found that the Arrhenius-like increase of the incubation time observed is described by an incubation energy of $E_{inc} = 7.5 \pm 0.5$ eV, for GaN nucleation on a crystalline layer of AlN. At the highest substrate temperatures studied, the NW formation is suppressed due to the increased Ga desorption rate. On the contrary, when a low temperature initial growth phase precedes a higher temperature growth phase, a high density of NWs can be achieved due to enhanced GaN nucleation of the low substrate temperature. The two-step growth procedure also ensures that the majority of the NW nucleation events occur during the initial growth stage, thus isolating the NW elongation stage in the second stage. The different substrate temperatures studied in the second stage, revealed a maximum height of the NWs grown at 770°C. This was correlated with a decrease in the Ga adatom diffusion length on the side facets of the GaN NWs, for substrate temperatures larger than 770°C, due to increased desorption. A decreased NW radial growth was also found with increasing the substrate temperature. For the maximum temperature studied (800°C) the NW height for the two-step growth method was increased by 237 % (from 95 nm to 320 nm) and the NW density by two orders of magnitude (from 9.7×10^7 cm⁻³ to 1.5×10^{10} cm⁻³) compared to the one-step growth method.

A comparison of the GaN NW formation on intentionally and unintentionally nitridated Si (111) surfaces, allowed for a clear identification of the cause of differences in the alignment and dimensions of the NWs. It should be pointed out that in our experimental PAMBE setup, GaN nucleation and unintentional Si (111) nitridation started simultaneously, as opposed to the commonly reported unintentional nitridation process of the Si (111) surface, before commencing the GaN deposition, that cannot be avoided in other PAMBE growth chambers. This was verified by the clear observation of the 7×7 RHEED pattern until the GaN growth initiation. The results in this case revealed GaN/Si interface regions where GaN nucleated directly on crystalline Si (111) and other regions with GaN nucleation on amorphous Si_xN_y . When GaN NWs nucleate on the intentionally nitridated Si (111) surface, a flat 1.5 nm of amorphous Si_xN_y layer was identified by HRTEM. Due to its uniformity, the grown NWs had a more homogeneous height, a better axial alignment and a larger diameter compared to NWs grown on the unintentionally nitridated Si (111) substrate.

Concerning the effects of an AlN prelayer on Si (111) substrates, we investigated for the first time the effects of ultrathin AlN layers on the GaN NW nucleation and growth process. Our study provided quantitative insights about the effects of increasing amount of deposited AlN, with nominal thickness between 0 and 1.5 nm. Significant differences in the nucleation, density and morphological characteristics of GaN NWs were observed, even for AlN nominal thickness in the range of 0.2 - 0.5 nm that is not sufficient for full coverage of the Si (111) substrate by a crystalline AlN layer. The deposition of 0.2 - 0.5 nm AlN accelerates the nucleation of 3D GaN islands on Si (111) by providing crystalline AlN nuclei as heterogeneous nucleation sites in the overall amorphized Si surface (Si_xN_y formation). This results in an increased height of GaN NWs, significant improvement of their crystallographic alignment and height homogeneity, and a decrease in the NW diameter and density. A full coverage of the Si substrate by crystalline AlN is achieved for 1.5 nm AlN deposition, which suppresses the formation of an amorphous Si_xN_y interfacial layer and improves the homogeneity of GaN NW nucleation. The formation of crystalline $\beta\text{-Si}_3\text{N}_4$ for a short period prior the AlN formation was also identified.

When growing GaN NWs on off-axis Si (111) substrates, we found that the $(0001)_{\text{GaN}}// (111)_{\text{Si}}$ epitaxial relation is dominant. The results reveal that the miscut angle of the Si (111) substrates affects the GaN NWs nucleation and elongation processes and thus their morphological characteristics. We found a weaker $(0001)_{\text{GaN}}// (111)_{\text{Si}}$ epitaxial relation for the thicker amorphous Si_xN_y interfacial layers. The epitaxial relation of GaN NWs with the Si (111) crystal even in the case of the intentionally deposited 10 nm Si_xN_y

interfacial layer, suggest that local regions of the Si_xN_y layer should have preserved their crystalline structure. Finally, the significant tilt angle observed between GaN [0001] and Si [111] for the case of GaN NWs grown on an AlN crystalline prelayer, cannot be explained by Nagai's model. The tilting of the AlN (0001) layer relative to the Si (111) crystal is attributed to the structure of the misfit dislocation network at the AlN/Si interface, which is induced by the presence of substrate steps.

In the case of selective area growth (SAG) of GaN NWs, this work aimed in investigating the limits of growth on a SiO_2 mask that is prepared directly on Si (111) substrates, without the use of any III-nitride prelayer growth. We showed that a proper amount of AlN can be deposited on the patterned substrates to increase the selectivity of the GaN growth process i.e., enhance nucleation events that occur in the selected Si nucleation sites (mask window openings), but not on the SiO_2 mask surface. The investigation of the mask's geometrical characteristics showed that in order to have GaN NWs grown in the majority of the windows, the distance between them (for the growth conditions used) should be larger than 500 nm, and the windows should not be wider than 50 nm. Numerical calculations that were performed, in combination with the observed NW array characteristics, revealed that Ga adatoms' diffusion towards mask windows that have GaN NWs grown inside, suppresses further GaN nucleation events in neighbouring windows, which are in a distance comparable to the Ga adatom diffusion length.

10.2 Relevant Future work

Over the last two decades since the initial realization of spontaneously grown GaN NWs [1, 2], works that focused on GaN NW growth on crystalline AlN and amorphous Si_xN_y have advanced our understanding of the nucleation mechanism and the diffusion induced elongation process. As our understanding of the GaN NW formation continues to expand, more details are revealed, that highlight the complexity of the processes occurring during the nucleation and the elongation stages of the GaN NWs. In the following, we mention some of the remaining open questions that could be the subject of further studies.

One of the assumptions that we make, when studying the structure of samples grown by MBE, is that the crystalline structure (from bottom to top) occurs during the deposition of the layers. While this may be true for the majority of the structures studied, when AlN was grown on Si (111) by MOCVD, an amorphous interface was identified forming at the AlN (0001) / Si (111) interface at high temperatures due to Si outdiffusion[3]. Similarly

with this, the final amorphous Si_xN_y that is widely observed between the GaN (0001) / Si (111) interface, may also result from a solid-state interaction by interdiffusion of Si and N atoms at the interface. Observation of such a solid-state reaction would be valuable for identifying high-temperature device degradation. If such a process takes place, mechanisms for limiting Si outdiffusion could be studied in order to improve GaN device performance and increase their active lifetime.

An issue that still puzzles scientists working on GaN NW growth, is the origin of the epitaxial relation of GaN NWs with the Si (111) crystal, in the case that GaN NWs nucleate and grow on an amorphous Si_xN_y layer. Although there are studies that suggest polycrystallinity of the amorphous Si_xN_y [4], there is still no direct evidence to support such claims. A study where GaN NWs would grow on different thicknesses of amorphous Si_xN_y on Si (111) substrates, and also on miscut Si (111) surfaces with increasing tilt angle, could identify the limits where the epitaxial relationship is lost. Such a study should include HRTEM analysis of the Si_xN_y layer with a low electron beam energy so that any possible alteration of crystallinity of the Si_xN_y layer due to interaction with the electron beam would be avoided [5]. The presence of crystalline $\beta\text{-Si}_3\text{N}_4$ islands during the initial NW nucleation stages, that become amorphous through a solid-state reaction during the later NW growth stages should also be confirmed or disregarded.

Throughout this work, another factor besides fluxes and substrate temperature that could be used in order to fine-tune the GaN NW nucleation has been identified, namely the use of ultrathin AlN prelayers of different thicknesses. Variations of the AlN nominal thickness as low as ~ 0.1 nm, exhibited significant differences in the GaN NW nucleation behaviour, as described in Chapter 7. Furthermore in Chapter 9 the deposition of ~ 0.4 nm of AlN on patterned SiO_2 / Si (111) substrates lead to enhancement of the GaN nucleation inside the mask's windows but not on the SiO_2 mask surface, leading to improved selectivity of the patterned growth. The next step to this study would be the investigation of ultrathin AlN prelayer thicknesses in the region between 0.5-1.5 nm. Additionally this study would include the effect of different AlN prelayer thicknesses on SiO_2 masked samples. Such a study, would give a complete picture of the role of the AlN thickness on spontaneously grown GaN NWs, as well as on the selectively grown GaN NWs. It could also allow to comprehensively optimize the GaN/Si interfacial structure for minimizing the conduction barrier (resistance) at the interface between Si substrate and GaN NWs, in vertical conduction GaN NW devices.

Bibliography

- [1] M. Yoshizawa, A. Kikuchi, N. Fujita, K. Kushi, H. Sasamoto, and K. Kishino. "Self-organization of GaN/Al_{0.18}Ga_{0.82}N multi-layer nanocolumns on (0001) Al₂O₃ by RF molecular beam epitaxy for fabricating GaN quantum disks". *J. Cryst. Growth*, 189/190:138, 1998.
- [2] M.A. Sanchez-Garcia, E. Calleja, E. Monroy, F.J. Sanchez, F. Calle and E. Munoz, and R. Beresford. "The effect of the III/V ratio and substrate temperature on the morphology and properties of GaN- and AlN-layers grown by molecular beam epitaxy on Si(111)". *J. Cryst. Growth*, 183:23, 1998.
- [3] P.-Y. Lin, J.-Y. Chen, Y. C. Chen, and L. Chang. "Effect of Growth Temperature on Formation of Amorphous Nitride Interlayer between AlN and Si(111)". *J. J. Appl.Phys.*, 52:08JB20–1, 2013.
- [4] A. Wierzbicka, Z. R. Zytkeiwicz, S. Kret, J. Borysiuk, P. Dluzewski, M. Sobanska, K. Klosek, A. Reszka, G. Tchutchulashvili, A. Cabaj, and E.Lusakowska. "Influence of substrate nitridation temperature on epitaxial alignment of GaN nanowires to Si(111) substrate". *Nanotechnology*, 24(3):035703, 2013.
- [5] X. S. Wang, G. Zhai, J. Yang, L. Wang, Y. Hu, Z. Li, J. C. Tang, X. Wang, K. K. Fung, and N. Cue. "Nitridation of Si (111)". *Surf. Science*, 494:83, 2001.

Si (111) wafer preparation

In the main work presented, GaN NWs are grown on 3" Si (111) wafers. Prior any deposition on the wafers, a specific chemical and thermal preparation was followed.

A.1 Chemical treatment

The Si (111) surface is oxidized very easily in the atmosphere, and a SiO_x layer is expected to cover the substrate surface as well as various contaminants. Initially, the Si (111) wafers were immersed in a solution of $\text{H}_2\text{SO}_4:\text{H}_2\text{O}_2$ (piranha), with a ratio 4:1, for 10 min. This step aims in cleaning any organic residue, that could be present on the substrates. This chemical solution also oxidizes slightly the Si surface [1]. After careful rinsing in de-ionized (DI) water, the substrate was then submerged in an $\text{HF}:\text{H}_2\text{O}$, 1:10 solution, for 90s. The HF solution used, etches the SiO_x layer, revealing the clean Si (111) surface. After rinsing again in DI water, a third solution is used, in order to form a volatile SiO_x on the Si (111) surface. The solution consists of $\text{HCl}:\text{H}_2\text{O}_2:\text{H}_2\text{O}$ (1:1:6), and the wafer is submerged for 10 min. After a final DI rinsing, the wafers were dried under N_2 , and then immediately loaded in the load chamber of the MBE system. According to older studies [2], this final treatment results in a volatile SiO_x , that protects the Si surface from contamination and inside the MBE growth chamber can be desorbed in a controllable way through appropriate heating treatment, ensuring the cleanliness of the Si (111) surface.

A.2 Thermal treatment

When the substrate is loaded in the MBE chamber, an initial heat treatment up to 650°C is performed in the degas chamber. This treatment aims in removing any adsorbed gases on the Si surface. It is specially effective in

removing any H_2O from the substrate, and it is necessary in order to keep the growth chamber as clean as possible.

After the desorption of adsorbed gases, a final heating treatment is performed in the main growth chamber to desorb the SiO_x layer, producing an atomically clean Si (111) surface. During this step, the substrate is heated up to 800°C , for 20 min and a characteristic 7×7 RHEED pattern appears at $740\text{-}760^\circ\text{C}$. This reconstruction has characteristic RHEED patterns, with 6 streaks visible between the 0^{th} and 1^{st} reflection of the Si (111), for incident electron beam directions towards $\langle 0\bar{1}1 \rangle$ and $\langle \bar{2}11 \rangle$ (Fig. A.1). It denotes the characteristic Si (111) 7×7 surface reconstruction revealing the cleanliness of the Si surface [3].

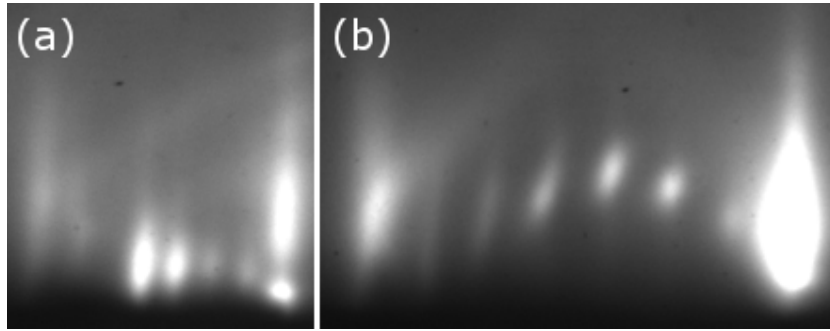


Figure A.1: The characteristic 7×7 pattern for electron beam incidence along the (a) $\langle 0\bar{1}1 \rangle$ and (b) $\langle \bar{2}11 \rangle$ Si azimuth, denoting the characteristic 7×7 Si (111) surface reconstruction.

The above described procedure, up to the characteristic 7×7 RHEED reconstruction observation, was followed in all cases when a Si (111) substrate was used, unless otherwise stated.

Bibliography

- [1] AJAGUNNA, A. O. "*Heteroepitaxy of InN on Silicon (111) and R-plane sapphire substrates*". PhD thesis, University of Crete, Physics Department, 2011.
- [2] KAYAMBAKI, M., CALLEC, R., CONSTANTINIDIS, G., PAPAVALASSIOU, C., LOCHTERMANN, E., KRASNY, H., PAPADAKIS, N., PANAYOTATOS, P., AND GEORGAKILAS, A. "Investigation of Si-substrate preparation for GaAs-on-Si MBE growth". *J. Cryst. Growth* 157 (1995), 300.
- [3] TAKAYANAGI, K., TANISHIRO, Y., TAKAHASHI, M., AND TAKAHASHI, S. "Structural analysis of Si(111)7x7 by UHVtransmission electron diffraction and microscopy". *J. Vac. Sci. Technol. A* 3, 3 (1985), 1502.

Publications - Conferences

B.1 Journal publications

1. **S. Eftychis**, J. Kruse, T. Koukoula, Th. Kehagias, Ph. Komninou, A. Adikimenakis, K. Tsagaraki, M. Androulidaki, P. Tzanetakis, E. Iliopoulos and A. Georgakilas, Understanding the effects of Si (111) nitridation on the spontaneous growth and properties of GaN nanowires, Journal of Crystal Growth 442 (2016) 813.

2. J. E. Kruse, L. Lymperakis, **S. Eftychis**, A. Adikimenakis, G. Doundoulakis, K. Tsagaraki, M. Androulidaki, A. Olziersky, P. Dimitrakis, V. Ioannou-Sougleridis, P. Normand, T. Koukoula, Th. Kehagias, Ph. Komninou, G. Konstantinidis and A. Georgakilas, Selective-area growth of GaN nanowires on SiO₂-masked Si (111) substrates by molecular beam epitaxy, Journal of Applied Physics 119, 224305 (2016)

3. **S. Eftychis**, J. Kruse, K. Tsagaraki, T. Koukoula, Th. Kehagias, Ph. Komninou and A. Georgakilas, Effects of ultrathin AlN prelayers on the spontaneous growth of GaN nanowires by plasma assisted molecular beam epitaxy, submitted in Journal of Crystal growth

B.2 Conference proceedings publications

1. Understanding the role of interfacial layers on the spontaneous growth of GaN nanowires by plasma assisted molecular beam epitaxy, (oral), **S. Eftychis**, J. E. Kruse, K. Tsagkaraki, M. Androulidaki, T. Koukoula, Th. Kehagias, Ph. Komninou, A. Georgakilas, Workshop on compound semiconductor devices and integrated circuits (WOCSDICE) 2014, Delfi, Greece, pp. 165-166

2. Importance of substrate temperature in one-step or two-step process of spontaneous GaN nanowire growth by plasma assisted molecular beam

epitaxy, (oral), **S. Eftychis**, J. E. Kruse, G. Doundoulakis, K. Tsagkaraki, M. Androulidaki, A. Georgakilas, Workshop on compound semiconductor devices and integrated circuits (WOCSDICE) 2014, Delfi, Greece, pp. 173-174

3. Selective growth of III-nitride nanopillars on Si (111) substrates, J. E. Kruse, **S. Eftychis**, K. Tsagaraki, M. Androulidaki, P. Dimitrakis, A. Olziersky, P. Normand and A. Georgakilas, 22nd Int. Symp. Nanostructures: Physics and Technology, Saint Petersburg, Russia, June 2327, 2014, pp. 305-306

4. Surface dependent structure of GaN nanowires spontaneously grown on Si (poster) T. Koukoura, T. Kehagias, J. Kioseoglou, **S. Eftychis**, J. Kruse, A. Georgakilas, P. Komninou, 18th International Microscopy Congress (IMC2014), Prague, Czech Republic, 7-12 September 2014, pp. 2354-2355

5. Structural properties of GaN/AlN/GaN core-double shell nanowires (poster) T. Koukoura, T. Kehagias, J. Kioseoglou, **S. Eftychis**, J. Kruse, A. Georgakilas, T. Karakostas, P. Komninou, 18th International Microscopy Congress (IMC2014), Prague, Czech Republic, 7-12 September 2014, pp. 2352-2353

6. Spontaneous growth of GaN nanowires on bare and AlN treated Si (111) (oral) T. Koukoura, Th. Kehagias, J. Kioseoglou, **S. Eftychis**, J. Kruse, A. Georgakilas, Ph. Komninou, Expert evaluation & control of compound semiconductor materials & technologies (EXMATEC) 2014, Delfi, Greece, pp. 265-266

7. A study on the fabrication of devices and the characterization of GaN nanowires and the GaN/Si heterojunction, (oral), G. Doundoulakis, A. Mparamis, E. Tsikritsaki, A. Stavrinidis, Ch. Zervos, G. Kwnstantinidis, M. Kagiampaki, **S. Eftychis**, J. E. Kruse, A. Adikimenakis, A. Georgakilas, Workshop on compound semiconductor devices and integrated circuits (WOCSDICE) 2014, Delfi, Greece, pp. 129-130

8. Nanopatterning of Si(111) substrates for selective growth of III-nitride nanowires by plasma-assisted molecular beam epitaxy, (oral), P. Dimitrakis, A. Olziersky, V. Ioannou Sougleridis, P. Normand, J. E. Kruse, **S. Eftychis**, G. Doundoulakis, K. Tsagkaraki, M. Androulidaki, G. Konstantinidis, A. Georgakilas, Workshop on compound semiconductor devices and integrated circuits (WOCSDICE) 2014, Delfi, Greece, pp. 131-132

9. Growth mechanism of catalyst-free GaN nanowires: An atomistic view, (oral), L. Limperakis, **S. Eftychis**, J. E. Kruse, A. Georgakilas, Expert

evaluation & control of compound semiconductor materials & technologies (EXMATEC) 2014, Delfi, Greece, pp.261-262

B.3 International Conferences

1. Study of the nucleation of GaN nanopillars on Si (111) substrates by plasma-assisted molecular beam epitaxy, (oral), **S. Eftychis**, J. E. Kruse, K. Tsagkaraki, M. Androulidaki, A. Adikimenakis, T. Koukoula, Th. Kehagias, Ph. Komninou, A. Georgakilas, International Conference on Intergranular and Interphase Boundaries in Materials, 2013, Sithonia, Halkidiki, Greece

2. The role of substrate temperature in the spontaneous nucleation and growth of GaN nanopillars on Si(111) substrates, (poster), J. E. Kruse, **S. Eftychis**, K. Tsagkaraki, M. Androulidaki, A. Adikimenakis, A. Georgakilas, International Conference on Intergranular and Interphase Boundaries in Materials, 2013, Sithonia, Halkidiki, Greece

3. Spontaneous growth of III-V semiconductor nanopillars by molecular beam epitaxy for nanoelectronic, photonic and sensor applications, (oral), A. Georgakilas, A. Adikimenakis, **S. Eftychis**, J. E. Kruse, K. Tsagkaraki, M. Androulidaki, E. Iliopoulos, Z. Hatzopoulos, P. Tzanetakis, Ph. Komninou, T. Koukoula, Th. Kehagias, G. P. Dimitrakopoulos, J. Kioseoglou, A. Lotsari, Th. Karakosas, G. Konstantinidis, G. Doundoulakis, K. Zekentes, P. Dimitrakis, V. Ioannou Sougleridis, A. Olziersky, P. Normand, 4th International Conference from Nanoparticles and Nanomaterials to Nanodevices and Nanosystems (IC4N), 2013, Corfu, Greece

4. Role of AlN Nucleation Layers in the Spontaneous Growth of GaN [0001] Nanopillars on Si(111) Substrates, (oral), J. E. Kruse, **S. Eftychis**, K. Tsagkaraki, M. Androulidaki, A. Adikimenakis, T. Koukoula, Th. Kehagias, Ph. Komninou, A. Georgakilas, 4th International Conference from Nanoparticles and Nanomaterials to Nanodevices and Nanosystems (IC4N), 2013, Corfu, Greece

5. The effect of substrate temperature on the nucleation and on the growth of GaN nanopillars on Si(111) substrates, (poster), **S. Eftychis**, J. E. Kruse, K. Tsagkaraki, M. Androulidaki, A. Adikimenakis, G. Doundoulakis, A. Georgakilas, International Workshop on Nitride Semiconductors 2014, Wroclav, Poland

6. Selective growth of GaN nanopillars on patterned Si(111) substrates, (poster), J.E. Kruse, **S. Eftychis**, G. Doundoulakis, K. Tsagkaraki, M. An-

droulidaki, A. Olziersky, P. Normad, A. Georgakilas, International Workshop on Nitride Semiconductors 2014, Wroclav, Poland

7. Effects of AlN and SiXNY interlayers on the nucleation and growth of GaN nanopillars on Si(111) substrates by PAMBE, (poster), **S. Eftychis**, J. E. Kruse, K. Tsagkaraki, M. Androulidaki, T. Koukoula, Th. Kehagias, Ph. Komninou, A. Georgakilas, International Workshop on Nitride Semiconductors 2014, Wroclav, Poland

8. Superior quality GaN NWs grown on AlN treated Si (111) substrates (poster) T. Kehagias, T. Koukoula, J. Kioseoglou, **S. Eftychis**, J. Kruse, A. Georgakilas, P. Komninou, International Workshop on Nitride Semiconductors 2014, Wroclav, Poland

9. GaN/AlN Core/ Shell Nanowires: Structural and Electronic Properties (poster) T. Pavloudis, J. Kioseoglou, T. Koukoula, T. Kehagias, **S. Eftychis**, J. Kruse, A. Georgakilas, P. R. Briddon, M. J. Rayson, T. Karakostas, and P. Komninou, International Workshop on Nitride Semiconductors 2014, Wroclav, Poland

10. Effects of AlN interfacial layers on spontaneous growth of GaN nanowires by plasma assisted molecular beam epitaxy, (poster), **S. Eftychis**, J. E. Kruse, K. Tsagkaraki, M. Androulidaki, T. Koukoula, Th. Kehagias, Ph. Komninou, A. Georgakilas, 8th Nanowire Growth Workshop Nanowires 2014, August 25-29, 2014 Eindhoven, Germany

11. Structural Analysis and Modelling of GaN/AlN Core/Shell Nanowires (poster) T. Koukoula, Th. Kehagias, J. Kioseoglou, **S. Eftychis**, J. Kruse, A. Georgakilas, Th. Karakostas, Ph. Komninou, International Conference on Extended Defects in Semiconductors (EDS2014), Gttingen, Germany, 14-19 September 2014

12. Surface Pre-treatment of (111) Si Substrates for GaN Nanowires Growth (poster) T. Koukoula, Th. Kehagias, J. Kioseoglou, **S. Eftychis**, J. Kruse, A. Georgakilas, Th. Karakostas, Ph. Komninou, International Conference on Extended Defects in Semiconductors (EDS2014), Gttingen, Germany, 14-19 September 2014

13. Temperature effects on GaN nanowire growth by PAMBE, (poster), **S. Eftychis**, J. E. Kruse, K. Tsagkaraki, M. Androulidaki, A. Adikimenakis, G. Doundoulakis, A. Georgakilas, 18th International Conference on Molecular Beam Epitaxy, September 7-12, 2014, Flagstaff, Arizona

14. Role of AlN Interfacial Layers on the spontaneous Growth of GaN Nanowires on Si(111) substrates, (poster), **S. Eftychis**, J. E. Kruse, K. Tsagkaraki, M. Androulidaki, T. Koukoula, Th. Kehagias, Ph. Komninou,

A. Georgakilas, 18th International Conference on Molecular Beam Epitaxy, September 7-12, 2014, Flagstaff, Arizona

15. Selective Growth of GaN Nanowires on SiO₂-masked Si(111) Substrates (poster), J. E. Kruse, **S. Eftychis**, G. Doundoulakis, K. Tsagkaraki, M. Androulidaki, P. Dimitrakis, A. Olziersky, P. Normad, A. Georgakilas, 18th International Conference on Molecular Beam Epitaxy, September 7-12, 2014, Flagstaff, Arizona

16. Comparison of Intentional and Unintentional Si (111) Nitridation Effects on the Interface and Properties of Spontaneously Grown GaN Nanowires, (poster), **S. Eftychis**, J. E. Kruse, K. Tsagkaraki, M. Androulidaki, T. Koukoula, Th. Kehagias, Ph. Komninou, E. Iliopoulos, Z. Hatzopoulos, A. Georgakilas, 11th International Conference on Nitride Semiconductors (ICNS-11), August 30th-September 4th, 2015, Beijing, China

17. Effectivity of SiO₂-Mask Patterns for Selective-Area Growth of GaN Nanowires on Si(111) Substrates, (poster), J. E. Kruse, **S. Eftychis**, L. Lymperakis, A. Adikimenakis, G. Doundoulakis, K. Tsagkaraki, M. Androulidaki, E. Iliopoulos, P. Tzanetakis, A. Olziersky, P. Dimitrakis, V. Ioannou-Sougleridis, P. Normad, T. Koukoula, Th. Kehagias, Ph. Komninou, A. Georgakilas, 11th International Conference on Nitride Semiconductors (ICNS-11), August 30th-September 4th, 2015, Beijing, China

18. Electrical characterization of individual gallium nitride nanopillars synthesized by plasma assisted molecular beam epitaxy, G. Doundoulakis, A. Stavriniadis, **S. Eftychis**, J. Kruse, M. Androulidaki, K. Tsagaraki, M. Kayambaki, G. Konstantinidis, P. Normand, K. Zekentes and A. Georgakilas, 11th International Conference on Nitride Semiconductors (ICNS-11), August 30th-September 4th, 2015, Beijing, China

19. Interfacial Structure of Self-Assembled GaN NWs Grown on Si (111) and R-Plane Sapphire Substrates (poster), Ph. Komninou, T. Koukoula, T. Kehagias, A. Lotsari, G.P. Dimitrakopoulos, J. Kioseoglou, Th. Karakostas, **S. Eftychis**, A. Adikimenakis, J. Kruse, A. Georgakilas, 11th International Conference on Nitride Semiconductors (ICNS-11), August 30th-September 4th, 2015, Beijing, China

20. SiO₂-mask patterns for selective-area growth of GaN nanowires on Si(111) substrates, (oral), J. Kruse, **S. Eftychis**, A. Adikimenakis, G. Doundoulakis, K. Tsagaraki, M. Androulidaki, A. Olziersky, P. Dimitrakis, V. I.-Sougleridis, P. Normand, T. Koukoula, T. Kehagias, Ph. Komninou and A. Georgakilas, European Materials Research Society 2015 fall meeting (EMRS 2015), September 15 -18 Warsaw, Poland

21. Understanding the effects of AlN and SiN layers on the Nucleation and Growth of GaN Nanowires by Plasma Assisted Molecular Beam Epitaxy, (oral), **S. Eftychis**, J. Kruse, A. Adikimenakis, K. Tsagaraki, M. Androulidaki, T. Koukoula, Th. Kehagias, Ph. Komninou and A. Georgakilas, Euromat 2017, 17-22 September, Thessaloniki, Greece

22. Evaluation and understanding of size effects on the conductivity of spontaneously grown GaN nanowires, (oral) G. Doundoulakis, A. Stavrinidis, **S. Eftychis**, M. Androulidaki, K. Tsagaraki, M. Kayambaki, G. Konstantinidis, A. Georgakilas, Euromat 2017, 17-22 September, Thessaloniki, Greece

B.4 Panhellenic conferences

1. Nucleation and growth of GaN nanowires by plasma-assisted molecular beam epitaxy”, (oral), **S. Eftychis**, J. E. Kruse, K. Tsagkaraki, M. Androulidaki, T. Koukoula, Th. Kehagias, Ph. Komninou, A. Georgakilas, 30th Panhellenic Conference on Solid-State Physics and Materials Science, Heraklion, Greece, 21-24 September 2014

2. The role of Intentional and Unintentional Nitridation of Si (111) in the Growth of GaN Nanowire by Plasma Assisted Molecular Beam Epitaxy, (poster), **S. Eftychis**, J. E. Kruse, K. Tsagkaraki, M. Androulidaki, T. Koukoula, Th. Kehagias, Ph. Komninou, E. Iliopoulos, Z. Hatzopoulos, A. Georgakilas, 31st Panhellenic Conference on Solid-State Physics and Materials Science, Thessaloniki, 20-23 September 2015

3. Nanoscale properties of GaN nanowires grown on Si substrates with an AlN interfacial layer, (poster), T. Koukoula, Th. Kehagias, J. Kioseoglou, **S. Eftychis**, J. Kruse, A. Georgakilas, Ph. Komninou, 30th Panhellenic Conference on Solid-State Physics and Materials Science, Heraklion, Greece, 21-24 September 2014

4. Interfacial phenomena in GaN core-AlN/GaN shell nanowires (poster) T. Koukoula, Th. Kehagias, Th. Pavloudis, J. Kioseoglou, **S. Eftychis**, J. Kruse, A. Georgakilas, Ph. Komninou, 30th Panhellenic Conference on Solid-State Physics and Materials Science, Heraklion, Greece, 21-24 September 2014

5. Catalyst-free growth of GaN NWs on Si (111) and r-planesapphire (poster), T. Koukoula, T. Kehagias, A. Lotsari, G.P. Dimitrakopoulos, J. Kioseoglou, Th. Karakostas, **S. Eftychis**, A. Adikimenakis, J. Kruse, A.

Georgakilas, Ph. Komninou, XXXI Panhellenic Conference on Solid-State Physics and Materials Science Thessaloniki, Greece, 20-23 September 2015

